

The nature of photoexcitations and carrier multiplication in low-dimensional semiconductors

Kulkarni, Aditya

DOI

[10.4233/uuid:32a7a099-94c3-45f7-955b-b14628996011](https://doi.org/10.4233/uuid:32a7a099-94c3-45f7-955b-b14628996011)

Publication date

2019

Document Version

Final published version

Citation (APA)

Kulkarni, A. (2019). *The nature of photoexcitations and carrier multiplication in low-dimensional semiconductors*. [Dissertation (TU Delft), Delft University of Technology].
<https://doi.org/10.4233/uuid:32a7a099-94c3-45f7-955b-b14628996011>

Important note

To cite this publication, please use the final published version (if applicable).
Please check the document version above.

Copyright

Other than for strictly personal use, it is not permitted to download, forward or distribute the text or part of it, without the consent of the author(s) and/or copyright holder(s), unless the work is under an open content license such as Creative Commons.

Takedown policy

Please contact us and provide details if you believe this document breaches copyrights.
We will remove access to the work immediately and investigate your claim.

The nature of photoexcitations and carrier
multiplication in low-dimensional
semiconductors

The nature of photoexcitations and carrier multiplication in low-dimensional semiconductors

Proefschrift

ter verkrijging van de graad van doctor
aan de Technische Universiteit Delft,
op gezag van de Rector Magnificus prof. dr. ir. T. H. J. J. van der Hagen,
voorzitter van het College voor Promoties,
in het openbaar te verdedigen op
maandag 24 juni 2019 om 10:00 uur

door
Aditya KULKARNI

Master of Science in Physics
Sri Sathya Sai Institute of Higher Learning, India
geboren te Davanagere, India

Dit proefschrift is goedgekeurd door de promotor

Prof. dr. L. D. A. Siebbeles

Samenstelling promotiecommissie:

Rector Magnificus

Prof. dr. L. D. A. Siebbeles

Voorzitter

Technische Universiteit Delft, promotor

Onafhankelijke leden:

Prof. dr. J. Gomez Rivas

Prof. dr. ir. H. T. C. Stoof

Dr. A. J. Houtepen

Prof. dr. B. Dam

Prof. dr. D. A. M. Vanmaekelbergh

Prof. dr. S. J. Picken

Technische Universiteit Eindhoven

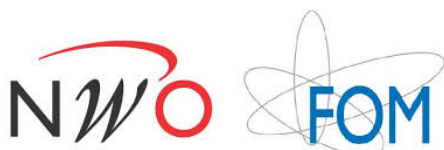
Universiteit Utrecht

Technische Universiteit Delft

Technische Universiteit Delft

Universiteit Utrecht

Technische Universiteit Delft



Dit werk maakt deel uit van het onderzoeksprogramma van de Stichting voor Fundamenteel Onderzoek der Materie (FOM), die deel uitmaakt van de Nederlandse Organisatie voor Wetenschappelijk Onderzoek (NWO), in het project “Designing Dirac carriers in semiconductor honeycomb superlattices”.

Printed by Ipskamp printing, The Netherlands

Copyright © 2019 Aditya Kulkarni

Cover designed by the author

ISBN: 978-94-028-1559-7

An electronic version of this dissertation is available at:

<http://repository.tudelft.nl>

Table of Contents

Chapter 1

Introduction	7
1.1 Nanoscience and nano semiconductors	7
1.2 Synthesis of nanocrystals	8
1.3 Size dependent electronic properties of nanocrystals	9
1.4 Excitons	11
1.4 Anisotropic nanocrystals	12
1.5 Carrier multiplication in nanostructures	14
1.6 The nature of electron-hole pairs as a function of density	16
1.7 Terahertz photoconductivity experiments to probe charge carriers and excitons	17
1.8 Thesis outline	18

Chapter 2

Efficient Steplike Carrier Multiplication in Percolative Networks of Epitaxially Connected PbSe Nanocrystals	25
2.1 Introduction	26
2.1 Materials and methods	27
2.1 Results and discussion	29
2.3 Conclusions	36

Appendix A	41
-------------------	-----------

Chapter 3

Photogeneration Quantum Yield and Character of Free Charges and Excitons in PbSe Nanorods	43
3.1 Introduction.	44
3.2 Materials and methods	45
3.3 Results and discussion	47
3.4 Conclusions	56

Appendix B	61
-------------------	-----------

Chapter 4

Room-Temperature Electron Transport in PbSe Honeycomb Superstructures Studied in a Transistor Configuration and by Terahertz Spectroscopy **65**

4.1 Introduction	66
4.2 Materials and methods	67
4.3 Results and discussion.	69
4.4 Conclusions	78

Appendix C **85**

Chapter 5

Charge Carrier Cooling Bottleneck Opens up Nonexcitonic Gain Mechanisms in Colloidal CdSe Quantum wells **95**

5.1 Introduction	96
5.2 Materials and methods	98
5.3 Results and discussion	100
5.3 Conclusions	114

Appendix D **121**

Summary **137**

Samenvatting **139**

Acknowledgements **141**

List of publications **143**

Curriculum Vitae **145**

Chapter 1

Introduction

1.1 Nanoscience and nano semiconductors

The famous physicist Richard Feynman proposed manipulating and controlling properties on a small scale in his talk in 1959 “There's Plenty of Room at the Bottom: An Invitation to Enter a New Field of Physics.” Since then especially after 1980, the field of nanoscience and nanotechnology has emerged as a major scientific field and continues to grow till today with synthesis of various new nanomaterials with their applications in the field of nanoparticle based targeted drug delivery, nanomedicine, optoelectronics and the list goes on. Then, how small is a nanometer? A nanometer (nm) is a one billionth $\left(\frac{1}{10^9}\right)^{th}$ of a meter. To practically understand how small a nm is, a human hair is about 10^5 nm thick and red blood cells are about 10^4 nm.¹

At nano-scale, the properties of a material are governed by quantum physics and are different from their bulk macroscopic counterparts. Among nanomaterials magnetic nanoparticles are extensively used for magnetic resonance imaging, drug delivery and multimodal imaging.^{2,3} Semiconducting nanomaterials also known as nanocrystals (NCs) have gained a lot attraction due to their size and shape tunable electronic and optical properties.³ One such example is shown in Figure 1.1C where the emission from CdSe quantum dots (QDs, isotropic NCs) is observed to be size dependent and the whole visible spectrum is covered by changing the size of QDs.

Semiconductors are a class of solid-state materials with their conductivity in between that of metals and insulators.⁴ Examples of metals are gold, silver, aluminum and iron, and examples of insulators are wood and plastic. A good example for a semiconductor is silicon that is used in solar cells that we see every day. Modern electronics relies on semiconductors from which smartphones, computers, televisions, communication systems are built and our life without them would be unimaginable.

Another way to classify semiconductors is based on their band gap.⁴ The overlap of electronic wavefunctions of the constituent atoms in a semiconductor crystal form closely spaced energy levels known as an energy band. In an intrinsic semiconductor, those energy levels that are filled with electrons form valence bands and unfilled ones

form conduction bands.⁴ The difference between the lowest conduction and the highest valence band is formidable and is referred to as the band gap.⁴ The typical band gap in semiconductors is 0.7-3.5 eV, and metals do not have a band gap, and insulators have a band gap greater than 4 eV. By absorbing a photon also referred to as photoexcitation an electron in a valence band can be promoted to a conduction band leaving behind an empty state called a hole.⁴ The promoted electron is free to move until it recombines with the hole to emit a photon, or eventually gets trapped due to imperfections in the crystal.

NCs exhibit properties that are significantly different from their bulk counterparts as illustrated by the size dependent emission from CdSe QDs.⁵⁻⁷ A few other factors that influence the optoelectronic properties of NCs including the size are: the environment around NCs, and the type of ligands that are protecting the NCs surface.^{8, 9} In addition, quantum confinement in NCs enhances the Coulomb attraction between electrons and holes to form a neutral bound electron-hole (e-h) pair known as an exciton.¹⁰ Therefore, the physics of nanomaterials is of interest from a fundamental perspective and also for various applications. Below research questions are listed, that are important to be addressed in this field:

- How semiconducting NCs are synthesized?
- What is the relation between the electronic and optical properties of NCs with their size and dimensionality?
- Does the nano-geometry (square or honeycomb) influence or affect their electronic structure compared to their analog NCs?
- What is the conduction mechanism in these NCs?
- To what extent does photoexcitation of NCs leads to electrons or holes that are free to move or do they form Coulombically bound electron-hole pairs known as excitons?

1.2 Synthesis of nanocrystals

So far NCs have been synthesized by various techniques such as molecular beam epitaxy, chemical vapor deposition, sol-gel, micro emulsions, hot injection etc. Among them hot injection, a “bottom-up approach”, has been used extensively to synthesize NCs.¹¹ Suitable precursors are introduced into a reaction flask with a hot solvent to form monomers. Nucleation occurs after a certain monomer threshold has reached and the growth of crystals continues until the reaction has been stopped, which is usually done by reducing the temperature.^{11, 12} Figure 1.1 shows the typical

reaction flask and the transmission electron microscope (TEM) image of a CdSe/CdS QDs. The surface of a NC is protected by surfactant ligands to prevent agglomeration and to keep them electrically neutral. The NCs studied in this thesis were synthesized by hot injection and are semiconducting by their nature.

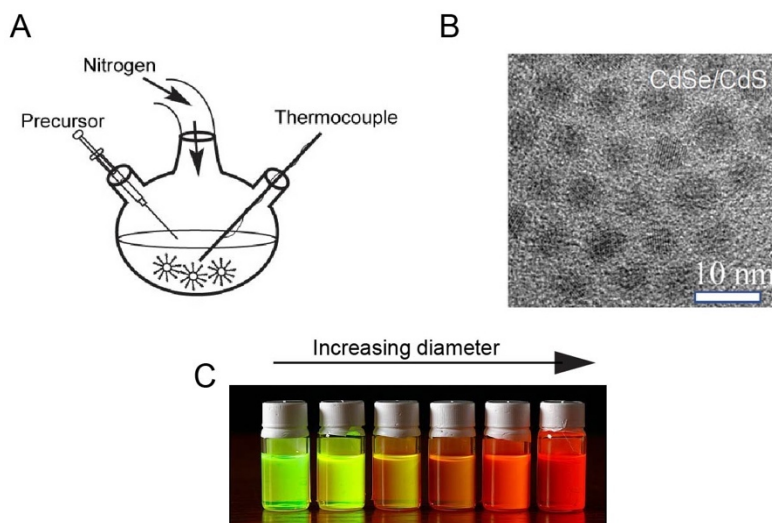


Figure 1.1. Bottom up approach. (A) Typical synthesis procedure used in hot injection method for synthesizing nanomaterials. (B) TEM image of CdSe/CdS, core/shell QDs (adapted from ref ¹³). (C) Red shift in the emission of CdSe QDs as their diameter increases (picture credit: prof. dr. A. Houtepen).

1.3 Size dependent electronic properties of nanocrystals

As mentioned above, the electronic and optical properties of NCs differ significantly from their bulk analogues (see Figure 1.1C). It is evident from the emission of CdSe QDs as the diameter decreases the emission is shifted towards shorter wavelength and reaches close to 500 nm for a diameter of 1.3 nm. To understand the observed trend, it is important to obtain the relation between the band gap and the size of NCs. At first, we begin with the electronic structure of a bulk semiconductor. In a bulk semiconductor a delocalized free electron experiences a periodic potential $V(x)$ caused by its constituent atoms.⁴ Assuming a chain of atoms along the x -direction, the total energy for this delocalized electron along the one dimensional chain is given by the time independent Schrodinger equation⁴

$$\frac{-\hbar^2}{2m_e} \frac{\partial^2 \psi(x)}{\partial x^2} + V(x)\psi(x) = E\psi(x), \quad (1.1)$$

with $\hbar = \frac{h}{2\pi}$, h is the Planck's constant, m_e the electron effective mass, different from the rest mass of an electron in vacuum, and is required to correct for the motion of the electron in the periodic potential, E the energy eigen value for the electron, $\psi(x)$ the eigen function. F. Bloch has proven that for a periodic potential in crystal with a lattice constant a , $\psi_{Bloch}(x) = e^{ikx}u(x)$, with $k = \frac{2\pi}{\lambda}$ the wavevector and a periodic modulating function $u_k(x) = u_k(x+a)$.^{4, 14} Therefore at $x+a$, the wavefunction $\psi_{Bloch}(x+a) = e^{ika}\psi_{Bloch}(x)$, is changed by a phase factor.

When the wavelength of the electron $\lambda = \frac{a}{2}$, k becomes $k = \frac{\pi}{a}$, the electron is reflected due to the periodic potential. These reflections also known as Bragg reflections occurring at $k = \pm \frac{\pi}{a}$, create standing waves with a significant energy difference between them at the same k value opening up band gaps.⁴

According to the top-down approach, for a NC, the Bloch wavefunctions of their analog bulk semiconductor are retained but with a correction for the spatial confinement of e-h pairs.¹⁴ The corrected wavefunction $\psi_{cor}(x)$, is given by the product of the Bloch wavefunction $\psi_{Bloch}(x)$ and an envelope function $\phi_{env}(x)$,¹⁴

$$\psi_{cor}(x) = \psi_{Bloch}(x)\phi_{env}(x). \quad (1.2)$$

The spatial confinement of e-h pairs in a NC is analogous to a particle in a box.¹⁴ $\phi_{env}(x)$ can be obtained by solving the time independent Schrodinger equation for a particle in a box.¹⁴ For a cubic box of length L , the energy levels of an electron is given by¹⁵

$$E_{n_x, n_y, n_z}^{conf} = \frac{\hbar^2 \pi^2}{2m_e L^2} (n_x^2 + n_y^2 + n_z^2), \quad (1.3)$$

where n_x, n_y, n_z are non-zero integers.

For a spherical QD, the envelope function is a product of a spherical harmonics and a radial Bessel function, *i.e.*

$$\varphi_{env}(\theta, \phi, r) = \gamma_l^m(\theta, \phi) R(r). \quad (1.4)$$

By taking an infinite potential outside the QD with diameter D , and solving the Schrodinger equation for the eigen function in expression (1.4) yields¹⁴

$$E_{n,l}^{conf}(D) = \frac{2\hbar^2 \chi_{nl}^2}{m_e D^2}. \quad (1.5)$$

The values of χ_{nl} depend on the quantum numbers n and l .¹⁴ For $n=1$, l can take values 0, 1, 2,..... which corresponds to energy levels 1S, 1P, 1D.... and continues further for $n=2, 3, \dots$ which corresponds to 2X, 3X... (X=S, P, D...). Due to such discrete energy levels similar to that of atoms, QDs are referred as artificial atoms. The band gap of a QD is the sum of electrons and holes confinement energies in addition to the bulk band gap, yielding¹⁴

$$E_{g,QD} = E_{g,bulk} + \frac{2\hbar^2 \chi_{nl}^2}{m_e D^2} + \frac{2\hbar^2 \chi_{nl}^2}{m_h D^2}, \quad (1.6)$$

with m_e (m_h) the effective mass for electrons (holes). According to expression (1.6), as the diameter of a QD decreases the band gap $E_{g,QD}$ increases, which is clearly seen from the emission from CdSe QDs shown in Figure 1.1C. Note that this expression is valid only for the strong confinement regime.

1.4 Excitons

Photoexcitation promotes an electron to the conduction band and leaves behind a hole in the valence band. The oppositely charged electron and hole can attract each other to form a neutral bound e-h pair known as an exciton. The binding energy of an exciton E_b in the ground state can be obtained according to,¹⁰

$$E_b = -\frac{\mu R_H}{m_o \epsilon_r^2}, \quad (1.7)$$

where $\mu = \frac{m_e m_h}{m_e + m_h}$ the reduced mass of the exciton, with m_e (m_h) the effective mass of the electron (hole), $R_H = 13.6$ eV the Rydberg constant, ϵ_r the dielectric constant of the material, m_o the rest mass of an electron in vacuum. Qualitatively it can be understood that the exciton binding energy decreases as the dielectric constant increases. For example, the dielectric constant for bulk PbSe is 210 which has $E_b < 1$ meV. NCs are typically dispersed in a solvent and are protected by ligands. The dielectric constant of the most commonly used solvents such as hexane, toluene, tetrachloroethylene is close to 2. Hence the exciton binding energy for NCs dispersed in these solvents must be higher than their bulk counterparts. A direct comparison can be made between bulk PbSe and PbSe nanorods dispersed in a solvent. According to calculations for a PbSe nanowire of radius 1 nm surrounded by a medium of dielectric constant 2, the exciton binding energy is close to 0.4 eV,¹⁶ whereas in bulk PbSe it is less than 1 meV.

The exciton Bohr radius determines the spatial extent of an exciton according to¹⁰

$$a_B = \frac{m_o e_r}{\mu} a_o , \quad (1.8)$$

where a_o is the Bohr radius of a hydrogen atom. In bulk PbSe the spatial extent of an exciton, *i.e.* the exciton Bohr radius, is 46 nm. This implies that an exciton is spread over 1.7×10^6 atoms, since in bulk PbSe the lattice constant is 6.12 Angstrom. Such spatially extended excitons over many atoms in the lattice are called Wannier-Mott excitons.

1.4 Anisotropic nanocrystals

The motion of an electron in a QD (0-D) is restricted equally in all three directions.¹⁷ In quasi-one dimensional (1-D) NCs such as nanorod and nanowires, the motion of an electron is restricted in two directions and the electron is free to move in the other direction.¹⁷ In quasi-two dimensional (2-D) NCs like nanoplatelets and nanosheets, the motion of an electron is restricted in only one direction and is free to move in the other two directions.¹⁷ The difference between them can be understood based on the density of states $\rho(E)$ available to be occupied by electrons in an

energy interval. Figure 1.2 shows the density of states for bulk (3-D), 2-D, 1-D and 0-D semiconductors.¹⁷

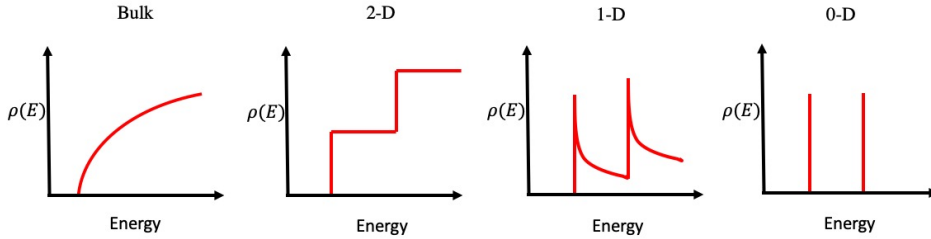


Figure 1.2. Density of states *versus* energy for bulk, two-dimensional, one-dimensional and zero-dimensional systems.

In addition to these anisotropic structures, square and honeycomb superlattices were prepared by facet specific oriented attachment of PbSe QDs recently (see Figure 1.3).¹⁸⁻²⁰ Theoretical calculations have shown the electronic structure of an ideal PbSe square superlattice to be distinct from the electronic structure of a PbSe two-dimensional continuous sheet (quantum well). The electronic band width calculated close to 100 meV for these structures is promising to achieve efficient charge transport.²¹⁻²³ Honeycomb structures of PbSe and CdSe were prepared to combine the electronic properties of graphene with semiconducting properties. Theoretical calculations on honeycomb structures have shown the presence of Dirac cones at the K point of the Brillouin zone and hence massless Dirac carriers are expected near the K point.^{21, 22}

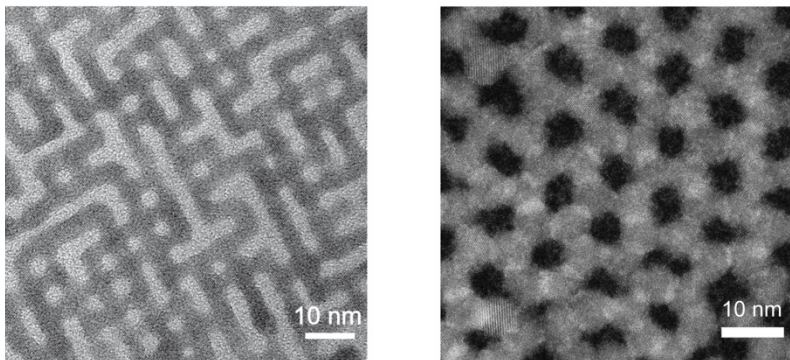


Figure 1.3. TEM picture of a typical percolative superlattice (left) (adapted from ref.²⁴) and TEM image of a typical honeycomb superlattice (right).

Conductivity experiments performed by Evers *et al.*, on a PbSe percolative network (non-ideal square superlattices with less than 4 connections per QD) has shown a charge mobility as high as $260 \text{ cm}^2\text{V}^{-1}\text{s}^{-1}$ in a non-contact optical pump-THz photoconductivity measurement and in a DC measurement a value of $13 \text{ cm}^2\text{V}^{-1}\text{s}^{-1}$ has been achieved.²⁵ This DC mobility value has been reproduced in a recently published study on a percolative network prepared by a slightly different method.²⁶ The measured ac charge mobility value of $260 \text{ cm}^2\text{V}^{-1}\text{s}^{-1}$ for a percolative network is much higher than the values found for films of PbSe QDs connected by short organic linkers, which is typically $1\text{-}40 \text{ cm}^2\text{V}^{-1}\text{s}^{-1}$.^{27, 28} The achieved high mobility offers prospects in applications such as infra-red photodetectors and ultra-thin solar cells.

1.5 Carrier multiplication in nanostructures

In 2002, Nozik proposed possibilities to achieve higher efficiencies in a single junction QD solar cell by extracting hot carriers or by creating multiple e-h pairs *via* a process called carrier multiplication (CM).²⁹ CM also known as impact ionization in bulk semiconductors is a process of generating multiple e-h pairs by absorbing a single energetic photon. CM leads to an increase in the density of e-h pairs, thereby enhances the photocurrent leading to an increase in the power conversion efficiency of a solar cell.³⁰⁻³²

In a bulk semiconductor absorption of a photon with energy greater than the band gap creates a hot electron in the conduction band and a hot hole in the valence band. The hot e-h pair cools down to the band edge by emitting multiple phonons to reduce their excess energy which is an energy loss as shown in Figure 1.4A. Thermalization losses and photons that are not absorbed in a single junction silicon solar cell limit the efficiency to 31%, which is known as the Shockley-Queisser limit (shown in Figure 1.4D).³³ To avoid this energy loss Nozik proposed QDs based solar cells.²⁹ In QDs energy levels are discrete with the energy difference between the successive levels is greater than the LO phonon energy.²⁹ This makes thermalization in QDs less efficient than in bulk which reduces the energy loss rate which increases the probability to create an additional e-h pair.³⁴

In bulk semiconductors, apart from thermalization losses the momentum conservation plays a major role. Due to the size of QDs which is typically 1-10 nm, restrictions imposed due to the momentum conservation are relaxed.³⁴ Therefore for CM to occur in QDs, it is enough if the energy conservation requirements are met. In addition, the Coulomb coupling between the single exciton states to multiexciton

states is higher in QDs than in bulk which enhances the CM rate.³⁵ According to a theoretical estimation if CM happens efficiently such that the quantum yield follows the step-like behavior as shown in Figure 1.4C, the power conversion efficiency can reach up to 42% which is a significant enhancement compared to the Shockley-Quiesser limit.^{32, 36}

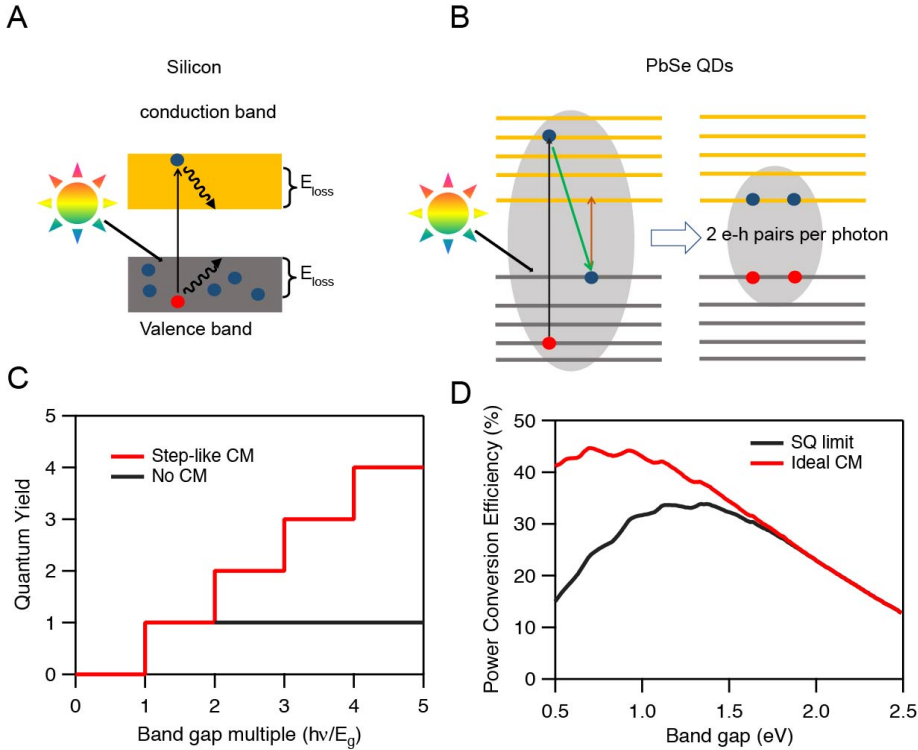


Figure 1.4. CM and its benefit. (A) Cooling of hot e (blue dots) -h (red dots) pairs in silicon to the band edge leading to an energy loss. (B) CM in PbSe QDs creates two e-h pairs per a single absorbed photon. (C) Quantum yield versus band gap multiple for the case when there is an ideal CM and no CM. (D) Theoretical estimation of the highest achievable power conversion efficiency due to CM and the Shockley-Quiesser limit.

CM experiments were performed extensively on Pb-chalcogenide QDs due to the possibility to tune their band gap close to 1eV by changing their size. CM signatures in PbSe QD dispersions were observed experimentally in various studies with an onset for CM at $3E_g$.^{35, 37, 38} Schaller *et al.*, rationalized the observation by proposing a symmetrical excess energy sharing between the electron and hole based on the fact that the effective masses for electrons and holes are almost the same in bulk PbSe.³⁹

However, to realize solar cells based on QDs, electrons and holes must be sufficiently mobile to reach electrodes. To achieve this, films of PbSe QDs connected by short organic linkers have been prepared to prevent Auger recombination of e-h pairs and to obtain charge transport over a long distance. Charge mobilities in the range of $1\text{-}40\text{ cm}^2\text{V}^{-1}\text{s}^{-1}$ have been obtained in various films of PbSe QDs.^{27, 28} CM experiments performed on PbSe QD films have shown efficiencies similar to that of QD dispersions.⁴⁰⁻⁴¹ To have better performing solar cells the mobility of charges plays a crucial role. In this context, PbSe percolative networks are more suitable due to charge mobility close to $260\text{ cm}^2\text{V}^{-1}\text{s}^{-1}$. Having a material with a high charge mobility with efficient CM would be ideal for a solar cell. Therefore, the CM efficiency in PbSe percolative networks are investigated in this thesis and the results are discussed in chapter 2.

1.6 The nature of electron-hole pairs as a function of density

As discussed earlier, enhanced Coulomb interaction between an electron and a hole due to quantum confinement and the solvent environment with a low dielectric constant close to 2, increases the binding energy of excitons in NCs to an extent that they are stable at room temperature. In anisotropic semiconductors, especially in transition metal dichalcogenides, CdSe nanoplatelets, and PbSe nanorods the exciton binding energy reaches a few hundreds of meV.^{16, 42, 43} Robust excitons at room temperature are useful to achieve optical gain and lasing. Photoexcitation of these transition metal dichalcogenides, CdSe nanoplatelets and PbSe nanorods most likely produces excitons and a few might dissociate into free charges by absorbing energy from phonons.

According to the Saha model, electrons and holes are in thermal equilibrium with excitons.^{44, 45} The Saha equilibrium constant depends on the exciton binding energy E_x and the reduced mass of electrons and holes μ and the temperature T . Based on the Saha model, exciton formation increases with the photoexcitation density and as a consequence the quantum yield of charges decreases.⁴⁵ At extremely high densities beyond this regime, as the average inter-exciton distance becomes less than the exciton Bohr diameter, a strong screening of the attraction between electrons and holes can lead to break down of excitons and result in a transition to a conducting e-h plasma as depicted in Figure 1.5. In this thesis, in-depth study on excitation density dependent nature of photoexcitations in PbSe nanorods has been performed and the results are discussed in chapter 3.

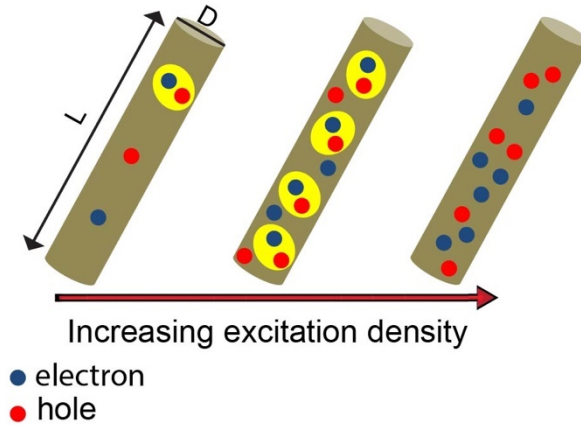


Figure 1.5. The nature of electrons and holes illustrated as a function of excitation density for a nanorod of length L and diameter D .

1.7 Terahertz photoconductivity experiments to probe charge carriers and excitons

Optical pump-terahertz (THz) probe (OPTP) spectroscopy is a widely used technique to measure the dynamics and mobility of charge carriers in a non-contact way. Especially in OPTP technique, charge carriers are probed on a nanometer scale and are less prone to domain boundaries and defects in the sample.⁴⁶ Hence the mobility of charge carriers determined by this way is accurate, and not affected by imperfections of the sample unlike in DC measurements.⁴⁶

A THz electric field oscillates at a frequency of 10^{12} Hz which corresponds to 4 meV in energy. In the setup that we used THz pulses were generated in a ZnTe or a Lithium Niobate crystal via optical rectification of 800 nm pulses of duration 60 fs delivered by a femtosecond mode-locked laser (Mira-Libra, Coherent Inc.).^{24, 25} The generated THz pulse was detected in a ZnTe crystal in a single laser shot by spatially overlapping with a chirped pulse.^{24, 25} An optical parametric amplifier from Coherent was used to generate pump pulses in the visible and infrared region. The differential THz signal $\Delta E(\tau, t)$ was obtained by the difference of the transmitted THz in the presence of optical pump $E_{excited}(\tau, t)$ and absence of optical pump $E_0(t)$ by placing a chopper in the pump beam.^{24, 25} τ is the time delay between the pump and probe varied by an automated delay stage and t is the time delay between the THz generation pulse and detection pulse. The real part of the THz conductivity is due to

the in-phase drift velocity of charge carriers in the probing THz field which reduces the amplitude of the transmitted THz field.⁴⁶ The imaginary part of the THz conductivity is due to the out-of phase drift velocity of charges and the polarizability of excitons which leads to a phase retardation in the transmitted THz field.^{46, 47} The fourier transform of $\Delta E(\tau, t)$ with respect to t yields $\Delta E(\tau, \omega)$, and similarly $E_0(t)$ yields $E_0(\omega)$. The complex mobility of charges, weighted by their quantum yield $\phi_e \mu_e + \phi_h \mu_h$ and the polarizability of excitons α related to $\Delta E(\tau, \omega)$,²⁵

$$\phi_e \mu_e + \phi_h \mu_h + \phi_x \frac{\alpha \omega}{e} = A \frac{\Delta E(\tau, \omega)}{E_0(\omega)}, \quad (1.9)$$

where ϕ_e, ϕ_h, ϕ_x are the quantum yield of electrons, holes and excitons respectively, e the elementary charge, and A is a proportionality constant which depends on the thickness of the film and the dielectric constant of the sample.^{46, 48}

The transport mechanism of charge carriers can be understood by modelling the frequency dependent complex mobility. Among them the simplest model, the Drude model has been able to explain the measured complex conductivity of charges in bulk GaAs, silicon, and in PbS.⁴⁶ In the Drude model, the mobility of charge carriers is affected by scattering by phonons, and charges do not interact with each other and do not experience any barrier or imperfections in the crystal.⁴⁶ In nanomaterials and films of QDs, a behavior opposite to the Drude model has been observed with negative values for the imaginary part of the conductivity and an increasing real part of the conductivity with frequency.^{49, 50} To explain the measured behavior Smith *et al.*, modified the Drude model and introduced a back-scattering parameter c to account for elastic collisions of charges.⁵¹ This model is able to explain the measured complex THz conductivity in various nanomaterials and in films of QDs.^{47, 52}

We have used the Drude-Smith model to explain the measured complex THz mobility of charges in a PbSe honeycomb superstructure with results being explained in chapter 4.

1.8 Thesis outline

This thesis describes ultrafast spectroscopy studies on low-dimensional semiconductors. The aim is to determine the nature of photoexcitations and the efficiency of CM. Measuring the terahertz (THz) conductivity and transient optical

absorption (TA) as a function of time after the pump pulse allows one to study the nature and mechanism of photogeneration, and decay of charges carriers and excitons.

Until now, CM in thin films and solar cells of semiconductor NCs has been found to begin at photon energies well above the minimum required energy of twice the band gap. The high threshold of CM strongly limits the benefits for solar cell applications. We performed THz photoconductivity experiments on a PbSe percolative network to determine the threshold and efficiency of CM. As discussed in chapter 2, the threshold for CM in PbSe percolative network is at the minimum energy of twice the band gap.

In chapter 3, we determine to what extent photoexcitation of PbSe nanorods leads to free charges or excitons, and we determine the charge carrier mobility and the exciton polarizability. We combine time-resolved TA spectroscopy with THz photoconductivity measurements for different photoexcitation densities to distinguish free charges from excitons.

PbSe honeycomb superlattices have been prepared to combine the electronic properties of graphene with semiconducting features. In chapter 4, we report the band occupation and electron transport in PbSe honeycomb superstructures at room temperature studied by DC transistor type measurements and THz photoconductivity measurements.

Ultrathin 2-D materials have received much attention in the past years for a wide variety of photonic applications due to their pronounced room temperature excitonic features, leading to unique properties in terms of light-matter interaction. In chapter 5, we study on light amplification and the complex photo-physics at high excitation density in CdSe nanoplatelets by using TA spectroscopy, time-resolved photoluminescence, and terahertz photoconductivity measurements.

References

1. Aarts, P. A.; Bolhuis, P. A.; Sakariassen, K. S.; Heethaar, R. M.; Sixma, J. J., Red blood cell size is important for adherence of blood platelets to artery subendothelium. *Blood* **1983**, *62* (1), 214.
2. Li, W.; Liu, Y.; Qian, Z.; Yang, Y., Evaluation of Tumor Treatment of Magnetic Nanoparticles Driven by Extremely Low Frequency Magnetic Field. *Sci. Rep.* **2017**, *7*, 46287.
3. Pankhurst, Q. A.; Connolly, J.; Jones, S. K.; Dobson, J., Applications of magnetic nanoparticles in biomedicine. *J. Phys. D: Appl. Phys.* **2003**, *36* (13), R167-R181.
4. Kittel, C., *Introduction to Solid State Physics*. Wiley: 2004.
5. Norris, D. J.; Bawendi, M. G., Measurement and assignment of the size-dependent optical spectrum in CdSe quantum dots. *Physical Review B* **1996**, *53* (24), 16338-16346.
6. Norris, D. J.; Sacra, A.; Murray, C. B.; Bawendi, M. G., Measurement of the size dependent hole spectrum in CdSe quantum dots. *Physical Review Letters* **1994**, *72* (16), 2612-2615.
7. Smith, A. M.; Nie, S., Semiconductor nanocrystals: structure, properties, and band gap engineering. *Acc. Chem. Res.* **2010**, *43* (2), 190-200.
8. Rodina, A. V.; Efros, A. L. J. J. o. E.; Physics, T., Effect of dielectric confinement on optical properties of colloidal nanostructures. **2016**, *122* (3), 554-566.
9. Lifshitz, E., Evidence in Support of Exciton to Ligand Vibrational Coupling in Colloidal Quantum Dots. *The Journal of Physical Chemistry Letters* **2015**, *6* (21), 4336-4347.
10. Fox, M., *Optical Properties of Solids*. Oxford University Press: Oxford, 2001.
11. Murray, C. B.; Norris, D. J.; Bawendi, M. G., Synthesis and characterization of nearly monodisperse CdE (E = sulfur, selenium, tellurium) semiconductor nanocrystallites. *Journal of the American Chemical Society* **1993**, *115* (19), 8706-8715.
12. Chang, J.; Waclawik, E. R., Colloidal semiconductor nanocrystals: controlled synthesis and surface chemistry in organic media. *RSC Advances* **2014**, *4* (45), 23505-23527.
13. Wang, X.; Yu, J.; Chen, R., Optical Characteristics of ZnS Passivated CdSe/CdS Quantum Dots for High Photostability and Lasing. *Sci. Rep.* **2018**, *8* (1), 17323.
14. Koole, R.; Groeneveld, E.; Vanmaekelbergh, D.; Meijerink, A.; de Mello Donegá, C., Size Effects on Semiconductor Nanoparticles. In *Nanoparticles: Workhorses of Nanoscience*, de Mello Donegá, C., Ed. Springer Berlin Heidelberg: Berlin, Heidelberg, 2014; pp 13-51.
15. Griffiths, D. J.; Schroeter, D. F., *Introduction to quantum mechanics*. Third edition. ed.; Cambridge University Press: Cambridge, United Kingdom, 2018.

16. Bartnik, A. C.; Efros, A. L.; Koh, W. K.; Murray, C. B.; Wise, F. W., Electronic states and optical properties of PbSe nanorods and nanowires. *Physical Review B* **2010**, 82 (19), 195313.
17. Krahne, R.; Morello, G.; Figuerola, A.; George, C.; Deka, S.; Manna, L., Physical properties of elongated inorganic nanoparticles. *Physics Reports* **2011**, 501 (3), 75-221.
18. Evers, W. H.; Goris, B.; Bals, S.; Casavola, M.; de Graaf, J.; van Roij, R.; Dijkstra, M.; Vanmaekelbergh, D., Low-Dimensional Semiconductor Superlattices Formed by Geometric Control over Nanocrystal Attachment. *Nano Letters* **2013**, 13 (6), 2317-2323.
19. Boneschanscher, M. P.; Evers, W. H.; Geuchies, J. J.; Altantzis, T.; Goris, B.; Rabouw, F. T.; van Rossum, S. A. P.; van der Zant, H. S. J.; Siebbeles, L. D. A.; Van Tendeloo, G.; Swart, I.; Hilhorst, J.; Petukhov, A. V.; Bals, S.; Vanmaekelbergh, D., Long-range orientation and atomic attachment of nanocrystals in 2D honeycomb superlattices. *Science* **2014**, 344 (6190), 1377.
20. Whitham, K.; Yang, J.; Savitzky, B. H.; Kourkoutis, L. F.; Wise, F.; Hanrath, T., Charge transport and localization in atomically coherent quantum dot solids. *Nature Materials* **2016**, 15, 557.
21. Kalesaki, E.; Evers, W. H.; Allan, G.; Vanmaekelbergh, D.; Delerue, C., Electronic structure of atomically coherent square semiconductor superlattices with dimensionality below two. *Physical Review B* **2013**, 88 (11), 115431.
22. Kalesaki, E.; Delerue, C.; Morais Smith, C.; Beugeling, W.; Allan, G.; Vanmaekelbergh, D., Dirac Cones, Topological Edge States, and Nontrivial Flat Bands in Two-Dimensional Semiconductors with a Honeycomb Nanogeometry. *Physical Review X* **2014**, 4 (1), 011010.
23. Delerue, C.; Vanmaekelbergh, D., Electronic band structure of zinc blende CdSe and rock salt PbSe semiconductors with silicene-type honeycomb geometry. *2D Materials* **2015**, 2 (3), 034008.
24. Kulkarni, A.; Evers, W. H.; Tomić, S.; Beard, M. C.; Vanmaekelbergh, D.; Siebbeles, L. D. A., Efficient Steplike Carrier Multiplication in Percolative Networks of Epitaxially Connected PbSe Nanocrystals. *ACS Nano* **2018**, 12 (1), 378-384.
25. Evers, W. H.; Schins, J. M.; Aerts, M.; Kulkarni, A.; Capiod, P.; Berthe, M.; Grandidier, B.; Delerue, C.; van der Zant, H. S. J.; van Overbeek, C.; Peters, J. L.; Vanmaekelbergh, D.; Siebbeles, L. D. A., High charge mobility in two-dimensional percolative networks of PbSe quantum dots connected by atomic bonds. *Nature Communications* **2015**, 6, 8195.
26. Balazs, D. M.; Matysiak, B. M.; Momand, J.; Shulga, A. G.; Ibáñez, M.; Kovalenko, M. V.; Kooi, B. J.; Loi, M. A., Electron Mobility of $24 \text{ cm}^2 \text{ V}^{-1} \text{ s}^{-1}$ in PbSe Colloidal-Quantum-Dot Superlattices. *Advanced Materials* **2018**, 30 (38), 1802265.
27. Guglietta, G. W.; Diroll, B. T.; Gaulding, E. A.; Fordham, J. L.; Li, S.; Murray, C. B.; Baxter, J. B., Lifetime, Mobility, and Diffusion of Photoexcited Carriers in Ligand-Exchanged Lead Selenide Nanocrystal Films Measured by Time-Resolved Terahertz Spectroscopy. *ACS Nano* **2015**, 9 (2), 1820-1828.
28. Talgorn, E.; Gao, Y.; Aerts, M.; Kunneman, L. T.; Schins, J. M.; Savenije, T. J.; van Huis, M. A.; van der Zant, H. S. J.; Houtepen, A. J.; Siebbeles, L. D. A.,

Unity quantum yield of photogenerated charges and band-like transport in quantum-dot solids. *Nature Nanotechnology* **2011**, *6*, 733.

29. Nozik, A. J., Quantum dot solar cells. *Physica E: Low-dimensional Systems and Nanostructures* **2002**, *14* (1), 115-120.

30. Semonin, A. J., Third Generation Photovoltaics Based on Multiple Exciton Generation in Quantum Confined Semiconductors. *Acc. Chem. Res.* **2013**, *46*, 1252-1260.

31. Greenham, M. L., Multiple-Exciton Generation in Lead Selenide Nanorod Solar Cells with External Quantum Efficiencies Exceeding 120%. *Nat. Commun.* **2015**, *6*, 8259.

32. Beard, A. J., Effect of Solar Concentration on the Thermodynamic Power Conversion Efficiency of Quantum-Dot Solar Cells Exhibiting Multiple Exciton Generation. *J. Phys. Chem. Lett.* **2012**, *3*, 2857-2862.

33. Shockley, W.; Queisser, H. J., Detailed Balance Limit of Efficiency of p-n Junction Solar Cells. *Journal of Applied Physics* **1961**, *32* (3), 510-519.

34. Kershaw, S. V.; Rogach, A. L., Carrier Multiplication Mechanisms and Competing Processes in Colloidal Semiconductor Nanostructures. *Materials (Basel, Switzerland)* **2017**, *10* (9), 1095.

35. Ellingson, R. J.; Beard, M. C.; Johnson, J. C.; Yu, P.; Micic, O. I.; Nozik, A. J.; Shabaev, A.; Efros, A. L., Highly Efficient Multiple Exciton Generation in Colloidal PbSe and PbS Quantum Dots. *Nano Letters* **2005**, *5* (5), 865-871.

36. Beard, M. C.; Midgett, A. G.; Hanna, M. C.; Luther, J. M.; Hughes, B. K.; Nozik, A. J., Comparing Multiple Exciton Generation in Quantum Dots To Impact Ionization in Bulk Semiconductors: Implications for Enhancement of Solar Energy Conversion. *Nano Letters* **2010**, *10* (8), 3019-3027.

37. Smith, C.; Binks, D., Multiple Exciton Generation in Colloidal Nanocrystals. *Nanomaterials* **2014**, *4* (1), 19.

38. Stewart, J. T.; Padilha, L. A.; Qazilbash, M. M.; Pietryga, J. M.; Midgett, A. G.; Luther, J. M.; Beard, M. C.; Nozik, A. J.; Klimov, V. I., Comparison of Carrier Multiplication Yields in PbS and PbSe Nanocrystals: The Role of Competing Energy-Loss Processes. *Nano Letters* **2012**, *12* (2), 622-628.

39. Schaller, R. D.; Pietryga, J. M.; Goupalov, S. V.; Petruska, M. A.; Ivanov, S. A.; Klimov, V. I., Breaking the Phonon Bottleneck in Semiconductor Nanocrystals via Multiphonon Emission Induced by Intrinsic Nonadiabatic Interactions. *Physical Review Letters* **2005**, *95* (19), 196401.

40. Sandeep, C. S. S.; Cate, S. t.; Schins, J. M.; Savenije, T. J.; Liu, Y.; Law, M.; Kinge, S.; Houtepen, A. J.; Siebbeles, L. D. A., High charge-carrier mobility enables exploitation of carrier multiplication in quantum-dot films. *Nature Communications* **2013**, *4*, 2360.

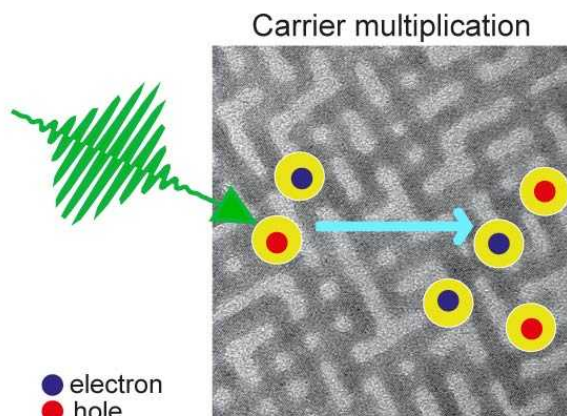
41. Aerts, M.; Suchand Sandeep, C. S.; Gao, Y.; Savenije, T. J.; Schins, J. M.; Houtepen, A. J.; Kinge, S.; Siebbeles, L. D. A., Free Charges Produced by Carrier Multiplication in Strongly Coupled PbSe Quantum Dot Films. *Nano Letters* **2011**, *11* (10), 4485-4489.

42. Park, S.; Mutz, N.; Schultz, T.; Blumstengel, S.; Han, A.; Aljarb, A.; Li, L.-J.; List-Kratochvil, E. J. W.; Amsalem, P.; Koch, N., Direct determination of monolayer MoS₂ and WSe₂ exciton binding energies on insulating and metallic substrates. *2D Materials* **2018**, *5* (2), 025003.

43. Scott, R.; Achtstein, A. W.; Prudnikau, A. V.; Antanovich, A.; Siebbeles, L. D. A.; Artemyev, M.; Woggon, U., Time-Resolved Stark Spectroscopy in CdSe Nanoplatelets: Exciton Binding Energy, Polarizability, and Field-Dependent Radiative Rates. *Nano Letters* **2016**, *16* (10), 6576-6583.
44. Kaindl, R. A.; Hägele, D.; Carnahan, M. A.; Chemla, D. S., Transient terahertz spectroscopy of excitons and unbound carriers in quasi-two-dimensional electron-hole gases. *Physical Review B* **2009**, *79* (4), 045320.
45. Ambigapathy, R.; Bar-Joseph, I.; Oberli, D. Y.; Haacke, S.; Brasil, M. J.; Reinhardt, F.; Kapon, E.; Deveaud, B., Coulomb Correlation and Band Gap Renormalization at High Carrier Densities in Quantum Wires. *Physical Review Letters* **1997**, *78* (18), 3579-3582.
46. Ulbricht, R.; Hendry, E.; Shan, J.; Heinz, T. F.; Bonn, M., Carrier dynamics in semiconductors studied with time-resolved terahertz spectroscopy. *Reviews of Modern Physics* **2011**, *83* (2), 543-586.
47. Joyce, H. J.; Boland, J. L.; Davies, C. L.; Baig, S. A.; Johnston, M. B., A review of the electrical properties of semiconductor nanowires: insights gained from terahertz conductivity spectroscopy. *Semiconductor Science and Technology* **2016**, *31* (10), 103003.
48. Lloyd-Hughes, J.; Jeon, T.-I., A Review of the Terahertz Conductivity of Bulk and Nano-Materials. *Journal of Infrared, Millimeter, and Terahertz Waves* **2012**, *33* (9), 871-925.
49. Cooke, D. G.; MacDonald, A. N.; Hryciw, A.; Wang, J.; Li, Q.; Meldrum, A.; Hegmann, F. A., Transient terahertz conductivity in photoexcited silicon nanocrystal films. *Physical Review B* **2006**, *73* (19), 193311.
50. Němec, H.; Kužel, P.; Sundström, V., Far-infrared response of free charge carriers localized in semiconductor nanoparticles. *Physical Review B* **2009**, *79* (11), 115309.
51. Smith, N. V., Classical generalization of the Drude formula for the optical conductivity. *Physical Review B* **2001**, *64* (15), 155106.
52. Beard, M. C.; Turner, G. M.; Murphy, J. E.; Micic, O. I.; Hanna, M. C.; Nozik, A. J.; Schmittenmaer, C. A., Electronic Coupling in InP Nanoparticle Arrays. *Nano Letters* **2003**, *3* (12), 1695-1699.

Chapter 2

Efficient Steplike Carrier Multiplication in Percolative Networks of Epitaxially Connected PbSe Nanocrystals



Based on:

Efficient Steplike Carrier Multiplication in Percolative Networks of Epitaxially Connected PbSe Nanocrystals.

Aditya Kulkarni, Wiel H. Evers, Stanko Tomić, Matthew C. Beard, Daniel Vanmaekelbergh and Laurens D. A. Siebbeles.

ACS Nano 2017, 12(1), 378-384

2.1 Introduction

Photoexcitation of an electron in a semiconductor produces an electron-hole (e-h) pair with excess energy equal to the difference of the photon energy and the band gap. The electron and hole can release their excess energy in the form of heat *via* phonon emission. A charge with excess energy greater than the band gap, can also relax by exciting another electron across the band gap. This process of carrier multiplication (CM) leads to generation of multiple e-h pairs per absorbed photon. CM is of great interest to enhance the photocurrent produced in a photovoltaic device.¹⁻⁶ In this context lead chalcogenide nanomaterials have received particular attention, since their band gap can be tuned to values near 1 eV, which is optimal for exploitation of CM in solar cells. The occurrence of CM has been observed in lead chalcogenide quantum dots in dispersion⁷⁻⁹ and thin film solids,^{6, 10-11} nanorods,^{2, 12-14} nanosheets,¹⁵ and bulk.¹⁶

For device applications the charges produced *via* CM must be sufficiently mobile to prevent Auger recombination and to enable their extraction at external electrodes. Charge mobilities in the range 1 - 40 cm²V⁻¹s⁻¹ have been found for thin film solids of PbSe nanocrystals (NCs) that are connected by short organic ligands.^{11, 17-18} Interestingly, a PbSe NC solid with 1,2-ethanediamine ligands has shown a lower threshold for CM than for the same NCs in dispersion.^{8, 11} In this PbSe NC solid the NCs are to some extent also coupled directly by thin atomic necks.¹⁹ Hence, electronic coupling appears not only to be beneficial to charge mobility, but also to reduce the threshold energy of CM. The coupling has been further enhanced by facet-specific oriented attachment of NCs.²⁰⁻²³ In the latter case, further thermal annealing of the formed superlattice results in the formation of a percolative PbSe network, in which the NCs are connected *via* strong crystalline bridges in the in-plane directions. There are on average less than 4 connections per nanocrystal in this system. The percolative network can hence be considered as a planar system with a dimensionality between 2 and 1 with straight segments in orthogonal directions, see Figure 2.1A. The short-range mobility of charge carriers was found to attain values as high 260 cm²V⁻¹s⁻¹ for a probing electric field oscillating in the terahertz (THz) frequency range.²³ Note, that the mobility in bulk PbSe is a few times higher than this value. The low band gap of a bulk PbSe crystal makes it, however, unsuitable for solar cell applications.^{3-4, 16}

The aim of the current work is to determine to what extent the enhanced electronic coupling in percolative PbSe networks affects the CM threshold energy and efficiency in addition to the beneficial effect on charge mobility already reported in ref. ²³. We studied the quantum yield for charge carrier photogeneration in

percolative PbSe networks and a PbSe NC solid, using optical-pump THz-probe (OPTP) time domain spectroscopy. We found that CM in percolative PbSe networks has lower threshold energy and is more efficient than in films of PbSe NCs coupled by organic ligands.¹¹ Interestingly, the CM efficiency follows a step-like dependence on photon energy and reaches a value of about 1.4 at the minimum required photon energy of twice the band gap. According to detailed-balance calculations the CM efficiency realised in the percolative PbSe network would enhance the power conversion efficiency of a solar cell by ~8% over the Shockley-Queisser limit for a band gap of 0.7eV at 1-sun. The results are of great promise for development of highly efficient third-generation solar cells.

2.1 Materials and methods

Sample preparation. PbSe NCs of diameter 5.8 ± 0.4 nm passivated with oleic acid surface ligands were synthesized according to the method of Steckel *et al.*²⁴ Two-dimensional percolative PbSe networks were prepared by oriented attachment of the PbSe NCs, as described previously.²³ According to TEM measurements the NCs are connected by necks of thickness 4.0 ± 0.4 nm with center-to-center distance of 6.4 ± 0.1 nm. The NC density in a network is 2.4×10^{12} cm⁻². To enhance the absorbed pump laser fluence and consequently the signal-to-noise ratio of the THz conductivity experiments, we stacked six monolayers of percolative PbSe networks on a quartz substrate, similar to our previous work.²³ The presence of long oleic acid ligands prevents electronic coupling between stacked layers. Consequently, charge transport only occurs within the layers and not from one layer to another. To get insight into the reproducibility of the experiments we studied two percolative networks that were both prepared according to the procedure outlined above.

A PbSe NC solid was prepared *via* layer-by-layer dip coating, using a DC multi-8 Nima Technology dip-coater.^{11, 18} At first, a quartz substrate was dipped into a dispersion of PbSe NCs with oleic acid ligands in hexane for 60 s. Subsequently, the sample was dipped into a 0.4 M solution of 1,2-ethanediamine ligands in methanol for 60 s for ligand exchange. Immediately after ligand exchange, the film was washed with methanol during 60 s. The above procedure was repeated 20 times to prepare a homogeneous film. The film has a thickness of 55 ± 10 nm, as determined with a Veeco Dektak 8 step-profilometer.

Terahertz photoconductivity measurements. Charge carriers were produced by excitation of the samples with optical pump pulses at varying wavelength and the

resulting photoconductivity was detected by time-domain THz spectroscopy,²⁵⁻²⁶ analogous to our previous work.²³ Pump pulses were generated starting from a chirped-pulse amplified laser system (Mira-Libra, Coherent Inc.), which runs at 1.4 kHz and delivers pulses of 60 fs at 800 nm. Pump pulses (<100 fs) in the infrared and visible were obtained from optical parametric amplification seeded by white light (Topas-Coherent). A BaB₂O₄ (BBO) crystal was used to generate pump pulses at 400 nm. Single-cycle THz waveforms were generated by optical rectification in LiNbO₃ and detected in a ZnTe crystal by the electro-optic effect. A pinhole of 1.5 mm diameter was placed on the samples to ensure photoexcitation and probing of the same sample area during different experiments.

The photogeneration quantum yield of charge carriers, ϕ , and decay kinetics of charge carriers were obtained from the difference, $\Delta E(t_p, t) = E_{excited}(t_p, t) - E_0(t_p)$, of the maximum amplitude of the THz electric field at time t after the optical pump pulse, $E_{excited}(t_p, t)$, and the maximum amplitude of the THz waveform at time t_p after generation of the THz waveform, $E_0(t_p)$, in the absence of the pump pulse. The THz conductivity signal is then obtained according to^{27, 28}

$$S(t) = \frac{-\Delta E(t_p, t)}{E_0(t_p)} = \phi \left(\frac{f_e(t)\mu_e + f_h(t)\mu_h}{2c\epsilon_0 n_{eff}} \right) N_a e. \quad (2.1)$$

In Equation 2.1 the functions $f_e(t)$ ($f_h(t)$) are the fractions of electrons (holes) that have survived from trapping or recombination, N_a is the absorbed pump photon fluence, c is the speed of light, ϵ_0 is the vacuum permittivity, n_{eff} is the effective refractive index in the THz frequency range and e is the elementary charge. The value of n_{eff} was taken equal to 10.8, as inferred from the data in refs.^{23, 29}. The electron (hole) μ_e (μ_h) mobility in Equation 1 is the real component due to the charge velocity in-phase with the THz field and averaged over the frequencies contained in the THz waveform (0.2 - 0.7 THz).

In our experiments the THz conductivity signal $S(t)$ was found to reach a maximum value at a pump probe delay time near 2 ps (see Figure 2.2 A) and to be merely constant up to 2.5 ps, so that $f_e(t)$ and $f_h(t)$ can be considered equal to unity on this timescale. To reduce the noise level, the quantum yield was obtained from $S(t)$ averaged over the time interval 2.0 ps - 2.5 ps, which is denoted as the initial THz conductivity

$$S_0 = \phi A N_a , \quad (2.2)$$

with $A = (\mu_e + \mu_h)e/2c\epsilon_0 n_{eff}$. According to Equation 2.2 the quantum yield of charge carriers, ϕ , can be obtained from the slope of a plot of S_0 versus N_a similar to previous studies.¹⁵⁻¹⁶ Note, that studies of CM on NCs in suspensions have in some cases been affected by photocharging effects that could be avoided by stirring.³⁰ Such effects do not play any role in our measurements, since we determine the CM efficiency from the THz conductivity due to free mobile charges directly after the pump laser pulse. Hence, normalization to an optical signal at longer times that may be too small due to presence of trapped charges (and thus leads to overestimation of the quantum yield) does not play a role. Our samples were found to be stable during the THz conductivity measurements and photodegrading did not occur.

2.1 Results and discussion

We studied CM in planar percolative PbSe networks with structure such as shown in the transmission electron microscope (TEM) image of Figure 2.1A (see Methods). Such networks have a thickness of 5.8 nm, which is equal to the diameter of the NCs from which they were prepared.^{20, 23} Similar to our previous work, the center-to-center distance between the NCs in the plane of the network is 6.4 ± 0.1 nm. The NCs are connected by crystalline necks of thickness 4.0 ± 0.4 nm and an average of 2.6 ± 0.7 necks per NC.²³ The entire percolative system thus forms a planar single rocksalt PbSe crystal with the [100] crystal axes being the principal axes. The attached NCs form straight segments with average length of about 20 nm. For comparison we also studied a thin film solid of PbSe NCs connected by 1,2-ethanediamine ligands with cubic ordering to some extent and relatively thin atomic necks between part of the NCs (see Methods).¹⁹ The NC solid has a thickness of about 55 ± 10 nm corresponding to 10 layers of NCs. Figure 2.1B shows a TEM image of a NC solid. It exhibits relatively thin necks between part of the NCs and it is more disordered than the percolative network. More details about the structure of such a NC solid can be found in refs 18, 19.

Figure 2.1C shows that the optical absorption spectra of the percolative PbSe network and the NC solid show a broadened peak at around 0.70 ± 0.01 eV. This peak is slightly red shifted from the first excitonic transition of PbSe NCs dispersed in tetrachloroethylene (see Figure 2.1C). This can be attributed to the electronic

coupling between NCs in the percolative network and the solid.²³ Photoluminescence from the percolative network and the NC solid could not be detected (see Methods), which implies that electrons and holes recombine predominantly non-radiatively. In what follows we take the energy of the peak absorption maximum as the band gap of the material; *i.e.* $E_g = 0.70$ eV. For the percolative network the tail at the low-energy side is less broad than for the NC solid. This may be due to the more ordered structure of the network and the smaller number of connections to other NCs in the two-dimensional network, as compared to the NC solid (see Figure 2.1A and B).

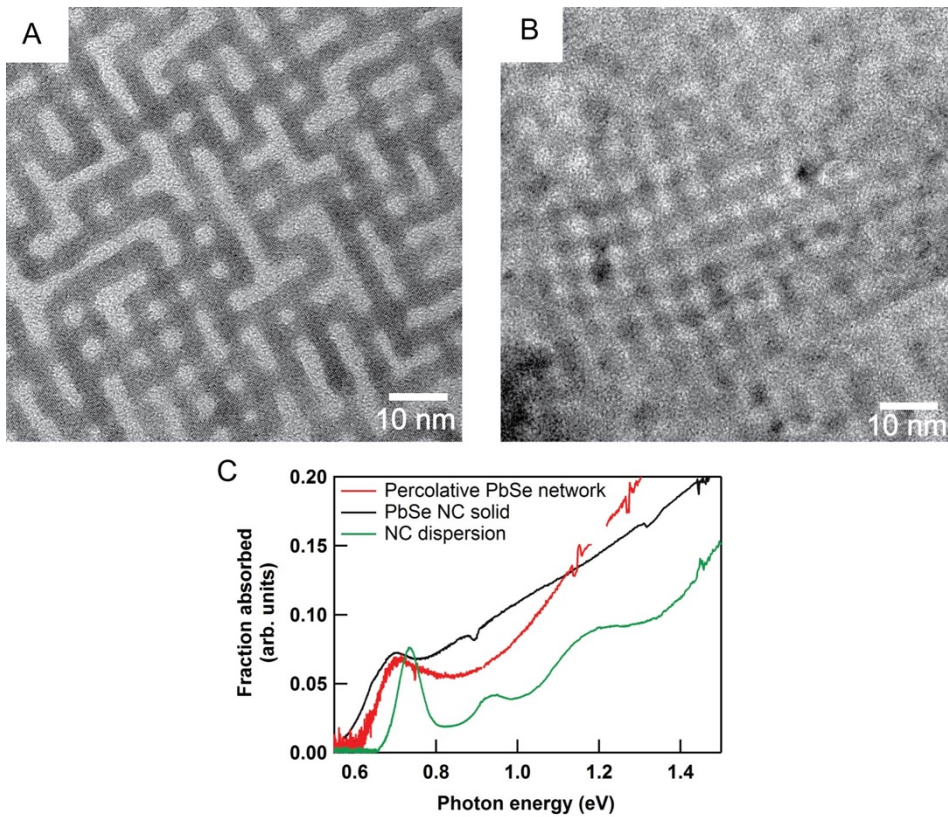


Figure 2.1. Structure and optical absorption. (A) TEM image of a monolayer percolative PbSe network (scale bar represents 10 nm). (B) TEM image of a NC solid (scale bar represents 10 nm). (C) Optical absorption spectra of a monolayer percolative PbSe network, the PbSe NC solid and a NC dispersion in tetrachloroethylene.

THz conductivity and quantum yield of charge carrier photogeneration. Figure 2.2 shows THz conductivity signals, $S(t)$, (see Methods) for the percolative PbSe network and the NC solid after excitation with pump photon energies of 1.08 eV and 0.77 eV, respectively. These photon energies are below twice the band gap so that

CM cannot occur. According to our previous studies, photoexcitation of these samples does not lead to a significant yield of neutral excitons and therefore the quantum yield of charge carriers can be considered equal to one; *i.e.* $\phi = 1$, see Methods Equations 1 and 2.^{18, 23} The THz conductivity signal is directly proportional to the sum of the time-dependent density of electrons and holes weighted by their mobility. The ~ 2 ps rise time of the THz conductivity signals in Figure 2.2 reflects the duration of the THz waveform. After the initial rise $S(t)$ is merely constant up to 2.5 ps for all pump fluences, so that charge trapping or recombination are insignificant and the survival fractions of electron and holes are equal to one; *i.e.* $f_e(t) = f_h(t) = 1$ for $t < 2.5$ ps, see Methods Equation 1. In agreement with this, the initial THz conductivity signal S_0 (obtained by averaging $S(t)$ between 2.0 and 2.5 ps, see Methods) increases linearly with pump fluence, see the insets in Figure 2.2A and 2B. Up to at least 6 ps the decay kinetics of the THz conductivity was found to be independent of pump photon energy, $h\nu$ (see Figure A1), from which we infer that cooling of charge carriers from higher energy to the band edge is so fast that it does not affect the decay kinetics monitored in this experiment. This agrees with charge cooling times less than 2 ps reported for PbSe NCs before.³¹⁻³² On a longer timescale of the order of 100 ps the charges decay by trapping or recombination, as discussed before.²³

The sum of the electron and hole mobilities, $\mu_e + \mu_h$, obtained from the data in Figure 2.2A for the percolative PbSe network is found to be $270 \pm 10 \text{ cm}^2 \text{V}^{-1} \text{s}^{-1}$, which is close to previous results.²³ For the PbSe NC solid the sum of the electron and hole mobilities obtained from the data in Figure 2.2B is $94 \pm 4 \text{ cm}^2 \text{V}^{-1} \text{s}^{-1}$. This value is higher than that reported by Guglietta *et al.*,¹⁷ which is due to the fact we used a higher refractive index for PbSe (see Methods) and could in addition result from preparing the NC solid *via* layer-by-layer dip-coating rather than spin-coating. The larger electronic coupling due to the broad crystalline necks between the NCs in the percolative PbSe network causes the mobility to be higher than in the NC solid, despite the smaller dimension of the network, between 2 and 1.

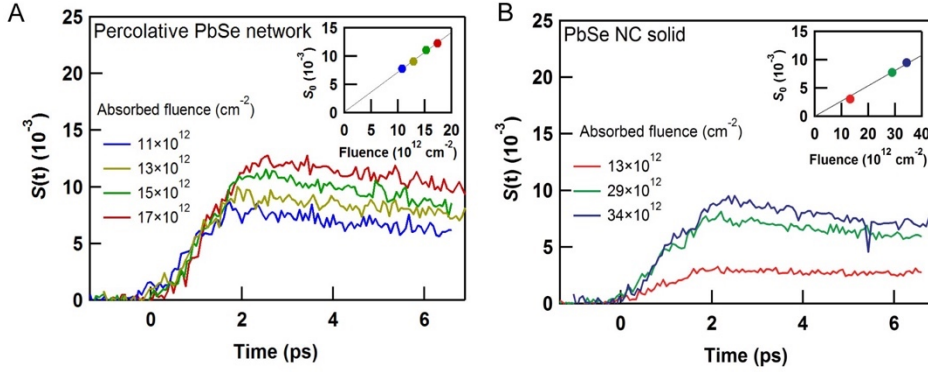


Figure 2.2. THz conductivity signal for different pump fluences. (A) THz conductivity signal induced by excitation of the percolative PbSe network at photon energy of 1.08 eV. (B) THz conductivity signal induced by excitation of the PbSe NC solid at photon energy 0.77 eV.

Determination of carrier multiplication efficiency. The CM efficiency was determined from measurements of the initial THz conductivity signal S_0 for different pump photon energies, $h\nu$, as a function of pump fluence, N_a , analogous to the data in the insets in Figure 2.2. A similar approach has been used previously to determine the CM efficiency in PbS nanosheets and in bulk PbS and PbSe.¹⁵⁻¹⁶ Figure 2.3A shows that the slope of S_0 versus N_a for the percolative PbSe network is the same for photon energies up to 1.30 eV (*i.e.* below $2E_g = 1.40$ eV). This is to be expected since at these energies the quantum yield $\phi = 1$. The slope exhibits increased values for photon energies of 1.55 eV and higher (*i.e.* above $2E_g$), which is due to a higher quantum yield as a result of CM. We determine the slope corresponding with unity quantum yield by averaging the slopes in plots of S_0 versus N_a for photon energies less than twice the band gap. The quantum yield at higher photon energies is then obtained from the relative values of the slopes. The quantum yields for the percolative PbSe network and the PbSe NC solid were obtained from linear fits to the measured values of S_0 versus N_a , shown in Figure A2. In Figure 2.3B we show the quantum yield as a function of photon energy, $h\nu$ (top axis), and as a function of photon energy normalised to the band gap, $h\nu/E_g$ (bottom axis).

Interestingly, Figure 2.3B shows that the onset of CM is near twice the band gap for both the percolative PbSe network and the PbSe NC solid. In addition, distinct step-like features appear in the quantum yield for the percolative network with

plateaus at photon energies in the range 1.5 eV – 2.0 eV ($2.1E_g - 2.9E_g$) and 2.0 eV – 2.6 eV ($2.9E_g - 3.7E_g$). At higher energies the CM efficiency increases linearly. These characteristics of the CM efficiency were reproduced for a second percolative PbSe network, see Figure A3. The PbSe NC solid exhibits a lower quantum yield with plateaus in the range 1.5 eV – 1.9 eV and 2.0 – 2.4 eV.

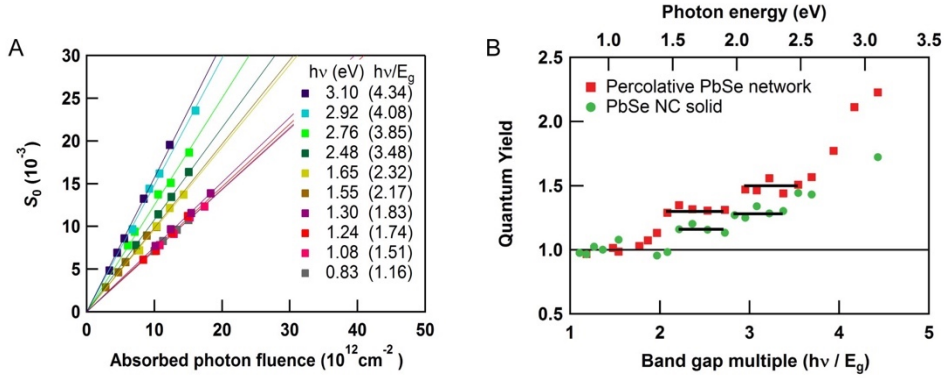


Figure 2.3. Initial THz conductivity and quantum yield for charge carrier photogeneration. (A) Initial THz conductivity of the percolative PbSe network *versus* absorbed pump fluence for photon energies as indicated. (B) Quantum yield as a function of band gap multiple ($h\nu/E_g$, bottom axis) and as a function of photon energy ($h\nu$, top axis) for the percolative PbSe network and the PbSe NC solid. The standard deviation in the quantum yields, as obtained from linear fits to experimental data as in Figure 2.3A (and Figure A2), is smaller than the data points.

Discussion of carrier multiplication efficiency. Ideal stair-case CM with the quantum yield increasing by one for each band gap multiple of the excess photon energy has been found for single-walled carbon nanotubes.³³ Such stair-case behavior has also been reported for silicon nanocrystals embedded in a silicondioxide matrix.³⁴ However, in the latter case the nanocrystals were not coupled, preventing charge transport and solar cell applications. The percolative network and the NC solid of the present study combine step-like CM with onset at twice the band gap with high charge mobility.

For lead chalcogenide NCs in dispersion the CM onset is at almost three times the band gap and step-like features have not been reported.^{9, 14} Interestingly, the CM onset in lead chalcogenide nanorods is lower than for NCs in dispersion with the lowest reported threshold energy being $2.23 E_g$.^{12, 14} Our percolative PbSe network is a planar crystal that can, somehow, be considered as a system of small NC rods of variable length (on average several PbSe NCs long) oriented and connected in two orthogonal [100] directions, see Figure 2.1A. This appears to reduce the CM

threshold energy to the absolute minimum of twice the band gap and lead to step-like features. CM at twice the band gap implies that the photon energy in excess of the band gap is fully converted into kinetic energy of one type of carrier only, either the photoexcited electron or the hole, as shown in the lower panel of Figure 2.4. The plateaus in the quantum yield *versus* photon energy in Figure 2.3 can be due to fast cooling of the electron (or hole) from higher energy in a series of electronic states to a lower state from which CM takes place prior to further cooling. The fact that the quantum yield does not increase up to 2.0 (see Figure 2.3) at photon energy of $2E_g$ can have different origins. First of all, it could be that not all photon absorption processes result in a fully asymmetric distribution of the photon energy, *i.e.* donate the excess energy to one type of charge carrier only. Possibly, part of the photons distribute their energy in excess of the band gap in a more symmetric way over the electron and the hole, as indicated in the upper panel of Figure 2.4. Secondly, thermal decay from the level of the CM precursor state might be at play. Interestingly, for PbS nanosheets the CM threshold was found to be at much higher band gap multiple¹⁵ than for the percolative PbSe network of the present work. It appears that the continuous nanosheets behave more like the bulk crystal in which CM has a higher threshold energy due to restrictions imposed by conservation of crystal momentum of the electrons involved in CM. The weakening of the rock salt periodicity in three orthogonal directions in the structure of a percolative network can relax these restrictions in favor of CM.

Insight into the occurrence of asymmetric electronic excitations, as shown in the lower panel of Figure 2.4, can be obtained from electronic structure calculations. To this end we considered a percolative network of 12x12 coupled NCs taken from the TEM image in Figure 2.1A. Electronic states of this network were calculated using $\mathbf{k} \cdot \mathbf{p}$ theory with a basis set corresponding to the two highest valence band states and the two lowest conduction band states at the L-point in the 1st Brillouin zone of PbSe.^{35, 36} This four band model did not yield a significant amount of asymmetric electronic excitations. Apparently, the electronic states resulting from mixing of the four band-edge states in the percolative network are to a large extent still resembling the almost symmetric energy dispersion of the valence and conduction bands in bulk PbSe. Hence, the four band-edge states at the L-point are insufficient to describe asymmetric excitations. A next step would be to include states along the Σ -path in the 1st Brillouin zone, or states at higher energy at the L-point.^{32, 37} It thus turns out that a proper description of CM in the percolative networks requires a more advanced theoretical approach, such as $\mathbf{k} \cdot \mathbf{p}$ theory with more electronic bands, or density functional theory with modern exchange/correlation functionals.

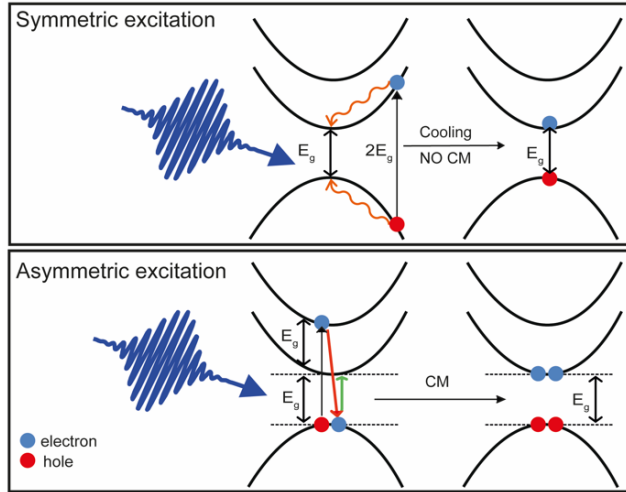


Figure 2.4. Photoexcitation and charge relaxation pathways. Upper panel: in a fully symmetric excitation at photon energy of twice the band gap, the excess energy is initially equally distributed between the electron (blue dot) and the hole (red dot), which subsequently relax by cooling to the band edges. Lower panel: in a fully asymmetric excitation the excess photon energy can be transferred to excite another electron *via* CM. In the example of this figure the electron in the second conduction band acquires the excess photon energy and subsequently relaxes *via* CM.

Enhancement of the allowable solar cell power conversion efficiency. Using the measured data in Figure 2.3B for the quantum yield *versus* band gap multiple, we calculated the power conversion efficiency (PCE) of a solar cell exposed to an AM 1.5 solar spectrum using the detailed-balance approach.³⁸⁻³⁹ All incident solar light at photon energy above the band gap was assumed to be absorbed. The results are shown in Figure 2.5, together with the Shockley-Queisser limit and the ideal staircase behaviour of CM. The CM efficiency in the PbSe NC solid does not significantly enhance the maximum PCE as compared to the Shockley-Queisser limit. However, the CM efficiency measured for the percolative PbSe network would enhance the maximum allowable PCE from $\sim 33\%$ with no CM to $\sim 37\%$ for the percolative network, a net increase of 4% (red curve in Figure 2.5). At a fixed band gap the increase in efficiency is greater. For a band gap of 0.7 eV the PCE increases from 24% without CM to 32% for the measured CM in the percolative network, an increase of $\sim 8\%$. Under concentration the PCE of all solar cells increases, however, when CM is present the increase in PCE is much higher than in the case of no CM.³ At a concentration of 500x the CM, measured in the percolative network, increases the PCE from 33% to 44% at 0.7 eV band gap.

Note, that the optical absorption spectrum of the percolative network in Figure 2.1C shows a tail below the band gap. This will reduce the PCE with respect to the calculated values given above.⁴⁰ To fully exploit CM, the networks should be improved to achieve a more narrow tail.

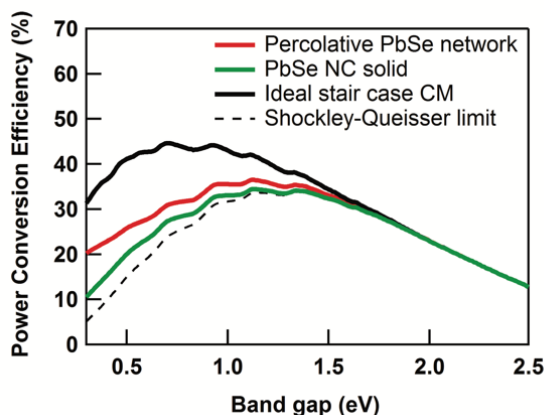


Figure 2.5. Simulated power conversion efficiency. Simulated power conversion efficiency of a solar cell exposed to an AM1.5 solar spectrum *versus* band gap for the percolative PbSe network and NC solid, together with the Shockley-Queisser limit and the ideal stair-case behaviour of CM. In the latter case the quantum yield increases by one each time the photon energy increases by an amount equal to the band gap.

2.3 Conclusions

In the percolative PbSe network the threshold photon energy for CM to occur was found to be equal to the minimum value of twice the band gap. At the threshold the quantum yield of charge carriers was found increase to about 1.4 and to exhibit a plateau as a function of photon energy. At higher photon energy the quantum yield exhibits a next step-like feature followed by a linear increase. Qualitatively similar results were obtained for a NC solid with organic ligands and thin atomic necks between part of the NCs. The PCE of a solar cell would be enhanced significantly by the CM efficiency found for the percolative PbSe network.

References

1. Beard, M. C.; Luther, J. M.; Semonin, O. E.; Nozik, A. J. Third Generation Photovoltaics Based on Multiple Exciton Generation in Quantum Confined Semiconductors. *Acc. Chem. Res.* **2013**, *46*, 1252–1260.
2. Davis, N. J.; Bohm, M. L.; Tabachnyk, M.; Wisnivesky-Rocca-Rivarola, F.; Jellicoe, T. C.; Ducati, C.; Ehrler, B.; Greenham, N. C. Multiple-Exciton Generation in Lead Selenide Nanorod Solar Cells with External Quantum Efficiencies Exceeding 120%. *Nat. Commun.* **2015**, *6*, 8259.
3. Hanna, M. C.; Beard, M. C.; Nozik, A. J. Effect of Solar Concentration on the Thermodynamic Power Conversion Efficiency of Quantum-Dot Solar Cells Exhibiting Multiple Exciton Generation. *J. Phys. Chem. Lett.* **2012**, *3*, 2857–2862.
4. Nozik, A. J. Quantum Dot Solar Cells. *Phys. E* **2002**, *14*, 115–120.
5. Semonin, O. E.; Luther, J. M.; Choi, S.; Chen, H. Y.; Gao, J.; Nozik, A. J.; Beard, M. C. Peak External Photocurrent Quantum Efficiency Exceeding 100% via MEG in a Quantum Dot Solar Cell. *Science* **2011**, *334*, 1530–1533.
6. Ten Cate, S.; Sandeep, C. S.; Liu, Y.; Law, M.; Kinge, S.; Houtepen, A. J.; Schins, J. M.; Siebbeles, L. D. A. Generating Free Charges by Carrier Multiplication in Quantum Dots for Highly Efficient Photovoltaics. *Acc. Chem. Res.* **2015**, *48*, 174–181.
7. Trinh, M. T.; Houtepen, A. J.; Schins, J. M.; Hanrath, T.; Piris, J.; Knulst, W.; Goossens, A. P.; Siebbeles, L. D. A. In Spite of Recent Doubts Carrier Multiplication Does Occur in PbSe Nanocrystals. *Nano Lett.* **2008**, *8*, 1713–1718.
8. Ellingson, R. J.; Beard, M. C.; Johnson, J. C.; Yu, P.; Micic, O. I.; Nozik, A. J.; Shabaev, A.; Efros, A. L. Highly Efficient Multiple Exciton Generation in Colloidal PbSe and PbS Quantum Dots. *Nano Lett.* **2005**, *5*, 865–871.
9. Smith, C.; Binks, D. Multiple Exciton Generation in Colloidal Nanocrystals. *Nanomaterials* **2013**, *4*, 19–45.
10. Aerts, M.; Suchand Sandeep, C. S.; Gao, Y.; Savenije, T. J.; Schins, J. M.; Houtepen, A. J.; Kinge, S.; Siebbeles, L. D. A. Free Charges Produced by Carrier Multiplication in Strongly Coupled PbSe Quantum Dot Films. *Nano Lett.* **2011**, *11*, 4485–4489.
11. Sandeep, C. S.; ten Cate, S.; Schins, J. M.; Savenije, T. J.; Liu, Y.; Law, M.; Kinge, S.; Houtepen, A. J.; Siebbeles, L. D. A. High Charge-Carrier Mobility Enables Exploitation of Carrier Multiplication in Quantum-Dot Films. *Nat. Commun.* **2013**, *4*, 2360.
12. Cunningham, P. D.; Boercker, J. E.; Foos, E. E.; Lumb, M. P.; Smith, A. R.; Tischler, J. G.; Melinger, J. S. Enhanced Multiple Exciton Generation in Quasi-One-Dimensional Semiconductors. *Nano Lett.* **2011**, *11*, 3476–3481.

13. Padilha, L. A.; Stewart, J. T.; Sandberg, R. L.; Bae, W. K.; Koh, W. K.; Pietryga, J. M.; Klimov, V. I. Aspect Ratio Dependence of Auger Recombination and Carrier Multiplication in PbSe Nanorods. *Nano Lett.* **2013**, *13*, 1092–1099.
14. Padilha, L. A.; Stewart, J. T.; Sandberg, R. L.; Bae, W. K.; Koh, W. K.; Pietryga, J. M.; Klimov, V. I. Carrier Multiplication in Semiconductor Nanocrystals: Influence of Size, Shape, and Composition. *Acc. Chem. Res.* **2013**, *46*, 1261–1269.
15. Aerts, M.; Bielewicz, T.; Klinke, C.; Grozema, F. C.; Houtepen, A. J.; Schins, J. M.; Siebbeles, L. D. A. Highly Efficient Carrier Multiplication in PbS Nanosheets. *Nat. Commun.* **2014**, *5*, 3789.
16. Pijpers, J. J. H.; Ulbricht, R.; Tielrooij, K. J.; Osherov, A.; Golan, Y.; Delerue, C.; Allan, G.; Bonn, M. Assessment of Carrier-Multiplication Efficiency in Bulk PbSe and PbS. *Nat. Phys.* **2009**, *5*, 811–814.
17. Guglietta, G. W.; Diroll, B. T.; Gaulding, E. A.; Fordham, J. L.; Li, S.; Murray, C. B.; Baxter, J. B. Lifetime, Mobility, and Diffusion of Photoexcited Carriers in Ligand-Exchanged Lead Selenide Nanocrystal Films Measured by Time-Resolved Terahertz Spectroscopy. *ACS Nano* **2015**, *9*, 1820–1828.
18. Talgorn, E.; Gao, Y.; Aerts, M.; Kunneman, L. T.; Schins, J. M.; Savenije, T. J.; van Huis, M. A.; van der Zant, H. S.; Houtepen, A. J.; Siebbeles, L. D. A. Unity Quantum Yield of Photogenerated Charges and Band-Like Transport in Quantum-Dot Solids. *Nat. Nanotechnol.* **2011**, *6*, 733–739.
19. Sandeep, C. S.; Azpiroz, J. M.; Evers, W. H.; Boehme, S. C.; Moreels, I.; Kinge, S.; Siebbeles, L. D. A.; Infante, I.; Houtepen, A. J. Epitaxially Connected PbSe Quantum-Dot Films: Controlled Neck Formation and Optoelectronic Properties. *ACS Nano* **2014**, *8*, 11499–11511.
20. Evers, W. H.; Goris, B.; Bals, S.; Casavola, M.; de Graaf, J.; van Roij, R.; Dijkstra, M.; Vanmaekelbergh, D. Low-Dimensional Semiconductor Superlattices Formed by Geometric Control over Nanocrystal Attachment. *Nano Lett.* **2013**, *13*, 2317–2323.
21. Geuchies, J. J.; van Overbeek, C.; Evers, W. H.; Goris, B.; de Backer, A.; Gantapara, A. P.; Rabouw, F. T.; Hilhorst, J.; Peters, J. L.; Konovalov, O.; Petukhov, A. V.; Dijkstra, M.; Siebbeles, L. D. A.; van Aert, S.; Bals, S.; Vanmaekelbergh, D. *In Situ* Study of the Formation Mechanism of Two-Dimensional Superlattices from PbSe Nanocrystals. *Nat. Mater.* **2016**, *15*, 1248–1254.
22. Boneschanscher, M. P.; Evers, W. H.; Geuchies, J. J.; Altantzis, T.; Goris, B.; Rabouw, F. T.; van Rossum, S. A.; van der Zant, H. S.; Siebbeles, L. D. A.; Van Tendeloo, G.; Swart, I.; Hilhorst, J.; Petukhov, A. V.; Bals, S.; Vanmaekelbergh, D. Long-Range Orientation and Atomic Attachment of Nanocrystals in 2D Honeycomb Superlattices. *Science* **2014**, *344*, 1377–1380.

23. Evers, W. H.; Schins, J. M.; Aerts, M.; Kulkarni, A.; Capiod, P.; Berthe, M.; Grandidier, B.; Delerue, C.; van der Zant, H. S.; van Overbeek, C.; Peters, J. L.; Vanmaekelbergh, D.; Siebbeles, L. D. A. High Charge Mobility in Two-Dimensional Percolative Networks of PbSe Quantum Dots Connected by Atomic Bonds. *Nat. Commun.* **2015**, *6*, 8195.
24. Steckel, J. S.; Yen, B. K.; Oertel, D. C.; Bawendi, M. G. On the Mechanism of Lead Chalcogenide Nanocrystal Formation. *J. Am. Chem. Soc.* **2006**, *128*, 13032–13033.
25. Ulbricht, R.; Hendry, E.; Shan, J.; Heinz, T. F.; Bonn, M. Carrier Dynamics in Semiconductors Studied with Time-Resolved Terahertz Spectroscopy. *Rev. Mod. Phys.* **2011**, *83*, 543–586.
26. Lloyd-Hughes, J.; Jeon, T. I. A Review of the Terahertz Conductivity of Bulk and Nano-Materials. *J. Infrared, Millimeter, Terahertz Waves* **2012**, *33*, 871–925.
27. Murphy, J. E.; Beard, M. C.; Nozik, A. J. Time-Resolved Photoconductivity of PbSe Nanocrystal Arrays. *J. Phys. Chem. B* **2006**, *110*, 25455–25461.
28. Hendry, E.; Koeberg, M.; Schins, J. M.; Nienhuys, H. K.; Sundstrom, V.; Siebbeles, L. D. A.; Bonn, A. Interchain Effects in the Ultrafast Photophysics of a Semiconducting Polymer: THz Time-Domain Spectroscopy of Thin Films and Isolated Chains in Solution. *Phys. Rev. B* **2005**, *71*, 125201.
29. Hyun, B. R.; Bartnik, A. C.; Koh, W. K.; Agladze, N. I.; Wrubel, J. P.; Sievers, A. J.; Murray, C. B.; Wise, F. W. Far-Infrared Absorption of PbSe Nanorods. *Nano Lett.* **2011**, *11*, 2786–2790.
30. McGuire, J. A.; Sykora, M.; Joo, J.; Pietryga, J. M.; Klimov, V. I. Apparent versus True Carrier Multiplication Yields in Semiconductor Nanocrystals. *Nano Lett.* **2010**, *10*, 2049–2057.
31. Spoor, F. C.; Kunneman, L. T.; Evers, W. H.; Renaud, N.; Grozema, F. C.; Houtepen, A. J.; Siebbeles, L. D. A. Hole Cooling Is Much Faster Than Electron Cooling in PbSe Quantum Dots. *ACS Nano* **2016**, *10*, 695–703.
32. Spoor, F. C. M.; Tomic, S.; Houtepen, A. J.; Siebbeles, L. D. A. Broadband Cooling Spectra of Hot Electrons and Holes in PbSe Quantum Dots. *ACS Nano* **2017**, *11*, 6286–6294.
33. Gabor, N. M.; Zhong, Z.; Bosnick, K.; Park, J.; McEuen, P. L. Extremely Efficient Multiple Electron-Hole Pair Generation in Carbon Nanotube Photodiodes. *Science* **2009**, *325*, 1367–1371.
34. Timmerman, D.; Valenta, J.; Dohnalová, K.; de Boer, W. D. A. M.; Gregorkiewicz, T. Step-Like Enhancement of Luminescence Quantum Yield of Silicon Nanocrystals. *Nat. Nanotechnol.* **2011**, *6*, 710–713.
35. Kang, I.; Wise, F. W. Electronic Structure and Optical Properties of PbS and PbSe Quantum Dots. *J. Opt. Soc. Am. B* **1997**, *14*, 1632–1646.

36. Aeberhard, U.; Vaxenburg, R.; Lifshitz, E.; Tomic, S. Fluorescence of Colloidal PbSe/PbS QDs in NIR Luminescent Solar Concentrators. *Phys. Chem. Chem. Phys.* **2012**, *14*, 16223–16228.
37. An, J. M.; Franceschetti, A.; Dudiy, S. V.; Zunger, A. The Peculiar Electronic Structure of PbSe Quantum Dots. *Nano Lett.* **2006**, *6*, 2728–2735.
38. Beard, M. C.; Midgett, A. G.; Hanna, M. C.; Luther, J. M.; Hughes, B. K.; Nozik, A. J. Comparing Multiple Exciton Generation in Quantum Dots to Impact Ionization in Bulk Semiconductors: Implications for Enhancement of Solar Energy Conversion. *Nano Lett.* **2010**, *10*, 3019–3027.
39. Hanna, M. C.; Nozik, A. J. Solar Conversion Efficiency of Photovoltaic and Photoelectrolysis Cells with Carrier Multiplication Absorbers. *J. Appl. Phys.* **2006**, *100*, 074510.
40. Jean, J.; Mahony, T. S.; Bozyigit, D.; Sponseller, M.; Holovsky, J.; Bawendi, M. G.; Bulović, V. Radiative Efficiency Limit with Band Tailing Exceeds 30% for Quantum Dot Solar Cells. *ACS Energy Lett.* **2017**, *2*, 2616–2624.

Appendix A

1. Normalized THz conductivity at various photon energies.

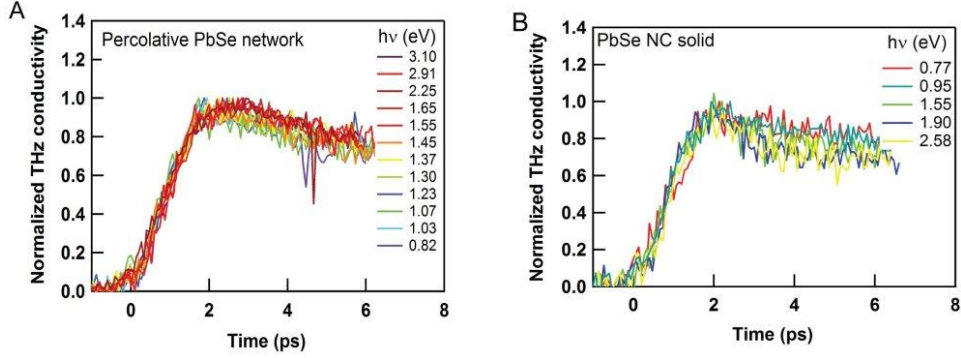


Figure A1. THz conductivity at various photon energies. (A) Normalized THz conductivity decay kinetics obtained by photoexciting the percolative PbSe network at photon energies as indicated and absorbed fluence near 10^{13} cm^{-2} . (B) Analogous results for the PbSe NC solid.

2. Determination of carrier multiplication efficiency.

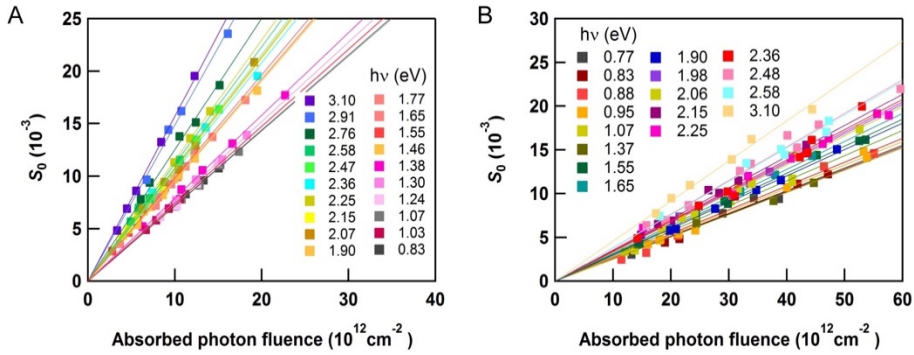


Figure A2. Determination of carrier multiplication efficiency. (A) Initial THz conductivity of the percolative PbSe network versus absorbed pump fluence for photon energies as indicated. (B) Analogous results for the PbSe QD solid.

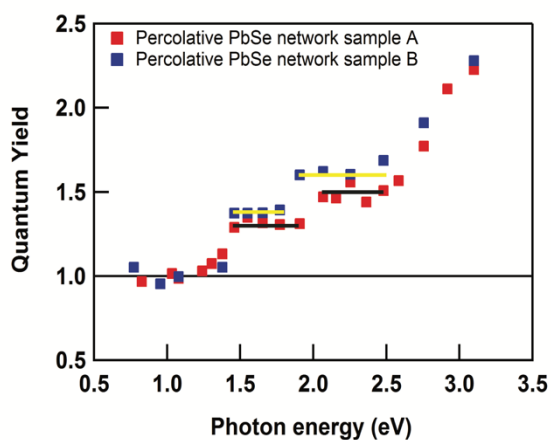
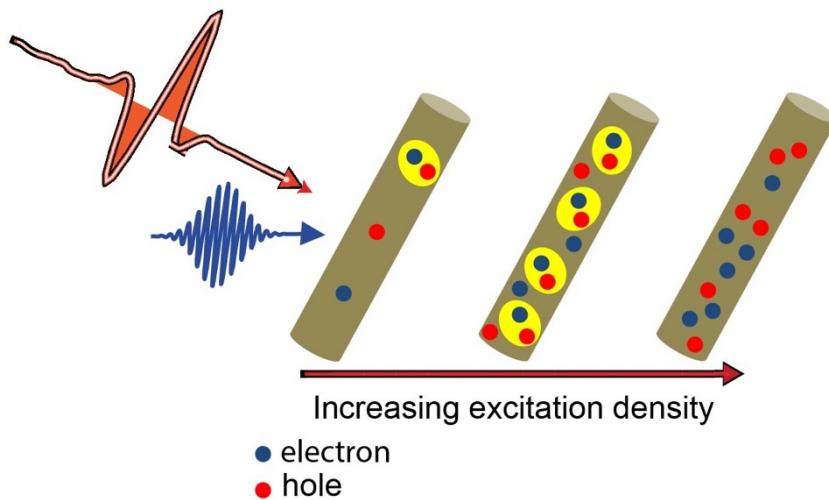


Figure A3. Comparison of quantum yield in percolative PbSe networks. Quantum yield as a function of photon energy for two percolative PbSe network samples denoted as A and B. The horizontal bars guide the eye to the plateaus in the quantum yield. The standard deviation in the quantum yields, as obtained from linear fits to data as in Figure A2, are smaller than the data points.

Chapter 3

Photogeneration Quantum Yield and Character of Free Charges and Excitons in PbSe Nanorods



Based on:

Photogeneration Quantum Yield and Character of Free Charges and Excitons in PbSe Nanorods.

Aditya Kulkarni, Wiel H. Evers, Thomas P. van Waas, and Laurens D. A. Siebbeles.

In preparation.

3.1 Introduction.

Nanorods of PbSe are of interest due to the possibility to tune their band gap from far to near infrared by decrease of their radius. A band gap close to 1 eV can be realized, which is ideal for solar cells, near infrared detectors and lasers.¹⁻³ Interestingly, it has been found that a single energetic photon can excite two or more electrons in PbSe nanorods via a process known as carrier multiplication (CM).^{1, 4} The effect of CM in solar cells based on PbSe nanorods was found to lead to an external quantum efficiency close to 120%.²

For optoelectronic applications as mentioned, above it is important to understand to what extent photon absorption leads to formation of free electrons and holes, or mutually bound electrons and holes in the form of neutral excitons. According to the Saha model the quantum yield of excitons increases at higher total photoexcitation density.⁵⁻⁷ At higher photoexcitation density it is more likely that electrons and holes recombine to form excitons, as described by the Saha equilibrium constant. At very high density where the distance between excitons becomes comparable to their diameter, their spatial overlap causes screening of the electron-hole (e-h) Coulomb attraction, which can lead to dissociation of excitons into free charges forming an e-h plasma.^{6, 8} Understanding the nature of photoexcited species as a function of density is of interest from a fundamental perspective, as well as for optoelectronic applications of PbSe nanorods.

Theoretical calculations on PbSe nanowires have yielded exciton binding energies that strongly increase as their radius goes down, with a value as high as 0.4 eV for a radius near 1 nm.⁹ Transient optical absorption (TA) and photoluminescence measurements do not directly reveal if photoexcitation leads to free charges or neutral excitons.^{1, 4, 10} However, according to theoretical analysis of the TA decay kinetics excitons are the dominant species in longer PbSe nanorods.^{10, 11}

The aim of the current work is to determine to what extent photoexcitation of PbSe nanorods leads to free charges or excitons and to determine the charge carrier mobility and the exciton polarizability. We combine time-resolved TA spectroscopy with terahertz (THz) photoconductivity measurements for different photoexcitation densities to distinguish free charges from excitons. From analysis of the TA and THz photoconductivity data it is inferred that photoexcitation leads predominantly to formation of excitons with a polarizability of $10^{-35} \text{ Cm}^2\text{V}^{-1}$. The quantum yield of photogenerated free charges is rather small. The sum of the mobility of an electron and hole moving in phase with the THz electric field is as high as $91 \pm 13 \text{ cm}^2\text{V}^{-1}\text{s}^{-1}$. For higher photoexcitation density the photoconductivity is strongly affected by

mutual interactions between charges and excitons, leading to a lower charge mobility and a reduction of the yield of excitons.

3.2 Materials and methods

Sample preparation. PbSe nanorods were synthesized by following a previously reported procedure.¹²

Transient absorption spectroscopy. The PbSe nanorod dispersion was photoexcited with 800 nm optical pulses of width 180 fs and the reduced absorption (bleach) near the band gap due to presence of free electrons, holes and excitons was probed by broadband optical pulses, generated in a sapphire crystal using the laser system described in ref. 7. The bleach of the low energy absorption peak (see Figure B1) was obtained from the transmitted probe light in the presence of pump (I_{on}) and the absence of pump pulse (I_{off}) using the relation¹³

$$\Delta OD = \log \left(\frac{I_{off}(\lambda)}{I_{on}(\lambda)} \right). \quad (3.1)$$

The measured bleach was averaged in the range of 1100 nm – 1600 nm to cover the entire bleach spectrum at each pump-probe delay time and to obtain time dependent traces.

Optical pump-THz probe spectroscopy. The PbSe nanorod dispersion was photoexcited with 800 nm optical pump pulses of width 60 fs. The photogenerated free e-h pairs and excitons were probed by single cycle THz pulses. Single-cycle THz pulses were generated in a non-linear crystal ZnTe *via* optical rectification of 60 fs pulses of wavelength 800 nm similar to our previous work.^{14, 15} The THz pulse was detected in a ZnTe crystal by spatially overlapping it with a chirped optical laser pulse centered at 800 nm, so that the entire THz waveform is detected by a single laser shot.^{14, 15} The differential THz signal $\Delta E(\omega, t)$ at time t after the pump pulse was obtained from the Fourier transformed electrical field of the transmitted THz pulse in the presence and absence $E_0(\omega)$ of optical pumping. The complex THz conductivity, $(\Delta\sigma)$ is related to the differential THz signal $\Delta E(\omega, t)$ according to^{14, 16, 17}

$$\frac{\Delta E(\omega, t)}{E_0(\omega)} = \frac{L\Delta\sigma}{2n_{sol}c\epsilon_0}, \quad (3.2)$$

with L the sample thickness, $n_{sol} = 1.5$ the refractive index of the solvent, c the speed of light in vacuum, ϵ_0 the vacuum permittivity.

The real part of THz conductivity signal, $S_R(t)$, is related to the quantum yield (*i.e.* the number of electron hole pairs per absorbed photon, $\phi(t)$, present at time t after the pump pulse) and the sum of the real component of the electron and hole mobility $\mu_e + \mu_h \equiv \mu_R$ for charge moving along the direction of the nanorod according to^{14, 16}

$$S_R(t) = \phi(t)\mu_R = R \frac{L\Delta\sigma_R}{eN_a}, \quad (3.3)$$

with e the elementary charge and N_a the number of absorbed photons per unit area in the nanorod dispersion (the excitation density). The factor R takes effects of the angle between the polarization direction of the pump laser pulse and the direction of the THz electric field with respect to the randomly oriented axes of the nanorods into account. The transition dipole moment for an optical transition is parallel or perpendicular to the axis of the nanorod, so that the optical absorption cross section of a nanorod depends on the angle Θ of its axis with respect to the pump polarization direction according to $\cos^2(\Theta)$ or $\sin^2(\Theta)$, respectively. Assuming the THz conductivity perpendicular to the axis of a nanorod to be negligible, the THz conductivity of a nanorod at angle Ω with the THz field is proportional to $\cos^2(\Omega)$. Taking this into account the factor R can be determined from the ratio of THz conductivity measured with the pump laser polarization parallel and perpendicular to the THz field, respectively. From such measurements it was found that $R = 3.3$. The imaginary conductivity signal $S_I(t)$ due to free electrons and holes, as well as the polarizability of excitons along the direction of the nanorod is given by

$$S_I(t) = \phi(t)\mu_I + [1 - \phi(t)] \frac{\alpha\omega}{e} = R \frac{L\Delta\sigma_I}{eN_a}, \quad (3.4)$$

with μ_I the sum of the imaginary electron and hole mobility, α the polarizability of an exciton and ω the radian frequency of the THz field.

3.3 Results and discussion

PbSe nanorods were synthesized by following a previously reported procedure.¹² According to analysis of the Transmission Electron Microscopy (TEM) image in Figure 3.1A the nanorods have diameter 4.0 ± 0.8 nm and length 51 ± 11 nm. The nanorods were dispersed in tetrachloroethylene for all spectroscopic measurements discussed below. The optical absorption spectrum of the PbSe nanorod dispersion is shown in Figure 3.1B. The absorption peak at lowest photon energy is maximum at 1395 nm.

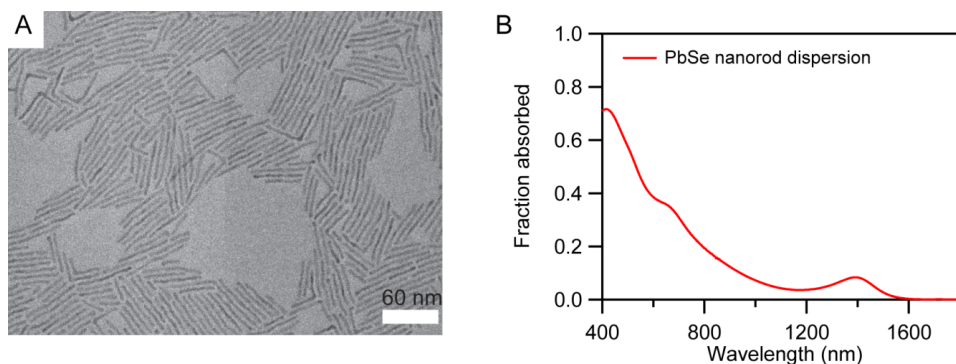


Figure 3.1. Structural and optical characterization. (A) TEM image of PbSe nanorods (the scale bar represents 60 nm). (B) Optical absorption spectrum of the PbSe nanorod dispersion exhibiting a low energy absorption peak at 1395 nm.

Transient optical absorption spectroscopy. Figure 3.2A shows the time-dependent bleach, ΔOD , obtained by averaging the measured bleach between 1100 nm and 1600 nm after photoexciting the PbSe nanorod dispersion with 800 nm pump pulses with duration of 180 fs (see Methods and Figure 3.2A). As expected the initial amplitude of the bleach increases with the excitation density (defined as the number of absorbed pump photons per unit area in the nanorod dispersion), while the decay becomes faster (additional data in Figure B2). For the lowest excitation density the bleach exhibits no decay on the 2.5 ns timescale considered. This can be understood since a single free electron-hole (e-h) pair, or a single neutral exciton, decay on a longer timescale.^{11, 18} At higher excitation densities the initial bleach on short time increases, which reflects the presence of a larger number of free e-h pairs and/or excitons. The faster decay at higher density is due to Auger recombination, which occurs when multiple e-h pairs and/or excitons are present in a nanorod.^{4, 10, 11, 19}

Figure 3.2B shows the bleach normalized to the maximum value in a short time range of 5-10 ps. The rise of the bleach during time is due to energetic relaxation (cooling) of the initially hot electrons and holes to the band gap. At the lowest excitation density this is observed to occur within a ps, similar to previous results.¹⁰ With increasing density cooling appears to be prolonged and takes about 4 ps at the highest density. This can be understood as follows.²⁰ Cooling of charge carriers occurs by emission of phonons. At higher charge carrier density, a larger number of phonons are emitted, and the nuclear lattice heats up more than for low density. Hence, at higher density reabsorption of phonons by charge carriers is more likely and the cooling time becomes longer.

The initial average number of free e-h pairs and excitons in semiconductor nanorods can be determined from the ratio of the maximum bleach amplitude, A, at short time after photoexcitation and the bleach at long time, B, when Auger recombination is complete and a single e-h pair or exciton is left in a photoexcited nanorod.^{4, 21, 22} In Figure 3.2C values of A are shown, as obtained by averaging the bleach over a time range of 5-10 ps, which is sufficiently long after the pump pulse so that charges have cooled to the band edge. The values of B in Figure 3.2C were obtained by averaging over 2.0-2.5 ns, during which the bleach in Figure 3.2A can be attributed to single e-h pairs or excitons, since it exhibits no significant decay. The values of A first increase linearly with excitation density, reflecting that the number of e-h pairs and excitons is directly proportional to the excitation density. At higher excitation density the increase becomes sublinear, which is attributed to decay by Auger recombination on a timescale shorter than 10 ps. The value of B at first increases with excitation density due to the fact that more nanorods are photoexcited and eventually saturates when all nanorods are excited and thus contain one e-h pair or exciton on longer times.

Figure 3.2D shows the ratio A/B as a function of the incident (bottom-axis) and absorbed (top-axis) number of photons per unit area. The ratio A/B is equal to the average initial number, N_i , of e-h pairs and excitons per *photoexcited* nanorod in the time range 5-10 ps. The value of N_i is equal to the average number of absorbed photons per *photoexcited* nanorod, N_0 , provided the density of e-h pairs and excitons in the nanorods is sufficiently low so that Auger recombination on times less than 10 ps is insignificant. The number of absorbed photons per nanorod is a Poisson distribution, so that the average initial number of e-h pairs and excitons per nanorod is equal to , with j_0 the number of incident pump photons per unit area and σ_{abs} the absorption cross section at the pump wavelength of 800 nm. The initial average number of e-h pairs and excitons per *photoexcited* nanorod is then equal to

$$N_0 = \frac{j_0 \sigma_{abs}}{(1 - e^{-j_0 \sigma_{abs}})} \quad (3.5)$$

Fitting equation 3.5 to the ratio A/B for those densities at which A increases linearly with the excitation density (so that Auger recombination does not affect A) yields the black curve in Figure 3.2D with $\sigma_{abs} = (5.0 \pm 0.4) \times 10^{-14} \text{ cm}^2$. At higher excitation density A/B is smaller than N_0 , which is attributed to decay of e-h pairs and excitons by Auger recombination on a timescale shorter than 10 ps.

For the value of σ_{abs} at 800 nm obtained from the fit, the optical absorption spectrum in Figure 3.1B yields an absorption cross section at the maximum of the low energy peak equal to $2 \times 10^{-14} \text{ cm}^2$. Cunningham *et al.* reported a cross section of $7.2 \times 10^{-15} \text{ cm}^2$ at the low energy peak for PbSe nanorods with volume 240 nm^3 .¹⁹ Taking our value of σ_{abs} at the low energy peak and assuming it to scale linearly with the nanorod volume (640 nm^3 for our nanorods),^{4, 19} yields an absorption cross section of $7.5 \times 10^{-15} \text{ cm}^2$ for nanorods of volume 240 nm^3 , which agrees with the value reported by Cunningham *et al.*¹⁹

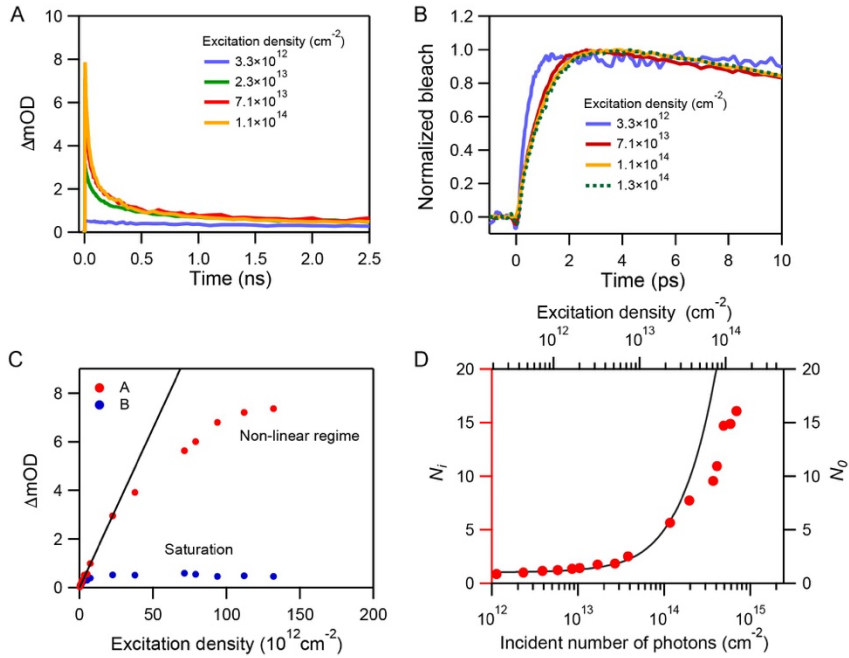


Figure 3.2. TA spectroscopy results. (A) ΔOD obtained by averaging the measured bleach in the range 1100-1600 nm near the band gap after photoexcitation at 800 nm. (B) The bleach rises more slowly during time at higher excitation density. (C) Initial bleach signal, A, obtained by averaging over a time range of 5-10 ps and the long-time bleach, B, obtained by averaging over 2.0-2.5 ns plotted *versus* the excitation density. (D) Values of $N_i = A/B$ (red markers plotted against left-axis) and N_0 (black curve plotted against right-axis) as a function of incident photons per cm^2 , j_0 , (bottom-axis) and the excitation density (top-axis).

THz spectroscopy. We conducted THz photoconductivity experiments to determine to what extent photoexcitation leads to formation of free e-h pairs and neutral excitons.

Figure 3.3 shows THz photoconductivity data obtained by photoexcitation of the PbSe nanorods with 800 nm pump pulses of duration 60 fs. The real component of the THz conductivity is due to motion of charges with velocity in-phase with the THz field and the imaginary part of the THz conductivity is due to the out-of-phase velocity resulting from backscattering of charges and the polarizability of excitons (See Methods).^{16, 17, 23}

Figure 3.3A shows the real (positive) and imaginary (negative) components of the differential THz signal averaged over frequencies ($f = \omega / 2\pi$) in the range 0.5-1.2 THz, as a function of time after the 800 nm pump pulse. The differential THz signal is directly proportional to the conductivity, or equivalently the density of e-h pairs and excitons weighted by their mobility and polarizability, respectively (see Methods). The real component is attributed to the presence of free mobile charge carriers only. Excitons will not contribute to the real component, since the calculated exciton binding energy in PbSe nanowires of diameter 4 nm is as high as 0.154 eV (see ref. ⁹), and consequently excitation to a higher exciton level will largely exceed the THz photon energy (1 THz = 4 meV). At higher excitation density the imaginary THz signal decays faster than the real component. This must be due to the fact that excitons also contribute to the imaginary component. Hence, from the data in Figure 3.3A we can conclude that both e-h pairs and excitons are produced by photoexcitation.

Figure 3.3B shows the real component of the product of the quantum yield of e-h pairs, $\phi(t)$, and the sum of the mobility of an electron and a hole; *i.e.* $S_R(t) = \phi(t)\mu_R$. Note, the quantum yield is the number of e-h pairs per absorbed pump photon at time t after the pump pulse. It can be seen that S_R decays faster at higher excitation density, which is due to enhanced Auger recombination of charges. The reduction of

the magnitude of S_R with excitation density can result from a decrease of the quantum yield of charges and/or a reduction of the charge mobility at higher density. This will be addressed further in the next section. The initial values of the quantum yield weighted real mobility averaged over t in the interval 5-10 ps, $S_{R,i}$, are shown in Figure 3.3C as a function of the average initial number of e-h pairs and excitons per nanorod, N_i .

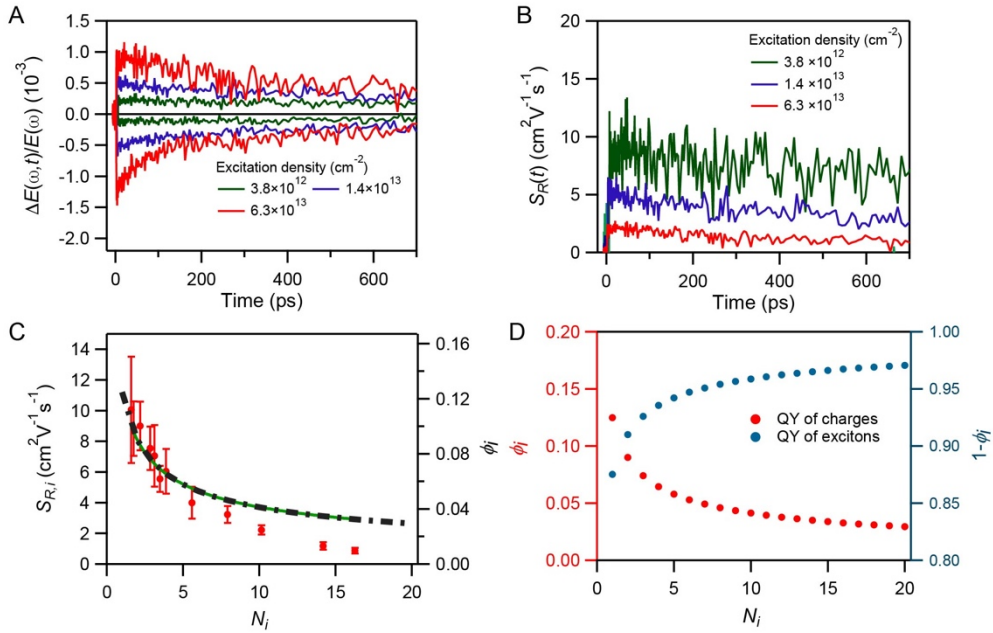


Figure 3.3. THz photoconductivity results. (A) Real (positive) and imaginary (negative) differential THz signal after photoexcitation at 800 nm for excitation densities as indicated. (B) Quantum yield weighted real mobility of free charges obtained from the data in Figure 3.3A. (C) Initial quantum yield weighted real mobility of charges, $S_{R,i}$, (red markers) and product of the quantum yield calculated from the Saha model and the fitted mobility of charges. (D) Quantum yields of charges and excitons *versus* N_i calculated from the Saha model.

Quantum yield and mobility of charges and polarizability of excitons. The thermodynamic equilibrium between e-h pairs and excitons can be described by the 1D Saha model. Focusing on the initial THz conductivity we can relate the density of free charges in a nanorod $n_q = \phi_i N_i / L$ and excitons $n_x = (1 - \phi_i) N_i / L$ by²⁴

$$\frac{n_q^2}{n_x} = K = \left(\frac{2m^* k_B T}{\pi \hbar^2} \right)^{1/2} \exp\left(\frac{-E_x}{k_B T}\right), \quad (3.6)$$

with ϕ_i the quantum yield of e-h pairs averaged over 5-10 ps after the pump pulse,

$m^* = 0.112 m_0$ the reduced effective mass of electrons and holes obtained from the calculated valence and conduction band dispersion (see Appendix B4) reported in literature.⁹ $E_x = 0.154$ eV is the calculated exciton binding energy from literature,⁹ k_B is the Boltzmann constant, \hbar is the reduced Planck constant and $T = 293$ K. Using equation 2 the quantum yield of e-h pairs is found to be $\phi_i = \frac{-KL}{2N_i} \left(1 - \sqrt{1 + \frac{4N_i}{KL}} \right)$.

Fitting the product $\phi_i \mu_R$ to the data in Figure 3.3C with K calculated from equation 2 and the mobility of an e-h pair as adjustable parameter yields $\mu_R = 91 \pm 13 \text{ cm}^2 \text{V}^{-1} \text{s}^{-1}$. The fit reproduces the experimental values of $S_{R,i}$ up to $N_i = 6$ and the reduction of $S_{R,i}$ with N_i can be attributed to a decrease of the quantum yield of e-h pairs as described by the Saha model. For higher values of N_i the experimental values of $S_{R,i}$ are lower than those from the fit. This can be due to a decrease of the charge mobility, since at higher density mutual scattering of charges in a rod of finite length will reduce their mobility. Figure 3.3D shows the quantum yield of e-h pairs and of excitons. It is seen that photoexcitation leads mainly to formation of excitons with a quantum yield exceeding 0.85 even at low N_i .

The real mobility of charges obtained above can be limited by scattering at the ends of nanorod. The ac charge carrier mobility $\mu_{ac}(f)$ at THz frequency f on a nanorod of finite length L can be related to the dc mobility μ_{dc} of a charge on an infinitely long nanowire according to²⁵⁻²⁷

$$\mu_{ac}(f) = 8\mu_{dc} \sum_{p=0}^{\infty} \frac{C_p^{-2}}{1 - \frac{ik_B T \mu_{dc} C_p^2}{eL^2 2\pi f}}, \quad (3.7)$$

with e the elementary charge and $C_p = 2\pi\left(p + \frac{1}{2}\right)$. Equation (3.7) yields for the real and imaginary components:

$$\mu_{ac}^R(f) = 8\mu_{dc} \sum_{p=0}^{\infty} \frac{C_p^{-2}}{1 + \left(\frac{k_B T \mu_{dc}}{e L^2 2\pi f}\right)^2 C_p^4}, \quad (3.8)$$

$$\mu_{ac}^I(f) = 8\mu_{dc} \sum_{p=0}^{\infty} \frac{C_p^{-2} \frac{k_B T \mu_{dc}}{e L^2 2\pi f}}{1 + \left(\frac{k_B T \mu_{dc}}{e L^2 2\pi f}\right)^2 C_p^4}. \quad (3.9)$$

Figure 3.4A shows the real and imaginary part ac mobility for $f = 0.8$ THz (the center frequency at which the experimental data in Figures 3.3 and 3.4 were obtained) calculated from equations 3.8 and 3.9 for a nanorod length $L = 51$ nm as a function of μ_{dc} . The experimental ac mobility is reproduced for $\mu_{dc} = 115 \text{ cm}^2\text{V}^{-1}\text{s}^{-1}$ and $\mu_{dc} = 2265 \text{ cm}^2\text{V}^{-1}\text{s}^{-1}$. The correct value can be determined by also considering the initial imaginary THz conductivity data in Figure 3.4C, which correspond to

$S_{I,i} = \phi_i \mu_i + [1 - \phi_i] \frac{\alpha \omega}{e}$ with μ_i the sum of the imaginary electron and hole mobility, α the polarizability of an exciton and ω the radian frequency of the THz field. Fitting $S_{I,i}$ with the quantum yield from the Saha model and $\mu_i = 25 \text{ cm}^2\text{V}^{-1}\text{s}^{-1}$ (which corresponds to $115 \text{ cm}^2\text{V}^{-1}\text{s}^{-1}$) yields the drawn curve in Figure 3.4B with $\alpha = (0.9 \pm 0.1) \times 10^{-35} \text{ Cm}^2\text{V}^{-1}$. The fit reproduces the experimental data with the exception of high densities. By contrast, taking $\mu_{dc} = 2265 \text{ cm}^2\text{V}^{-1}\text{s}^{-1}$ and the corresponding $\mu_i = 404 \text{ cm}^2\text{V}^{-1}\text{s}^{-1}$ fails to reproduce the measured data (See Figure B5). Therefore, we conclude that $\mu_{dc} = 115 \text{ cm}^2\text{V}^{-1}\text{s}^{-1}$, which is close to the measured real THz mobility. Hence, the effect of scattering of charges at the ends of a nanorod is very small when probed at a frequency near 0.8 THz. In the analysis described above it was assumed that either the electron or the hole is mobile, which gives a lower limit to the exciton polarizability. Since the effective masses of electrons and holes are almost equal (see SI Section 4), it is reasonable to assume that electrons and holes have the same mobility ($45 \text{ cm}^2\text{V}^{-1}\text{s}^{-1}$). In that case we obtain $\mu_i = 12 \text{ cm}^2\text{V}^{-1}\text{s}^{-1}$.

s^{-1} and an upper limit to the exciton polarizability equal to $\alpha = 1.1 \times 10^{-35} \text{ Cm}^2\text{V}^{-1}$

¹. The exciton polarizability can be estimated theoretically using $\alpha_{\text{theory}} = \frac{2e^2 a_B^2}{E_1 - E_0}$,²⁸

where the summation over all higher exciton states is reduced to the first only, the transition dipole moment is taken equal to the calculated exciton Bohr radius $a_B = 2.2 \text{ nm}$ and $E_1 - E_0$ is taken equal to the exciton binding energy for PbSe nanowires with 4 nm diameter, as mentioned above.⁹ This gives $\alpha_{\text{theory}} = 10^{-35} \text{ Cm}^2\text{V}^{-1}$, which is in close agreement with the experimental result of $(0.8-1.1) \times 10^{-35} \text{ Cm}^2\text{V}^{-1}$.

As discussed above, photoexcitation of the PbSe nanorods leads mainly to excitons (see Figure 3.3D). Hence, the optical bleach at the band gap (ΔOD in Figures 3.2A, B2) can to a good approximation be taken as a measure of the average number of excitons per nanorod, which we denote as N . As discussed above, for low excitation densities $N_i = N_0 \leq 6$ the maximum bleach at short time directly reflects the average number of photoexcitations per nanorod. For these densities, the transients in Figure 3.4C and 3.4D were obtained by scaling the measured bleach (ΔOD) such that they have magnitude $j_0 \sigma_{\text{abs}}$ at the maximum. At higher densities this procedure is not valid, due to Auger recombination of hot charge carriers prior to having relaxed to the band gap. This causes the maximum bleach on short time to be smaller than $j_0 \sigma_{\text{abs}}$, see Figure 3.2D. Fortunately, at these higher densities all nanorods are photoexcited and the bleach can be scaled such that $N=1$ at long times.

Taking into account Auger recombination of excitons, the time-dependent average number of excitons per nanorod is given by²⁹

$$N(t) = \sum_{i=1}^{\infty} A_i \exp \left[-i \left(\frac{1}{2} (i-1) k_2^A \right) t \right], \quad (3.10)$$

with k_2^A the Auger recombination rate for two excitons in a nanorod. The coefficients in equation (3.10) are equal to²⁹

$$A_i = N^i e^{-N} (2i-1) \sum_{j=0}^{\infty} \frac{N^j \Gamma(i+j)}{j! \Gamma(2i+j)}. \quad (3.11)$$

By taking the initial value of the number of excitons in a nanorod equal to $N = j_o \sigma_{abs}$ and treating as an adjustable parameter, we could reproduce the measured optical bleach transients until $N = 6$ with a value of $k_2^A = 3 \times 10^9 \text{ s}^{-1}$ (see Figure 3.4C). For $N > 6$ the fitted transients exceed the experimental results shorter times. This is attributed to Auger recombination of hot e-h pairs before they reach the band edge, so that the maximum in the measured transient does not represent the initial number of photoexcitations. Hence, transients at higher density such that $N > 6$, we take N_i as the initial value for N in equation (3.10), yielding the curves shown in Figure 3.4D. The fitted curves in Figure 3.4D obtained with $k_2^A = 3 \times 10^9 \text{ s}^{-1}$ agree with the experimental data. From this we infer that Auger recombination of hot e-h pairs reduces the initial average number of excitons at the band gap in a nanorod, while approximately maintaining a Poisson distribution, which is the initial condition for equation (3.10). Results for other densities are shown in Figure B6. The biexciton lifetime of $1/k_2^A = 330 \text{ ps}$ obtained as described above, is longer than the value of 210 ps reported for shorter nanorods of average length 25 nm and 4 nm diameter.¹⁰ This can be understood, since in longer nanorods the spatial overlap between two excitons will be smaller than in shorter nanorods, which enhances the lifetime before Auger recombination.

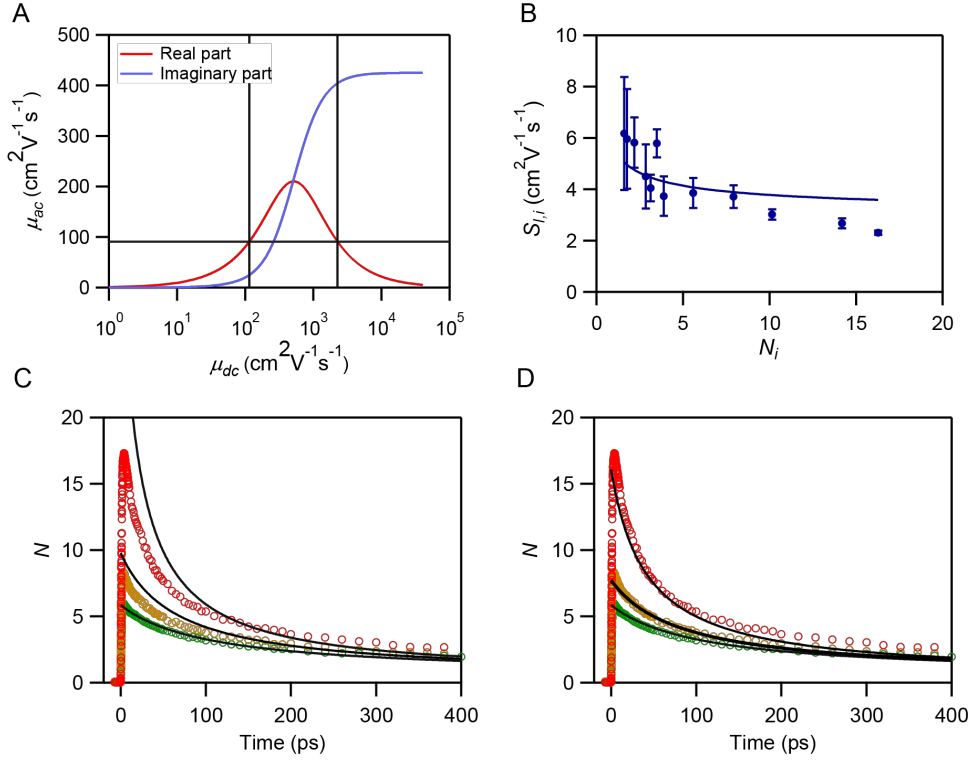


Figure 3.4. Theoretical modelling. (A) Calculated real and imaginary components of μ_{ac} as a function of μ_{dc} at frequency 0.8 THz for a nanorod of length 51 nm. (B) Experimental $S_{L,i}$ values (markers), obtained by averaging over 5-10 ps after the laser pump pulse and fit with $\mu_l = 25 \text{ cm}^2 \text{V}^{-1} \text{s}^{-1}$ and α as adjustable parameter (drawn curve). (C) Experimental (markers) and theoretical (drawn black curves) decay of N as a function of time with the initial condition $N = j_0 \sigma_{abs}$ in equation (3.10). (D) Decay with $N = N_i$ as the initial condition in equation (3.10), for $N \geq 6$.

3.4 Conclusions

Photoexcitation of the PbSe nanorods studied leads predominantly to excitons rather than free e-h pairs. The exciton polarizability of $10^{-35} \text{ Cm}^2 \text{V}^{-1}$ inferred from the experiments agrees with that from a theoretical estimate. The sum of the mobility of an electron and hole moving in phase with the THz electric field is as high as $91 \pm 13 \text{ cm}^2 \text{V}^{-1} \text{s}^{-1}$. For higher photoexcitation density the photoconductivity is strongly affected by mutual interactions between charges and excitons, leading to a lower charge mobility. The high quantum yield of excitons makes PbSe nanorods of interest as a gain material in near infra-red LEDs or lasers. For use of PbSe nanorods in solar

cells, hetero-junctions must be realized so that excitons can dissociate into free charges.

References

1. Cunningham, P. D.; Boercker, J. E.; Foos, E. E.; Lumb, M. P.; Smith, A. R.; Tischler, J. G.; Melinger, J. S., Enhanced Multiple Exciton Generation in Quasi-One-Dimensional Semiconductors. *Nano Lett.* **2011**, *11* (8), 3476-3481.
2. Davis, N. J. L. K.; Böhm, M. L.; Tabachnyk, M.; Wisnivesky-Rocca-Rivarola, F.; Jellicoe, T. C.; Ducati, C.; Ehrler, B.; Greenham, N. C., Multiple-exciton generation in lead selenide nanorod solar cells with external quantum efficiencies exceeding 120%. *Nat. Commun.* **2015**, *6*, 8259.
3. Talebi, H.; Dolatyari, M.; Rostami, G.; Manzuri, A.; Mahmudi, M.; Rostami, A., Fabrication of fast mid-infrared range photodetector based on hybrid graphene–PbSe nanorods. *Appl. Opt.* **2015**, *54* (20), 6386-6390.
4. Padilha, L. A.; Stewart, J. T.; Sandberg, R. L.; Bae, W. K.; Koh, W. K.; Pietryga, J. M.; Klimov, V. I., Carrier multiplication in semiconductor nanocrystals: influence of size, shape, and composition. *Acc. Chem. Res.* **2013**, *46* (6), 1261–1269.
5. Kaindl, R. A.; Hägele, D.; Carnahan, M. A.; Chemla, D. S., Transient terahertz spectroscopy of excitons and unbound carriers in quasi-two-dimensional electron-hole gases. *Physical Review B* **2009**, *79* (4), 045320.
6. Hangleiter, A.; Jin, Z.; Gerhard, M.; Kalincev, D.; Langer, T.; Bremers, H.; Rossow, U.; Koch, M.; Bonn, M.; Turchinovich, D., Efficient formation of excitons in a dense electron-hole plasma at room temperature. *Phys. Rev. B* **2015**, *92* (24), 241305.
7. Lauth, J.; Kulkarni, A.; Spoor, F. C. M.; Renaud, N.; Grozema, F. C.; Houtepen, A. J.; Schins, J. M.; Kinge, S.; Siebbeles, L. D. A., Photogeneration and Mobility of Charge Carriers in Atomically Thin Colloidal InSe Nanosheets Probed by Ultrafast Terahertz Spectroscopy. *J. Phys. Chem. Lett.* **2016**, *7* (20), 4191-4196.
8. Suzuki, T.; Shimano, R., Exciton Mott Transition in Si Revealed by Terahertz Spectroscopy. *Phys. Rev. Lett.* **2012**, *109* (4), 046402.
9. Bartnik, A. C.; Efros, A. L.; Koh, W. K.; Murray, C. B.; Wise, F. W., Electronic states and optical properties of PbSe nanorods and nanowires. *Physical Review B* **2010**, *82* (19), 195313.
10. Yang, J.; Hyun, B.-R.; Basile, A. J.; Wise, F. W., Exciton Relaxation in PbSe Nanorods. *ACS Nano* **2012**, *6* (9), 8120-8127.
11. Aerts, M.; Spoor, F. C. M.; Grozema, F. C.; Houtepen, A. J.; Schins, J. M.; Siebbeles, L. D. A., Cooling and Auger Recombination of Charges in PbSe Nanorods: Crossover from Cubic to Bimolecular Decay. *Nano Lett.* **2013**, *13* (9), 4380-4386.
12. Placencia, D.; Boercker, J. E.; Foos, E. E.; Tischler, J. G., Synthesis and Optical Properties of PbSe Nanorods with Controlled Diameter and Length. *J. Phys. Chem. Lett.* **2015**, *6* (17), 3360-3364.

13. Spoor, F. C. M.; Kunneman, L. T.; Evers, W. H.; Renaud, N.; Grozema, F. C.; Houtepen, A. J.; Siebbeles, L. D. A., Hole Cooling Is Much Faster than Electron Cooling in PbSe Quantum Dots. *ACS Nano* **2016**, *10* (1), 695-703.
14. Evers, W. H.; Schins, J. M.; Aerts, M.; Kulkarni, A.; Capiod, P.; Berthe, M.; Grandidier, B.; Delerue, C.; van der Zant, H. S. J.; van Overbeek, C.; Peters, J. L.; Vanmaekelbergh, D.; Siebbeles, L. D. A., High charge mobility in two-dimensional percolative networks of PbSe quantum dots connected by atomic bonds. *Nature Communications* **2015**, *6*, 8195.
15. Kulkarni, A.; Evers, W. H.; Tomić, S.; Beard, M. C.; Vanmaekelbergh, D.; Siebbeles, L. D. A., Efficient Steplike Carrier Multiplication in Percolative Networks of Epitaxially Connected PbSe Nanocrystals. *ACS Nano* **2018**, *12* (1), 378-384.
16. Ulbricht, R.; Hendry, E.; Shan, J.; Heinz, T. F.; Bonn, M., Carrier dynamics in semiconductors studied with time-resolved terahertz spectroscopy. *Reviews of Modern Physics* **2011**, *83* (2), 543-586.
17. Joyce, H. J.; Boland, J. L.; Davies, C. L.; Baig, S. A.; Johnston, M. B., A review of the electrical properties of semiconductor nanowires: insights gained from terahertz conductivity spectroscopy. *Semiconductor Science and Technology* **2016**, *31* (10), 103003.
18. Schaller, R. D.; Klimov, V. I., High Efficiency Carrier Multiplication in PbSe Nanocrystals: Implications for Solar Energy Conversion. *Phys. Rev. Lett.* **2004**, *92* (18), 186601.
19. Cunningham, P. D.; Boercker, J. E.; Placencia, D.; Tischler, J. G., Anisotropic Absorption in PbSe Nanorods. *ACS Nano* **2014**, *8* (1), 581-590.
20. Shah, J., IV.1 - Ultrafast Luminescence Studies of Carrier Relaxation and Tunneling in Semiconductor Nanostructures. In *Hot Carriers in Semiconductor Nanostructures*, Shah, J., Ed. Academic Press: San Diego, 1992; pp 279-312.
21. Trinh, M. T.; Houtepen, A. J.; Schins, J. M.; Hanrath, T.; Piris, J.; Knulst, W.; Goossens, A. P. L. M.; Siebbeles, L. D. A., In Spite of Recent Doubts Carrier Multiplication Does Occur in PbSe Nanocrystals. *Nano Lett.* **2008**, *8* (6), 1713-1718.
22. Ellingson, R. J.; Beard, M. C.; Johnson, J. C.; Yu, P.; Micic, O. I.; Nozik, A. J.; Shabaev, A.; Efros, A. L., Highly Efficient Multiple Exciton Generation in Colloidal PbSe and PbS Quantum Dots. *Nano Letters* **2005**, *5* (5), 865-871.
23. Lloyd-Hughes, J.; Jeon, T.-I., A Review of the Terahertz Conductivity of Bulk and Nano-Materials. *Journal of Infrared, Millimeter, and Terahertz Waves* **2012**, *33* (9), 871-925.
24. Ambigapathy, R.; Bar-Joseph, I.; Oberli, D. Y.; Haacke, S.; Brasil, M. J.; Reinhardt, F.; Kapon, E.; Deveaud, B., Coulomb Correlation and Band Gap Renormalization at High Carrier Densities in Quantum Wires. *Physical Review Letters* **1997**, *78* (18), 3579-3582.

25. Grozema, F. C.; Siebbeles, L. D. A., Mechanism of charge transport in self-organizing organic materials. *Int. Rev. Phys. Chem.* **2008**, *27* (1), 87-138.
26. Bhaskar, P.; Achtstein, A. W.; Diedenhofen, S. L.; Siebbeles, L. D. A., Mobility and Decay Dynamics of Charge Carriers in One-Dimensional Selenium van der Waals Solid. *J. Phys. Chem. C* **2017**, *121* (34), 18917-18921.
27. Prins, P.; Grozema, F. C.; Schins, J. M.; Patil, S.; Scherf, U.; Siebbeles, L. D. A., High Intrachain Hole Mobility on Molecular Wires of Ladder-Type Poly(\$p\$-Phenylenes). *Phys. Rev. Lett.* **2006**, *96* (14), 146601.
28. Atkins, P. W.; Friedman, R. S., *Molecular Quantum Mechanics*. OUP Oxford: 2011.
29. Barzykin, A. V.; Tachiya, M., Stochastic models of charge carrier dynamics in semiconducting nanosystems. *J. Phys.: Condens. Matter* **2007**, *19* (6), 065105.

Appendix B

1. Spectral feature at various N_i .

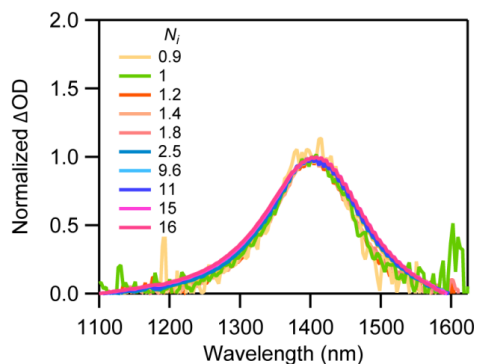


Figure B1. Spectral bleach at various N_i obtained from averaging the bleach spectrum over 5-10 ps after photoexcitation.

2. TA spectroscopy data.

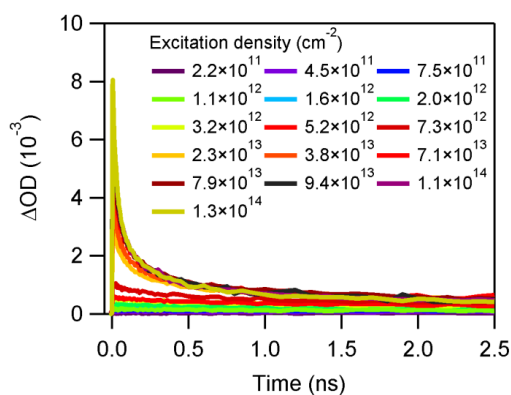


Figure B2. TA spectroscopy results. ΔOD obtained by averaging the measured bleach in the range 1100-1600 nm near the band gap after photoexcitation at 800 nm for excitation densities as indicated.

2. THz photoconductivity data.

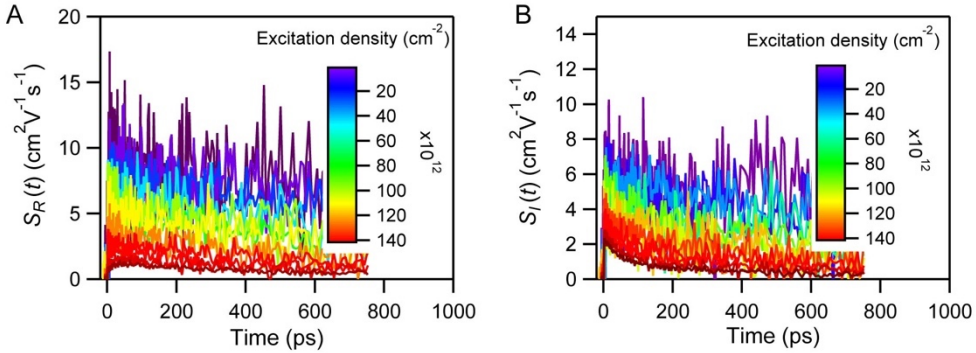


Figure B3. THz photoconductivity results. (A) Quantum yield weighted real mobility of free charges obtained for photoexcitation densities as indicated. (B) Quantum yield weighted imaginary mobility of free charges and the polarizability of exciton obtained for photoexcitation densities as indicated.

4. Determination of the effective masses of electrons and holes.

The effective masses of electrons m_e^* and holes m_h^* for a nanowire of diameter 4 nm was determined by fitting the expression $E(k_z) = E_0 + \frac{\hbar^2 k_z^2}{2m_{e(h)}^*}$ to the conduction and valence band dispersion taken from published data.¹

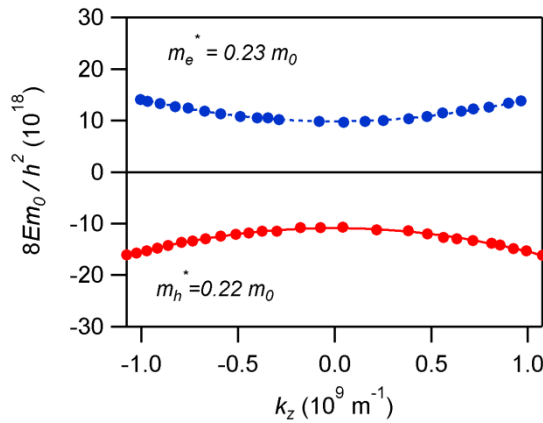


Figure B4. Fit to energy dispersion for the valence and conduction band of PbSe nanowires of diameter 4 nm obtained from ref. 1.

5. Fit to the imaginary component of the THz signal.

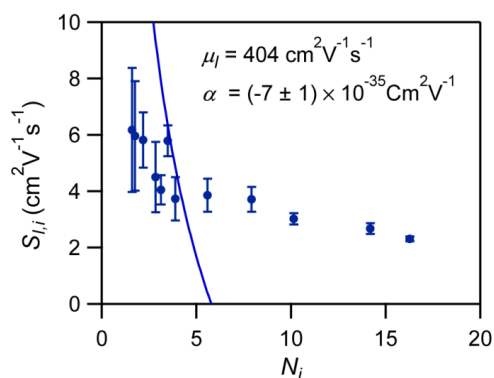


Figure B5. Fit to the initial imaginary component of the quantum yield weighted with imaginary charge mobility $\mu_l = 404 \text{ cm}^2 \text{V}^{-1} \text{s}^{-1}$ and α as adjustable parameter.

6. Simulated decay of optical bleach.

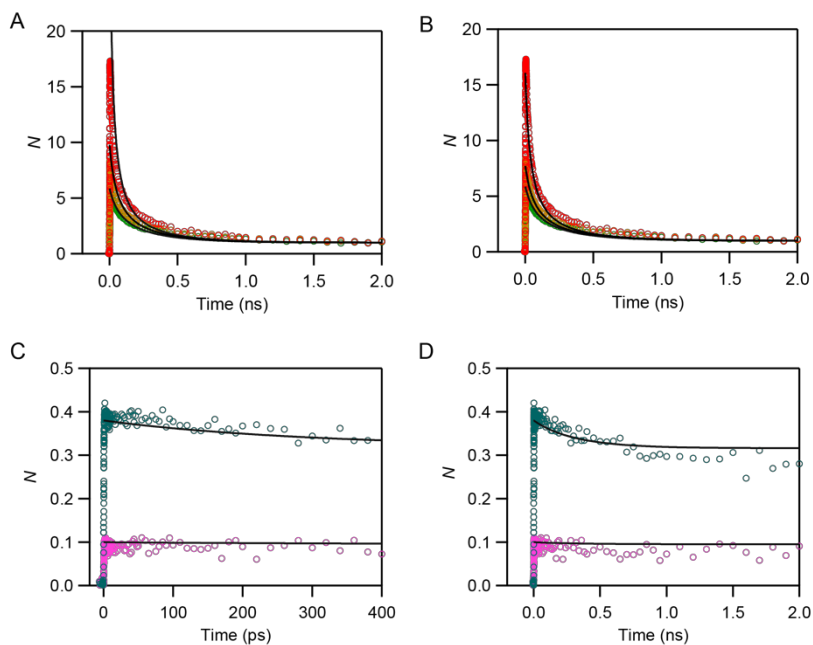


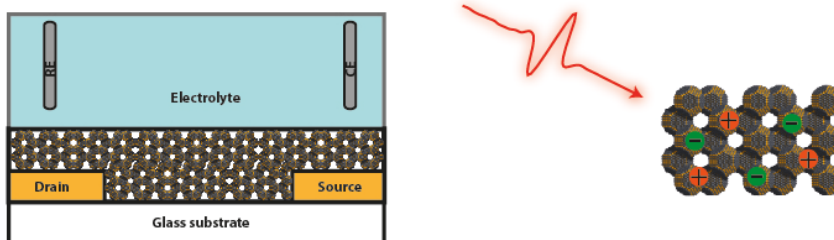
Figure B6. Simulated decay curves. (A) Experimental (markers) and theoretical (drawn black curves) decay of N as a function of time with the initial condition $N = j_0 \sigma_{abs}$ in equation (3.10). (B) Decay with $N = N_i$ as the initial condition in equation (3.10), for $N \geq 6$. (C) Experimental decay of for $N < 1$ until 400 ps, (D) until 2 ns.

Reference

1. Bartnik, A. C.; Efros, A. L.; Koh, W. K.; Murray, C. B.; Wise, F. W. Electronic states and optical properties of PbSe nanorods and nanowires. *Phys. Rev. B* **2010**, 82, 195313.

Chapter 4

Room-Temperature Electron Transport in PbSe Honeycomb Superstructures Studied in a Transistor Configuration and by Terahertz Spectroscopy



Based on:

Room-Temperature Electron Transport in PbSe Honeycomb Superstructures Studied in a Transistor Configuration and by Terahertz Spectroscopy.

Maryam Alimoradi Jazi, Aditya Kulkarni, Sophia Buhbut Sinai, Joep L. Peters, Eva Geschiere, Michele Failla, Christophe Delerue, Arjan J. Houtepen, Laurens D. A. Siebbeles, and Daniel Vanmaekelbergh.

The Journal Physical Chemistry C, in press.

4.1 Introduction

Quantum dot solids composed of colloidal nanocrystals (NCs) have attracted strong interest since about two decades. Such solids show opto-electronic properties that reflect the properties of the individual nanocrystalline quantum dots together with the dipolar and electronic coupling between them. Since there are many types of NCs that can be incorporated in a solid and the quantum coupling between the NCs can be varied by control over the NC surface chemistry, NC solids form a material platform with considerable tunability and versatility. This platform is of great interest to address basic scientific questions in quantum transport and shows promises for future opto-electronics.¹⁻¹²

In this field, solids that are formed by NC assembly followed by oriented attachment of the NCs constitute a special class, since oriented attachment results in atomically coherent systems and strong quantum coupling. Over the years, atomically coherent one-dimensional rods,^{13, 14} two-dimensional quantum wells¹⁵, and nearly three dimensional¹⁶ nanostructured but atomically coherent systems have been reported. Since, due to the NC/NC epitaxy, the quantum coupling is strong, the energy level and band structure of these systems is determined by their overall dimensions. A remarkable class is 2-D superstructures that show a silicene-type honeycomb structure: these systems retain the semiconductor band gap but the highest valence and lowest conduction bands show a linear dispersion near the K-points of the Brillouin zone. This would mean that at sufficiently low temperature and with precise control of the Fermi level at around the K-points, massless electrons (holes) may dominate the transport properties, as in graphene.¹⁷

However, before this type of physics can be explored, several challenges must be addressed: One must be able to prepare sufficiently large domains of honeycomb superlattices to incorporate them in an electrical device with suitable contacts and to change the Fermi-level in a controlled way by gating. Control over the band occupation also means that a decent knowledge on the presence of in-gap states is a prerequisite. Second, it will be required to cool down the entire transistor system (at a given position of the Fermi-level), without mechanical or electrical breakage.

Here, we start this endeavor by a room-temperature study of the band occupation and electron transport in silicene-type honeycomb structures prepared from PbSe NCs. We used a transistor device allowing to measure the electronic properties under electronic equilibrium, and terahertz (THz) spectroscopy to measure the transient behavior of photo-generated electrons and holes. This study is motivated by the fact

that we recently were able to reproducibly fabricate extended ($> 100 \mu\text{m}$) domains of PbSe honeycomb structures by nanocrystal assembly and oriented attachment.¹⁸ We show that we can incorporate wet-chemically prepared superstructures as individual silicene sheets in an electrolyte gated device. We can change the Fermi level in a controlled way and occupy the lowest conduction band with up to 4 electrons, without interference of mid-gap electron traps. By moving the Fermi level to lower energies towards the valence band, holes are injected. They might either occupy the valence band or mainly trap states in the gap. The electron mobility measured in the transistor type device (about $1.5 \pm 0.5 \text{ cm}^2\text{V}^{-1}\text{s}^{-1}$) compares well with that obtained by THz spectroscopy. The frequency-dependent THz results indicate that the room temperature electron mobility is not limited by electron scattering on lattice phonons, but mostly by lattice imperfections.

4.2 Materials and methods

PbSe NCs synthesis. PbSe QDs were synthesized based on the methodology of Steckel et al. method.¹⁸ For the lead precursor, a mixture of 4.77 g lead acetate, 10.35 g oleic acid and 39.75 g 1-octadecene was heated at 120°C under vacuum for 5 hours. For the selenium precursor, a mixture of 3.52 g selenium powder, 46.59 mL trioctylphosphine and 0.41 mL diphenylphosphine were prepared by dissolving selenium. Subsequently, 10.25 mL of the lead containing solution was heated upto 180°C and 7.5 mL of the selenium precursor was injected. The mixture was kept at 150°C for 70 second and the NC growth was quenched with 30 mL of a methanol/butanol mixture (1:2). The NC product solution was centrifuged and the NCs were dissolved in toluene. This concentrated suspension of PbSe NCs was washed twice more with methanol and the NCs were dissolved in toluene.

The formation of honeycomb superstructure by means of oriented attachment. Honeycomb superlattices were obtained by the NCs assembly at the toluene-nitrogen interface followed by oriented attachment. We followed an ultra-slow procedure that has been developed recently in our group (Figure C1). A small petri dish was filled with ethylene glycol as a liquid substrate. This dish was placed in a bigger petri dish that also contained toluene. A certain volume of PbSe NC dispersion in toluene was drop casted on top of ethylene glycol. A beaker was placed on top of the petri dishes to slow down the toluene evaporation. The evaporation of the toluene solvent and the superlattice formation was really slow and took around 16 hours. The honeycomb monolayer was transferred onto a TEM grid for structural characterization, quartz substrates for THz measurement and a device with microstructured gold electrodes,

i.e. source and drain, separated by a gap for electrolyte gating and transport measurements (details in SI section 3). The formation of PbSe honeycomb superlattices and their transport to a TEM grid, the quartz substrate and a transport device were performed in a glove box.

Surface treatment by PbCl_2 . In an attempt to passivate the surface traps, the surface of the honeycomb superlattices was treated by PbCl_2 . For this purpose, a saturated dilution of PbCl_2 in methanol was prepared. The substrates with the superlattices were immersed shortly into the PbCl_2 dilution and then into methanol, to remove the residuals.

Electron injection and transport measurement in an electrolyte gated transistor. Electrochemical gating is a well-established method used to investigate the transport properties of 2-D superlattices. The device used for this measurement consists of interdigitated source and drain electrodes, on top of a SiO_2 substrate (details in SI). In this experiment we used acetonitrile containing a Li^+ salt as an electrolyte. An Ag wire and a Pt sheet were inserted into the electrolyte for reference and counter electrodes, respectively. The Fermi level of the superlattices moved towards the conduction band (valence band) by applying negative (positive) potential with respect to the reference electrode by using a potentiostat. To investigate the charge injection into the honeycomb superlattice, differential capacitance measurements were performed. By applying the potential in small steps of 55 mV, the current in an interval time was measured. The integration of the current gave us the total amount of charge injected to the structure. For measurement of the sample conductance at a given potential, a small potential was applied between source and drain electrodes and the source-drain current was measured. As soon as the Fermi level was in the conduction band, the source-drain resistance was Ohmic. The conductivity was obtained from the measured conductance the geometry of the electrodes. Eventually, the electron mobility was obtained from the conductivity and the electron density (details in SI).

Terahertz conductivity measurements. The honeycomb superlattice was photoexcited by optical pulses with photon energy 1.55 eV. The photoconductivity was probed by single-cycle THz pulses analogous to our previous work.^{19, 20} To prevent air exposure, we placed the sample in an airtight sample holder during the photoconductivity measurements. According to the thin film approximation the complex conductivity ($\Delta\sigma(\omega, t)$) of charges at a pump-probe delay time t averaged over the sample thickness (L) is related to the differential THz signal ($\Delta E(\omega, t)$) via

21, 22

$$\frac{\Delta E(\omega, t)}{E_0(\omega)} = \frac{L\Delta\sigma(\omega, t)}{(1+n_s)c\epsilon_0}. \quad (4.1)$$

The complex conductivity of charges is related to the quantum yield weighted complex mobility ($\phi_e(t)\mu_e + \phi_h(t)\mu_h$) via ^{37,38}

$$\phi_e\mu_e + \phi_h\mu_h = \frac{L\Delta\sigma(\omega, t)}{eN_a}, \quad (4.2)$$

with N_a the number of absorbed photons per unit area (excitation density). Substituting equation (2) into (1) and rearranging yields

$$S(t) = \phi_e\mu_e + \phi_h\mu_h = \frac{L\Delta\sigma(\omega, t)}{eN_a}, \quad (4.3)$$

which is independent of the sample thickness L .

4.3 Results and discussion.

Formation of 2-D honeycomb superlattices of PbSe. We prepared 2-D honeycomb superlattices from PbSe NCs (with the size of 6.15 ± 0.4 nm) dispersed in toluene by self-assembly at the toluene-nitrogen interface and oriented attachment as described in the methods section and appendix C1.²³ An atomically coherent silicene-type honeycomb structure is formed by epitaxial attachment of the PbSe NCs via three of their 6 facets. A part of such a honeycomb structure is shown in Figure 4.1A. The Fourier transform of the image in the inset shows that the honeycomb periodicity holds for the entire image and is thus long ranged. We remark here that, due to the epitaxial connection, the quantum coupling between the NCs is strong. Atomic tight binding (TB) calculations have shown that this coupling results in mini-band formation with a band width in 0.1 eV range.²⁴ This means that, for ideal honeycomb structures, high mobility values only limited by phonon scattering are expected. On the other hand, disorder could also limit carrier transport. Several types of disorder have been observed and detailed in a recent work²³: Non-perfect epitaxial connections between the NCs is probably the most important origin of crystallographic disorder. In the experiments described here, the PbSe superstructures also showed slightly more disordered regions between the

honeycomb domains (Figure 4.1B). Disorder due to the nanocrystal misalignment in the lattice is obvious from Figure 4.1c.

Light absorption by a PbSe honeycomb monolayer. The optical absorption spectrum of the NCs dispersed in tetrachloroethylene exhibits a peak at 0.7 eV related to the first exciton transition (Figure 4.1D). For a single PbSe honeycomb layer, the first feature is broadened such that it almost looks as a step, and it is also red shifted. Similar features have been observed for the square superlattices.²⁵ The broadening is due to quantum coupling between the PbSe NCs, ultimately resulting in band formation (see also below).^{3, 25, 26} The red shift has been attributed to the effect of the dielectric environment.^{3, 25} The band structure obtained from a TB calculation is presented in Figure C2 without inclusion of many-body electron-hole interaction effects, which are probably weak, due to the large dielectric constant of PbSe. The calculated band structure yields an effective mass of $0.21 m_0$ for electrons (m_0 the free electron mass). We should remark here that models for 2-D quantum wells predict a value of the absorbance of 2.3 % (related to the fine structure constant) for a single quantum well. The value that we measure is 1.5 %, about half the predicted value for a single free standing layer. A similar reduction of absorption of a 2-D monolayer has been observed previously and was attributed to the presence of the quartz substrate.²⁷

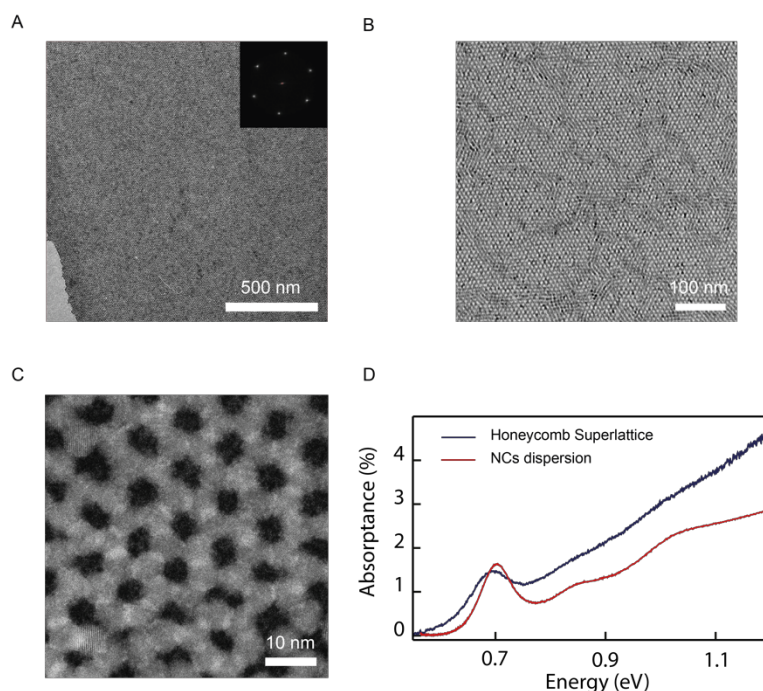


Figure 4.1. Structural properties of the PbSe honeycomb superlattice studied here: (A) TEM overview of a PbSe superlattice with honeycomb nanogeometry; the inset is the Fourier transform of the image showing that the honeycomb periodicity is long ranged and holds for the entire image. (B) TEM image of a superlattice with smaller honeycomb domains connected by slightly disordered grain boundaries. (C) High resolution HAADF-STEM image showing several types of NC misalignment in the honeycomb structure. (D) Absorption spectrum of a single-layer honeycomb superlattice deposited on a quartz substrate compared to that of dispersed NCs. The first excitonic absorption feature of the PbSe superlattice shows a red shift and broadening, compared to the NCs in dispersion. For the honeycomb superlattice monolayer on a quartz substrate, the absorption is 1.5 % at a photon energy of 0.7 eV. The absorption of NC dispersion is scaled down for comparison to the superlattice.

Transport measurements in an electrolyte-gated transistor. Single sheets of a honeycomb superlattice were incorporated into a transistor-type device by horizontal transfer of the structure from the ethylene glycol (EG) surface on which it was formed (see methods). The surface of the sample is treated by $PbCl_2$ which has been shown to passivate surface traps and improve electronic transport.²⁸ Using electrochemical gating; the number of conduction electrons in the honeycomb superlattice can be controlled. From the source-drain conductance and the electrode-gap geometry, the electron conductivity and, finally, the electron mobility can be obtained.²⁵

In order to investigate the occupation of the bands with electrons (holes), differential capacitance measurements were performed (see methods). Figure 4.2A shows the differential capacitance characterizing the injection of electrons and holes into the PbSe honeycomb superlattice treated with $PbCl_2$. It can be seen that electron injection sets on at -0.4 V (versus Ag, reference electrode) and increases gradually up to a sample potential of -1.2 V. The shapes of the forward and backward scans are similar but not entirely identical. It means that the charge injection is not entirely electrochemically reversible and some minor side reactions, such as the reduction of residual molecular oxygen, may be ongoing. At positive potentials, the differential capacitance rises, showing that positive charge carriers are injected into the PbSe superstructure.

The total amount of injected charge carriers and the number of carriers per NC site ($=1/2$ unit cell) in the forward scan is depicted in Figure 4.2B. The method to determine this number is outlined in appendix C Section 4. At the most negative potential (-1.2 V), we observed 4 electrons per NC site, meaning that the 8-fold degenerate S-type conduction band is, in principle, half occupied. We should mention here that the uncertainty in the occupation number is relatively large due to the uncertainty in the effective active area of the device (see details appendix C Section 4). An optical microscope image of the active channel of the device is presented in

Appendix C4 showing that basically the whole area of the channel is covered by the superlattice. Also note that at room temperature, electrons can be thermally excited from the S-type mini-band into the P-type mini-band. Strongly charged PbSe NCs have also been reported recently.²⁹⁻³³

At sample potentials more negative than -0.5 V, the source-drain transport current increased linearly with the source-drain bias (see Figure C6); the slope provides the conductance of the superlattice. From the conductance and the geometry of the interdigitated source-drain electrodes and gap, the electronic conductivity was calculated. We have plotted the conductivity of the sample as a function of the sample potential on a linear scale (Figure 4.2A) and a logarithmic scale (Figure 4.2D) for convenience. As can be observed in Figure 4.2C, the conductivity sets on at around -0.5 V and rises steeply with the electrochemical potential, up to 1100 S/m at the most negative potential. For positive electrochemical potentials the differential capacitance increases again, this is accompanied with a small increase of the source-drain conductance (Figure 4.2D). It appears that the conductivity at positive potential is much smaller than the electron conductivity. This indicates that the injected positive charges to the superlattice might either occupy the valence band, or could occupy localized in-gap states. In the logarithmic scale in Figure 4.2D, the conductivity shows a step-like peak (not clearly visible on a linear scale) at a potential of -0.4 V. However, the charge density at this potential has a very small value. Therefore, we cannot conclude whether this peak is real and related to the band occupation of the superlattice.

Results obtained with other samples, also a sample that is non-treated with $PbCl_2$, are provided in Appendix C section 6. Similar results are obtained for those samples; i.e. the onset of the conductivity close to the onset of electron injection, the number of electrons in the conduction band varying between 4 and 8 per nanocrystal site, and a smaller conductance at positive potentials at which holes either occupy the valence band or trap states.

The electron mobility of the sample of Figure 4.2 calculated from the electron density and conductivity reached a maximum value of $2.3 \text{ cm}^2\text{V}^{-1}\text{s}^{-1}$ at -1V. We performed differential capacitance and conductivity measurement on three other PbSe honeycomb devices. On average, we find an electron mobility of $1.5 \pm 0.5 \text{ cm}^2\text{V}^{-1}\text{s}^{-1}$ in the PbSe honeycomb superlattices in the potential window of $-1.05 < V < -0.75$. For the sample non-treated with $PbCl_2$ the mobility was found to have a lower value of $0.4 \text{ cm}^2\text{V}^{-1}\text{s}^{-1}$ (see Figure C7), which we attribute to the presence of trapping sites that have a negative effect on electron transport.

We further note that at the most negative potentials the conductivity is probably limited somewhat by the contact resistance between the honeycomb superlattice and the gold source and drain contacts. This may explain why the conductivity levels off and why the derived value of the mobility even decreases. Hence the values obtained here are a lower limit to the intrinsic dc mobility.

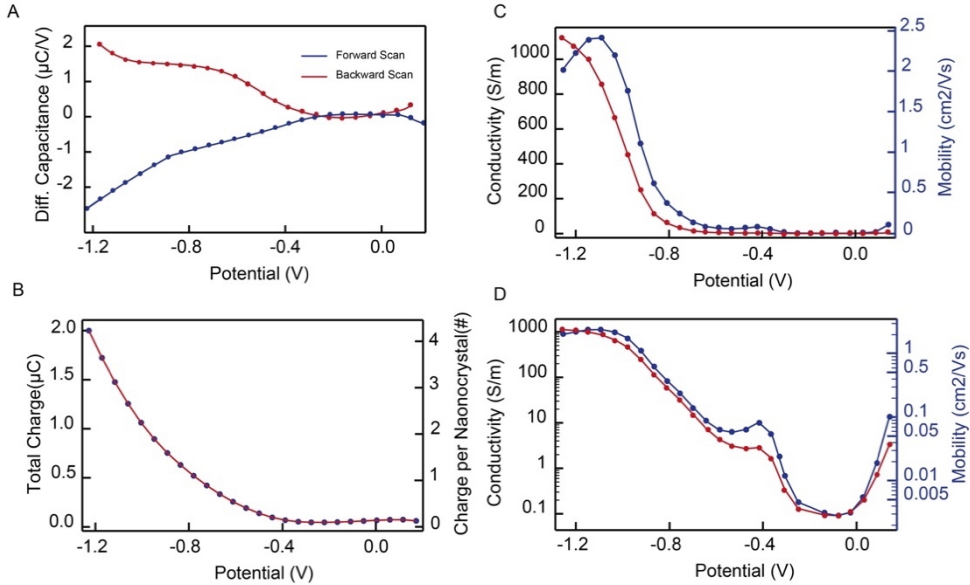


Figure 4.2. Electron injection and electron transport characteristics in a passivated PbSe honeycomb superstructure incorporated in an electrolyte gated transistor: (A) Differential capacitance of a passivated PbSe honeycomb superlattice measured in forward (from 0.2 to -1.2 V) and backward scan. (B) The total injected charge and the charge per NC site as measured in the forward scan. (C) The conductivity (blue) and the electron mobility (green) of the superlattice obtained from the source-drain conductance (See Figure C5), the geometry of the source-gap-drain fingers system and the charge density presented as a function of the electrochemical potential. (D) The conductivity (blue) and the electron mobility (green) of the superlattice in logarithmic scale.

Terahertz photoconductivity spectroscopy: The THz photoconductivity was studied by photoexciting PbSe honeycomb superstructures with 50 fs laser pulses at a photon energy of 1.55 eV. The experimental procedure involves detection of charges and excitons with a single-cycle THz field and is identical to that described previously.^{19, 20} In general, photoexcitation of a semiconductor leads to formation of free mobile charges that can coexist with bound e-h pairs in the form of neutral excitons.³⁴⁻³⁶ Free mobile charges and neutral excitons both contribute to the THz conductivity to an extent that is different for the real and imaginary parts.^{37, 38} At

higher photoexcitation density recombination of free charges into excitons is more likely and consequently the quantum yield of charges decreases. If excitons co-exist with free charges in the honeycomb superlattice the relative magnitude of the real and imaginary THz conductivity should depend on the initial photoexcitation density and the decay kinetics of the real and imaginary parts should be different. Since the normalized decay of the real and imaginary parts are identical (see Figure C9) it can be inferred that the contribution of excitons is negligible and the initial quantum yield of charges can be taken equal to 1. The real part (positive sign) of the THz conductivity is due to the in-phase charge velocity in the probing THz field, and the imaginary part (negative sign) is due to the out-of-phase charge velocity.^{21, 22, 39} The electrolyte gated transistor measurements have shown that holes might mostly occupy localized in-gap states. Therefore, the mobility of holes can be neglected and the THz conductivity can be ascribed to electrons only.

Figure 4.3 shows the THz conductivity for a PbSe honeycomb superstructure treated with PbCl₂ to passivate surface traps. The product of the time-dependent quantum yield of electrons and their mobility: defined $S(t) = \phi_e(t)\mu_e$ with the initial quantum yield $\phi_e(t = 0) = 1$, as discussed above is shown for an excitation density of $2.5 \times 10^{13} \text{ cm}^{-2}$, which corresponds to 10 electron-hole (e-h) pairs per nanocrystal (NC) (see methods). The signal $S(t)$ reaches a maximum value of $2.1 \pm 0.4 \text{ cm}^2\text{V}^{-1}\text{s}^{-1}$ at a pump-probe delay time of 1.5 ps, which reflects the pulse duration of the probing single-cycle THz field. This value of $S(t)$ is attributed to relaxed charge carriers at the band edge, since for a photoexcitation energy of 1.55 eV initially hot e-h pairs in PbSe NCs cool down to the band edge within a picosecond.^{40, 41} The electrons are seen to decay *via* trapping or recombination with a lifetime for half decay of ~ 10 ps. Similar results were obtained for lower ($0.8 \times 10^{13} \text{ cm}^{-2}$) and higher ($2.5 \times 10^{13} \text{ cm}^{-2}$) excitation densities (see Figure C8), which implies that higher-order recombination is not important for these densities.

A comparison of $S(t)$ for the PbSe superstructure passivated with PbCl₂ and a non-treated superstructure is shown in Figure C11 for similar excitation densities. It can be clearly seen that surface passivation with PbCl₂ enhances the mobility by a factor four, which is in the same direction to that obtained from the DC device measurements described above. The excitation density of $4.3 \times 10^{13} \text{ cm}^{-2}$ needed to observe the THz conductivity in the non-treated superstructure is higher than that used for the structure treated with PbCl₂. The higher density leads to a faster decay via recombination and consequently a smaller value of $S(t)$ even on short timescales.

To understand the charge transport mechanism, we plot in Figure 4.3B the frequency dependent electron mobility obtained by averaging $S(t)$ over a pump-probe delay time interval of 2-6 ps. The increase of the mobility in Figure 4.3B with frequency ω and the negative imaginary mobility disagree with the simple Drude model.³⁹ The THz mobility is described by the Drude-Smith model, yielding⁴²

$$\mu(\omega) = \frac{e\tau}{m^*(1-i\omega\tau)} \left(1 + \frac{c}{1-i\omega\tau} \right), \quad (4.4)$$

with e the elementary charge, τ the scattering time, m^* the effective mass, and $c = \langle \cos\theta \rangle$ a persistence of velocity parameter accounting for elastic backscattering with θ the scattering angle.

Solving for the real and imaginary parts of the Drude-Smith model yields:

$$\mu_{real}(\omega) = \frac{e\tau}{m^*(1+\omega^2\tau^2)} \left(1 + \frac{c(1-\omega^2\tau^2)}{1+\omega^2\tau^2} \right), \quad (4.5)$$

$$\mu_{imag}(\omega) = \frac{e\omega\tau^2}{m^*(1+\omega^2\tau^2)} \left(1 + \frac{2c}{1+\omega^2\tau^2} \right). \quad (4.6)$$

Taking the value of $m^* = 0.21 m_0$, from atomistic tight binding (See Figure 4.3), and fitting expressions (4.5) and (4.6) to the frequency dependent mobility in Figure 4.3B yields $\tau = 5.2 \pm 0.6$ fs and $c = -0.96 \pm 0.01$. At lower excitation densities we obtain similar values for τ and c (see Figure C9), which indicates that for the densities studied band filling does not affect the THz mobility. The backscattering parameter c close to -1 implies significant backscattering of the charges, which is typical for NC solids.^{43, 44} The DC mobility obtained from the Drude-Smith fit parameters is $1.7 \text{ cm}^2 \text{ V}^{-1} \text{ s}^{-1}$, which is close to the value of $1.5 \pm 0.5 \text{ cm}^2 \text{ V}^{-1} \text{ s}^{-1}$ obtained from the transistor measurements described above. Hence, although the coupling between the NCs in the honeycomb structure is considerable, the electron mobility is strongly limited by scattering at imperfections.

The Drude-Smith fit reproduces the measured real part of the THz mobility, while it does not agree very well with the measured imaginary part. Structural disorder may cause the site-energy of a charge to vary on going from one NC to another. The disorder in the site-energies is roughly equal to the width of the first optical absorption peak of the NCs, which is about 0.1 eV, see Figure 4.1D. Such

disorder is not included in the Drude-Smith model, which may cause the model to be inaccurate for the current material. A more detailed model of charge transport should include effects of disorder, however, that is beyond the scope of this study.

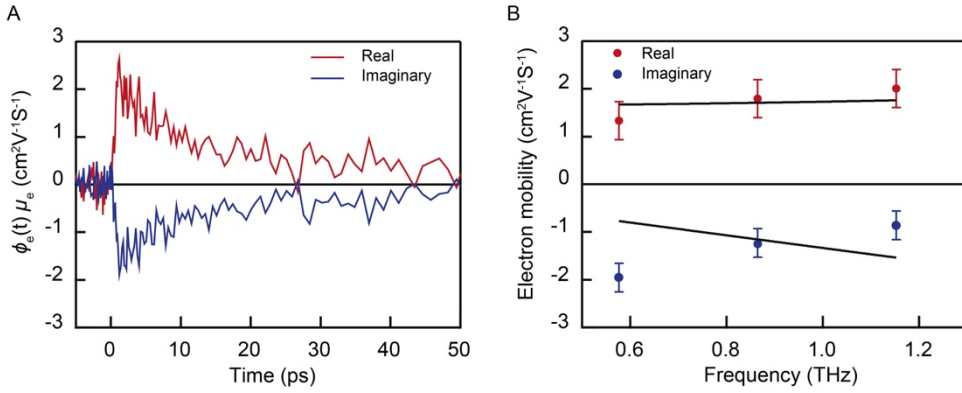


Figure 4.3. Terahertz photoconductivity obtained by photoexciting the PbSe honeycomb superstructure treated with PbCl_2 at photon energy of 1.55 eV. (A) Real (positive signal) and imaginary part (negative signal) of the quantum yield weighted mobility as a function of time obtained at excitation density $2.5 \times 10^{13} \text{ cm}^{-2}$, which corresponds to 10 electron-hole pairs per NC. (B) Experimental frequency dependent charge carrier mobility (markers) together with fit of the Drude-Smith model to the data.

Discussion: We have studied electron transport in single sheets of PbSe with a silicene-type honeycomb geometry. In an ideal case, these structures are atomically coherent: the $\langle 111 \rangle$ axis of PbSe rock salt is perpendicular to the plane of the sheet. Each nanocrystal unit is epitaxially connected to three other ones, forming $[100]/[100]$ connections. Silicene honeycomb structures of PbSe, very similar to the ones used here, have been structurally characterized in detail in a recent work.²³ It has been shown that while the honeycomb domains are very large ($> 10 \mu\text{m}$), there are several types of crystallographic defects, mostly related to non-ideal $[100]/[100]$ connections between the constituting NCs. Our electrolyte-gated transport measurements show that the injected electrons occupy the lowest conduction band. However, the injected holes might either occupy the valence band or localized in-gap states. The similarity between the mobility obtained with an electrochemically gated transistor type device and the THz mobility is remarkable (both values are about $1.5 \text{ cm}^2 \text{V}^{-1} \text{s}^{-1}$). This indicates that the quantum yield for charge carrier photo-generation in the terahertz experiments is close to unity, and also that mainly electrons contribute to the THz conductivity. From the above, it is thus reasonable to state that the electron mobility at room temperature is close to $1.5 \text{ cm}^2 \text{V}^{-1} \text{s}^{-1}$ and independent of frequency up to the

THz range. The frequency independence implies that charge transport over tens of microns in the transistor measurements (see Figure C3) is as efficient as along the distance (L) probed at THz frequencies which is the diffusion length during a period (t_{osc}) of the THz field; *i.e.* $L = \sqrt{\frac{4\mu_{dc}k_B T t_{osc}}{e}} \sim 5$ nm with k_B the Boltzmann constant and T the temperature. The value of L estimated in this way corresponds to the center-to-center distance between adjacent NCs. The similar mobility found for this short distance scale and the DC value implies that electronic coupling between the NCs exhibits long-range order. Hence, there is a strong electronic coupling between every two NCs, but also a high density of structural defects. This means that in both types of measurements electron transport is mainly limited by structural defects.

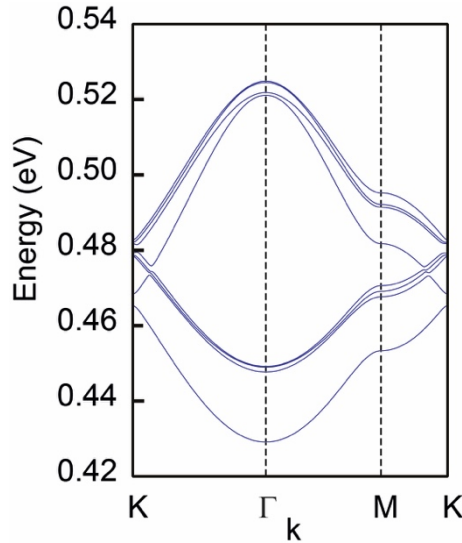


Figure 4.4. Tight binding (TB) of PbSe honeycomb superlattice. The lowest conduction bands calculated with atomistic tight-binding (TB) theory. The lowest conduction band is 8-fold degenerate (including spin); the degeneracy is slightly broken due to quantum coupling of the 4 L points in the zone. The bands show a conventional parabolic dispersion at the Γ -point, and a linear Dirac-type dispersion at the K-points. The calculated band structure yields an effective mass of $0.21 m_0$ for electrons (m_0 is the free electron mass).

Here we provide an interpretation of this result, using the band structure calculated for a PbSe silicene-type honeycomb structure with the same size of the honeycomb units (NCs) and periodicity. The lowest conduction bands calculated with atomistic tight-binding theory are shown in Figure 4.4. The lowest conduction band is 8-fold degenerate (including spin). It shows a conventional parabolic

dispersion at the Γ -point, and a linear Dirac-type dispersion at the K-points. When electrons are injected and the occupation is low, the (low-T) occupation is at the Γ -point. The effective mass of electrons, obtained from atomistic tight binding calculations is $0.21 m_0$ (see Figure 4.4). It is instructive to compare the mobility observed in the honeycomb superstructures with that reported for bulk PbSe. The experimental value for macroscopic crystals of PbSe at room temperature is $1000 \text{ cm}^2\text{V}^{-1}\text{s}^{-1}$.⁴⁵ When we assume that the effective mass in bulk PbSe is $0.1 m_0$,⁴⁶ the scattering time in a macroscopic PbSe crystal is calculated to be 60 fs, which is more than 10 times larger the value of 5.2 ± 0.6 fs we found for the honeycomb superlattice. For the PbSe superstructures, we find that the mobility is almost 500 times smaller than the bulk value, whereas the effective mass is only (here at the Γ -point) 2 times larger. This means that in our PbSe honeycomb superlattice the electron scattering time is considerably shorter than in the bulk PbSe; hence electrons do not only scatter at lattice phonons, but also at lattice imperfections. This is corroborated by the frequency dependence of the THz mobility. The real and imaginary parts cannot be described by the Drude model, which accounts only for electron-phonon scattering, but backscattering of electrons on defects needed to be included. The THz mobility could be reproduced approximately by the Drude-Smith model with $c = -0.96 \pm 0.01$, which implies strong backscattering of electrons at imperfections in the PbSe honeycomb superstructures. We believe that imperfect [100]/ [001] connections between the NCs are the most important origin of disorder in the PbSe honeycomb superstructures.

Several previous studies have yielded charge mobilities in PbSe NC solids in the range of $1\text{-}15 \text{ cm}^2\text{V}^{-1}\text{s}^{-1}$.^{6, 7, 10, 20, 28, 47-49} In these studies of 3-dimensional assemblies, the NCs were coupled by small organic linker molecules, and in some case the NC solids were thermally annealed or infilled with a metal oxide by atomic layer deposition. Apparently these treatments lead to somewhat high mobilities.^{3, 49} However, in the present case, please notice that our system is truly 2-D, this increases the relative surface area and, related to this, the density of surface trap states and also increases the effect of the inhomogeneous electrostatic potential. All these features have a negative effect on electron mobility.

4.4 Conclusions

We studied the electronic properties of PbSe honeycomb superstructures in a transistor type device and with THz spectroscopy. The results show that electrons

occupy the lowest conduction band. The electron mobility is limited by lattice imperfections. The electronic characterization at room-temperature presented here shows that it should be possible to subtly move the Fermi level through the energy range of the conduction mini-band. Once PbSe honeycomb transistor-type devices can be cooled down to cryogenic temperatures (*i.e.* $k_B T \ll$ band width), it should be possible to study the transport physics with the Fermi-level positioned in a narrow energy window, e.g. to distinguish the Γ point from K-points. Eventually, this research would enable to display the Dirac character of the carriers in the energy region around the K-points, as has been predicted by simple and advanced theories.

References

1. Talapin, D. V.; Murray, C. B., PbSe Nanocrystal Solids for n- and p-Channel Thin Film Field-Effect Transistors. *Science* **2005**, *310*, 86-89.
2. Vanmaekelbergh, D.; Liljeroth, P., Electron-conducting quantum dot solids: novel materials based on colloidal semiconductor nanocrystals. *Chemical Society Reviews* **2005**, *34* (4), 299-312.
3. Sandeep, C. S. S.; Azpiroz, J. M.; Evers, W. H.; Boehme, S. C.; Moreels, I.; Kinge, S.; Siebbeles, L. D. A.; Infante, I.; Houtepen, A. J., Epitaxially Connected PbSe Quantum-Dot Films: Controlled Neck Formation and Optoelectronic Properties. *ACS Nano* **2014**, *8* (11), 11499-11511.
4. Talapin, D. V.; Lee, J.-S.; Kovalenko, M. V.; Shevchenko, E. V., Prospects of Colloidal Nanocrystals for Electronic and Optoelectronic Applications. *Chemical Reviews* **2010**, *110* (1), 389-458.
5. Law, M.; Luther, J. M.; Song, Q.; Hughes, B. K.; Perkins, C. L.; Nozik, A. J., Structural, Optical, and Electrical Properties of PbSe Nanocrystal Solids Treated Thermally or with Simple Amines. *Journal of the American Chemical Society* **2008**, *130* (18), 5974-5985.
6. Oh, S. J.; Wang, Z.; Berry, N. E.; Choi, J.-H.; Zhao, T.; Gaubling, E. A.; Paik, T.; Lai, Y.; Murray, C. B.; Kagan, C. R., Engineering Charge Injection and Charge Transport for High Performance PbSe Nanocrystal Thin Film Devices and Circuits. *Nano Letters* **2014**, *14* (11), 6210-6216.
7. Oh, S. J.; Berry, N. E.; Choi, J.-H.; Gaubling, E. A.; Paik, T.; Hong, S.-H.; Murray, C. B.; Kagan, C. R., Stoichiometric Control of Lead Chalcogenide Nanocrystal Solids to Enhance Their Electronic and Optoelectronic Device Performance. *ACS Nano* **2013**, *7* (3), 2413-2421.
8. Luther, J. M.; Law, M.; Beard, M. C.; Song, Q.; Reese, M. O.; Ellingson, R. J.; Nozik, A. J., Schottky Solar Cells Based on Colloidal Nanocrystal Films. *Nano Letters* **2008**, *8* (10), 3488-3492.
9. Chiu, S.-C.; Jhang, J.-S.; Chen, J.-F.; Fang, J.; Jian, W.-B., Effects of cross-sectional area on the tunneling-junction array in octahedral PbSe colloidal-nanocrystal solids. *Physical Chemistry Chemical Physics* **2013**, *15* (38), 16127-16131.
10. Gao, Y.; Aerts, M.; Sandeep, C. S. S.; Talgorn, E.; Savenije, T. J.; Kinge, S.; Siebbeles, L. D. A.; Houtepen, A. J., Photoconductivity of PbSe Quantum-Dot Solids: Dependence on Ligand Anchor Group and Length. *ACS Nano* **2012**, *6* (11), 9606-9614.
11. Kang, M. S.; Lee, J.; Norris, D. J.; Frisbie, C. D., High Carrier Densities Achieved at Low Voltages in Ambipolar PbSe Nanocrystal Thin-Film Transistors. *Nano Letters* **2009**, *9* (11), 3848-3852.
12. Baumgardner, W. J.; Whitham, K.; Hanrath, T., Confined-but-Connected Quantum Solids via Controlled Ligand Displacement. *Nano Letters* **2013**, *13* (7), 3225-3231.
13. Koh, W.-k.; Bartnik, A. C.; Wise, F. W.; Murray, C. B., Synthesis of Monodisperse PbSe Nanorods: A Case for Oriented Attachment. *Journal of the American Chemical Society* **2010**, *132* (11), 3909-3913.

14. Cho, K.-S.; Talapin, D. V.; Gaschler, W.; Murray, C. B., Designing PbSe Nanowires and Nanorings through Oriented Attachment of Nanoparticles. *Journal of the American Chemical Society* **2005**, *127* (19), 7140-7147.
15. Schliehe, C.; Juarez, B. H.; Pelletier, M.; Jander, S.; Greshnykh, D.; Nagel, M.; Meyer, A.; Foerster, S.; Kornowski, A.; Klinke, C.; Weller, H., Ultrathin PbS Sheets by Two-Dimensional Oriented Attachment. *Science* **2010**, *329*, 550-553.
16. Whitham, K.; Hanrath, T., Formation of Epitaxially Connected Quantum Dot Solids: Nucleation and Coherent Phase Transition. *The Journal of Physical Chemistry Letters* **2017**, *8* (12), 2623-2628.
17. Castro Neto, A. H.; Guinea, F.; Peres, N. M. R.; Novoselov, K. S.; Geim, A. K., The electronic properties of graphene. *Reviews of Modern Physics* **2009**, *81* (1), 109-162.
18. Steckel, J. S.; Yen, B. K. H.; Oertel, D. C.; Bawendi, M. G., On the Mechanism of Lead Chalcogenide Nanocrystal Formation. *Journal of the American Chemical Society* **2006**, *128* (40), 13032-13033.
19. Kulkarni, A.; Evers, W. H.; Tomić, S.; Beard, M. C.; Vanmaekelbergh, D.; Siebbeles, L. D. A., Efficient Steplike Carrier Multiplication in Percolative Networks of Epitaxially Connected PbSe Nanocrystals. *ACS Nano* **2018**, *12* (1), 378-384.
20. Evers, W. H.; Schins, J. M.; Aerts, M.; Kulkarni, A.; Capiod, P.; Berthe, M.; Grandidier, B.; Delerue, C.; van der Zant, H. S. J.; van Overbeek, C.; Peters, J. L.; Vanmaekelbergh, D.; Siebbeles, L. D. A., High charge mobility in two-dimensional percolative networks of PbSe quantum dots connected by atomic bonds. *Nature communications* **2015**, *6*, 8195-8195.
21. Joyce, H. J.; Boland, J. L.; Davies, C. L.; Baig, S. A.; Johnston, M. B., A review of the electrical properties of semiconductor nanowires: insights gained from terahertz conductivity spectroscopy. *Semiconductor Science and Technology* **2016**, *31* (10), 103003.
22. Lloyd-Hughes, J.; Jeon, T.-I., A Review of the Terahertz Conductivity of Bulk and Nano-Materials. *Journal of Infrared, Millimeter, and Terahertz Waves* **2012**, *33* (9), 871-925.
23. Peters, J. L.; Altantzis, T.; Lobato, I.; Jazi, M. A.; van Overbeek, C.; Bals, S.; Vanmaekelbergh, D.; Sinai, S. B., Mono- and Multilayer Silicene-Type Honeycomb Lattices by Oriented Attachment of PbSe Nanocrystals: Synthesis, Structural Characterization, and Analysis of the Disorder. *Chemistry of materials* **2018**, *30* (14), 4831-4837.
24. Kalesaki, E.; Delerue, C.; Morais Smith, C.; Beugeling, W.; Allan, G.; Vanmaekelbergh, D., Dirac Cones, Topological Edge States, and Nontrivial Flat Bands in Two-Dimensional Semiconductors with a Honeycomb Nanogeometry. *Physical Review X* **2014**, *4* (1), 011010.
25. Alimoradi Jazi, M.; Janssen, V. A. E. C.; Evers, W. H.; Tadjine, A.; Delerue, C.; Siebbeles, L. D. A.; van der Zant, H. S. J.; Houtepen, A. J.; Vanmaekelbergh, D., Transport Properties of a Two-Dimensional PbSe Square Superstructure in an Electrolyte-Gated Transistor. *Nano Letters* **2017**, *17* (9), 5238-5243.
26. Wolcott, A.; Doyeux, V.; Nelson, C. A.; Gearba, R.; Lei, K. W.; Yager, K. G.; Dolocan, A. D.; Williams, K.; Nguyen, D.; Zhu, X. Y., Anomalous Large Polarization Effect Responsible for Excitonic Red Shifts in PbSe Quantum Dot Solids. *The Journal of Physical Chemistry Letters* **2011**, *2* (7), 795-800.

27. Fang, H.; Bechtel, H. A.; Plis, E.; Martin, M. C.; Krishna, S.; Yablonovitch, E.; Javey, A., Quantum of optical absorption in two-dimensional semiconductors. *Proceedings of the National Academy of Sciences* **2013**, *110*, 11688-11691.
28. Oh, S. J.; Berry, N. E.; Choi, J.-H.; Gauding, E. A.; Lin, H.; Paik, T.; Diroll, B. T.; Muramoto, S.; Murray, C. B.; Kagan, C. R., Designing High-Performance PbS and PbSe Nanocrystal Electronic Devices through Stepwise, Post-Synthesis, Colloidal Atomic Layer Deposition. *Nano Letters* **2014**, *14* (3), 1559-1566.
29. Araujo, J. J.; Brozek, C. K.; Kroupa, D. M.; Gamelin, D. R., Degenerately n-Doped Colloidal PbSe Quantum Dots: Band Assignments and Electrostatic Effects. *Nano Letters* **2018**, *18* (6), 3893-3900.
30. Boehme, S. C.; Vanmaekelbergh, D.; Evers, W. H.; Siebbeles, L. D. A.; Houtepen, A. J., In Situ Spectroelectrochemical Determination of Energy Levels and Energy Level Offsets in Quantum-Dot Heterojunctions. *The Journal of Physical Chemistry C* **2016**, *120* (9), 5164-5173.
31. Koh, W.-k.; Koposov, A. Y.; Stewart, J. T.; Pal, B. N.; Robel, I.; Pietryga, J. M.; Klimov, V. I., Heavily doped n-type PbSe and PbS nanocrystals using ground-state charge transfer from cobaltocene. *Scientific Reports* **2013**, *3*, 2004.
32. Wehrenberg, B. L.; Guyot-Sionnest, P., Electron and Hole Injection in PbSe Quantum Dot Films. *Journal of the American Chemical Society* **2003**, *125* (26), 7806-7807.
33. Wehrenberg, B. L.; Yu, D.; Ma, J.; Guyot-Sionnest, P., Conduction in Charged PbSe Nanocrystal Films. *The Journal of Physical Chemistry B* **2005**, *109* (43), 20192-20199.
34. Kaindl, R. A.; Hägele, D.; Carnahan, M. A.; Chemla, D. S., Transient terahertz spectroscopy of excitons and unbound carriers in quasi-two-dimensional electron-hole gases. *Physical Review B* **2009**, *79* (4), 045320.
35. Ambigapathy, R.; Bar-Joseph, I.; Oberli, D. Y.; Haacke, S.; Brasil, M. J.; Reinhardt, F.; Kapon, E.; Deveaud, B., Coulomb Correlation and Band Gap Renormalization at High Carrier Densities in Quantum Wires. *Physical Review Letters* **1997**, *78* (18), 3579-3582.
36. Hangleiter, A.; Jin, Z.; Gerhard, M.; Kalincev, D.; Langer, T.; Bremers, H.; Rossow, U.; Koch, M.; Bonn, M.; Turchinovich, D., Efficient formation of excitons in a dense electron-hole plasma at room temperature. *Physical Review B* **2015**, *92* (24), 241305.
37. Lauth, J.; Kinge, S.; Siebbeles Laurens, D. A., Ultrafast Transient Absorption and Terahertz Spectroscopy as Tools to Probe Photoexcited States and Dynamics in Colloidal 2D Nanostructures. In *Zeitschrift für Physikalische Chemie*, 2017; Vol. 231, p 107.
38. Lauth, J.; Kulkarni, A.; Spoor, F. C. M.; Renaud, N.; Grozema, F. C.; Houtepen, A. J.; Schins, J. M.; Kinge, S.; Siebbeles, L. D. A., Photogeneration and Mobility of Charge Carriers in Atomically Thin Colloidal InSe Nanosheets Probed by Ultrafast Terahertz Spectroscopy. *The Journal of Physical Chemistry Letters* **2016**, *7* (20), 4191-4196.
39. Ulbricht, R.; Hendry, E.; Shan, J.; Heinz, T. F.; Bonn, M., Carrier dynamics in semiconductors studied with time-resolved terahertz spectroscopy. *Reviews of Modern Physics* **2011**, *83* (2), 543-586.

40. Spoor, F. C. M.; Kunneman, L. T.; Evers, W. H.; Renaud, N.; Grozema, F. C.; Houtepen, A. J.; Siebbeles, L. D. A., Hole Cooling Is Much Faster than Electron Cooling in PbSe Quantum Dots. *ACS Nano* **2016**, *10* (1), 695-703.
41. Spoor, F. C. M.; Tomić, S.; Houtepen, A. J.; Siebbeles, L. D. A., Broadband Cooling Spectra of Hot Electrons and Holes in PbSe Quantum Dots. *ACS nano* **2017**, *11* (6), 6286-6294.
42. Smith, N. V., Classical generalization of the Drude formula for the optical conductivity. *Physical Review B* **2001**, *64* (15), 155106.
43. Bergren, M. R.; Kendrick, C. E.; Neale, N. R.; Redwing, J. M.; Collins, R. T.; Furtak, T. E.; Beard, M. C., Ultrafast Electrical Measurements of Isolated Silicon Nanowires and Nanocrystals. *The Journal of Physical Chemistry Letters* **2014**, *5* (12), 2050-2057.
44. Beard, M. C.; Turner, G. M.; Murphy, J. E.; Micic, O. I.; Hanna, M. C.; Nozik, A. J.; Schmittenmaer, C. A., Electronic Coupling in InP Nanoparticle Arrays. *Nano Letters* **2003**, *3* (12), 1695-1699.
45. Kittel, C., *Introduction to Solid State Physics*. 8 ed.; Wiley.
46. Kang, I.; Wise, F. W., Electronic structure and optical properties of PbS and PbSe quantum dots. *J. Opt. Soc. Am. B* **1997**, *14* (7), 1632-1646.
47. Liu, Y.; Tolentino, J.; Gibbs, M.; Ihly, R.; Perkins, C. L.; Liu, Y.; Crawford, N.; Hemminger, J. C.; Law, M., PbSe Quantum Dot Field-Effect Transistors with Air-Stable Electron Mobilities above $7 \text{ cm}^2 \text{ V}^{-1} \text{ s}^{-1}$. *Nano Letters* **2013**, *13* (4), 1578-1587.
48. Talgorn, E.; Gao, Y.; Aerts, M.; Kunneman, L. T.; Schins, J. M.; Savenije, T. J.; van Huis, M. A.; van der Zant, H. S. J.; Houtepen, A. J.; Siebbeles, L. D. A., Unity quantum yield of photogenerated charges and band-like transport in quantum-dot solids. *Nature Nanotechnology* **2011**, *6*, 733.
49. Balazs, D. M.; Matysiak, B. M.; Momand, J.; Shulga, A. G.; Ibáñez, M.; Kovalenko, M. V.; Kooi, B. J.; Loi, M. A., Electron Mobility of $24 \text{ cm}^2 \text{ V}^{-1} \text{ s}^{-1}$ in PbSe Colloidal-Quantum-Dot Superlattices. *Advanced Materials* **2018**, *30* (38), 1802265.

Appendix C

1. Oriented attachment. The oriented attachment of PbSe QDs to form honeycomb superlattices were performed following our recent slow process.¹ A dispersion of 2 μL of PbSe QDs (with concentration of 1.56×10^{-5} M) in 800 μL toluene was prepared (Figure C1A). A 6.5 mL petri dish with 28 mm in diameter was filled with ethylene glycol and used as a liquid substrate. This dish was placed in a bigger petri dish containing 3 mL toluene (Figure C1B). 350 μL of PbSe QDs dispersion in toluene was drop casted on top of the ethylene glycol substrate. A beaker was placed on top of the petri dishes to slow down the toluene evaporation (Figure C1C). After 16 hours, the solvent was evaporated and the honeycomb superlattice formed on the liquid-nitrogen interface (Figure C1D). The monolayer of the superstructure was transferred onto quartz substrates for THz measurement and electrochemical golden fingered electrodes for electrochemical gating measurements (Figure C1E).

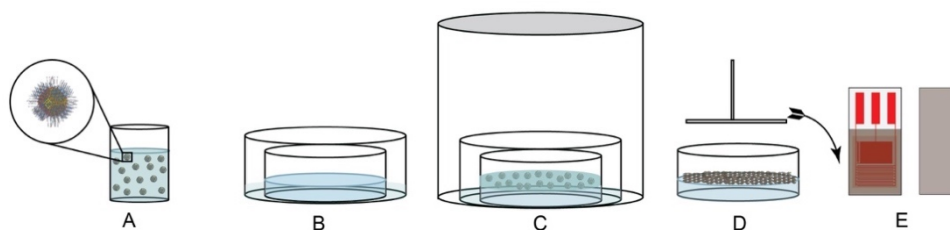


Figure C1. (A) dilution of QDs in toluene, (b) 6.5 mL petri dish with ethylene glycol as substrate inside a bigger petri dish containing 2 mL toluene, (c) drop casted QDs on top of the EG substrate and covered with a 500 mL beaker to slow down the toluene evaporation, (d) formation of honeycomb superlattices and stamping the superstructure on the solid substrates and (e) covered quartz substrate and fingered electrode by a monolayer of the structure.

2. Band structure of a honeycomb superstructure. Experiments show that atomically-coherent silicene-type honeycomb structures are formed by epitaxial attachment of the PbSe NCs via three of their 6 $\{100\}$ facets. In addition, substantial atomic rearrangement takes place during the attachment process. Inspired by the experimentally observed structures, we have considered the following model of silicene-like superlattice.^{2,3} The lattice is made of an ensemble of tangential spherical NCs, the center-to-center distance between nearest-neighbor NCs is equal to the NC diameter. Each sphere is connected to three other spheres along three out of the six $\langle 100 \rangle$ directions. Between each pair of neighbors, we add a cylinder of atoms which accounts for the atom rearrangement and the necking occurring during the oriented attachment process. The diameter of each NC is equal to 5.5 nm and the cylinder one is equal to 2.7 nm. Inside the spheres and the cylinders, the PbSe lattice is the same as in bulk, i.e., we

assume that there is no lattice relaxation. The surfaces are not passivated as this is not necessary in the case of PbSe for reasons discussed in Ref ⁴. Each atom in the lattice is described by a double set of $sp^3d^5s^*$ atomic orbitals including the spin degree of freedom. The tight-binding parameters including spin-orbit coupling are taken from Ref ⁴. Due to the large number (6415) of atoms per unit cell, the numerical methods described in Ref ⁵ are used to calculate near-gap states.⁵

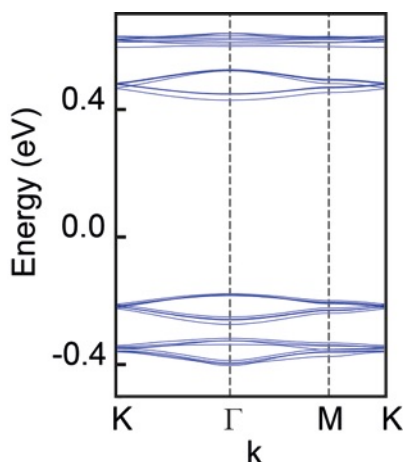


Figure C2. Conduction and valence band of a silicene-type PbSe honeycomb superlattice consisting of tangential spheres connected by cylinders.

3. Electrode design for gating measurement. Figure C3 shows the electrode design used for electrochemical gating measurements. The gold figure pattern is created by optical lithography on a SiO₂ substrate. These interdigitated fingers are spaced 10 to 50 μm apart, with a total device length between 9 and 1200 μm .

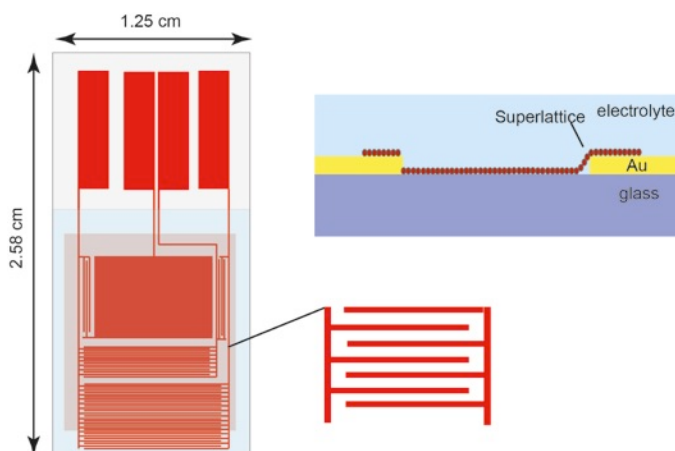


Figure C3. Electrode designs used for differential capacitance and conductivity measurements in an electrochemical gating setup.

4. Conductivity and mobility for electrochemical gating measurement. To calculate the charge density, we integrated the differential capacitance giving us the total amount of charge injected to the superstructure. Next, we should know the number of nanocrystals in the gated area of the electrode. For this purpose, we visually checked the area of the electrode covered by superlattices shown in Figure C4. It shows that the superlattice covers the whole active area. Some cracks are visible in the image, but they can hardly affect the electron transport between source and drain as many parallel transport paths exist. In addition, from the TEM images, we saw that not the whole area is covered by superstructure due to the empty places and cracks (Figure C5A). For the sample presented in this work, we estimated that 70% of the area is covered by the superlattices. To estimate the number of NCs in the covered area, we got an HAADF image and counted the number of presented NCs in the image which was equal to 34 (Figure C5B). The area of the image was $1.6 \times 10^{-15} \text{ nm}^2$. Therefore, the number of NCs in a cm^2 is equal to 2.2×10^{12} . Therefore, the number of charge per NC was: (D.7)

$$N = \frac{Q/e}{0.7 \times A \times 2.2 \times 10^{12}}. \quad (\text{C.1})$$

Where N is the number of charge per nanocrystal, Q is total charge injected to the superlattice, e is elementary charge and A is the area of the electrode where the superstructure was stamped on.

From the source-drain current versus applied potential shown in Figure C5, the conductance of the superstructure was determined. From the conductance and the fingers geometry, the conductivity of the superlattices was calculated:

$$\sigma = \frac{G \times w}{l \times h}. \quad (\text{C.2})$$

Where G is the conductance, w and l are the width and length of the fingers and h is the thickness of the honeycomb monolayer equal to 6.2 nm. From the charge per NC and the conductivity, the mobility of the honeycomb superlattice was calculated:

$$\mu = \frac{\sigma}{e \times \frac{N}{V}}. \quad (\text{C.3})$$

Where V is the volume of a NC considered as sphere.

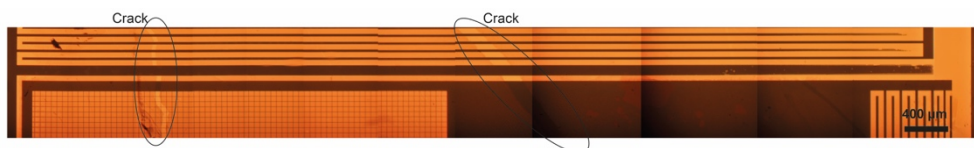


Figure C4. An optical microscope image of the film in the active channel of the device.

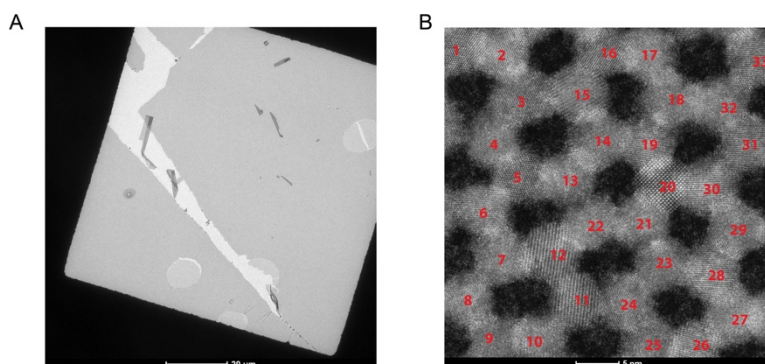


Figure C5. (A) Zoom out TEM image of the superstructure used to estimate the coverage of the sample on the electrode and (B) HAADF image of the honeycomb superlattice to estimate the number of NCs in a cm^2 area.

5. Source-drain current versus applied potential. We applied a step-wise potential of 55 mV between drain and source and measured the current vs applied potential in each step. As soon as the Fermi level is in the conduction band the current versus potential has linear (Ohmic) behavior. The line with a positive (negative) slope in each cross in Figure C6 represents the current versus applied potential for drain (source).

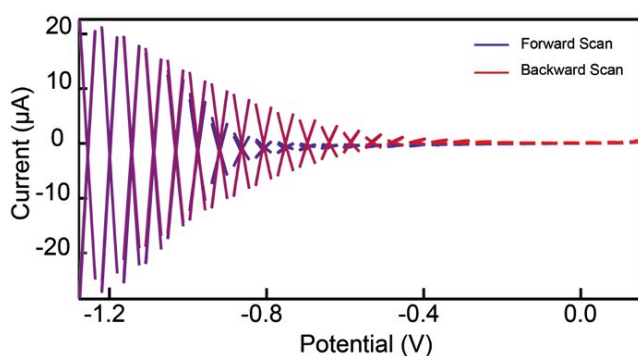


Figure C6. Source-drain current versus applied potential. In the forward scan when the potential is more negative than -0.7 V, the Fermi level is in the conduction band.

6. Transport measurements in an electrolyte-gated transistor on a non-treated honeycomb sample. Figure C7A shows the differential capacitance characterizing the injection of electrons into the honeycomb superlattice; electron injection sets on at -0.4 V and rises gradually until a sample potential of -1.2 V. The shapes of the forward and backward scans are very similar showing that electron injection and extraction are reversible in this potential window. At positive potentials, the differential capacitance raises again, showing that positive charge carriers are injected into the PbSe superstructure.

The total amount of injected charge carriers and the number of carriers per NC site ($=1/2$ unit cell) in the forward scan are depicted in Figure C7B. At the most negative potential (-1.2 V), we observed 8 electrons per NC site, meaning that the 8-fold degenerate S-type conduction band is, in principle, fully occupied.

As it can be observed in Figure C7C and C7D, the conductivity sets on at -0.4 V and rises with the electrochemical potential, up to 50 S/m at the most negative potential. The raise in the conductivity is pretty small for potentials more negative than -0.8 V, this is due to the fact for this device the interfacial PbSe superstructure/gold contact resistance starts to dominate over the resistance of the superstructure. The conductance onset agrees with the onset of the differential capacitance, showing that the injected electrons occupy conductive states only. While for electrochemical potentials positive of 0 V the differential capacitance increases again, this is not accompanied with an increase of the source-drain conductance. We conclude that positive charges are injected in the PbSe superstructure, but they occupy localized in-gap states.

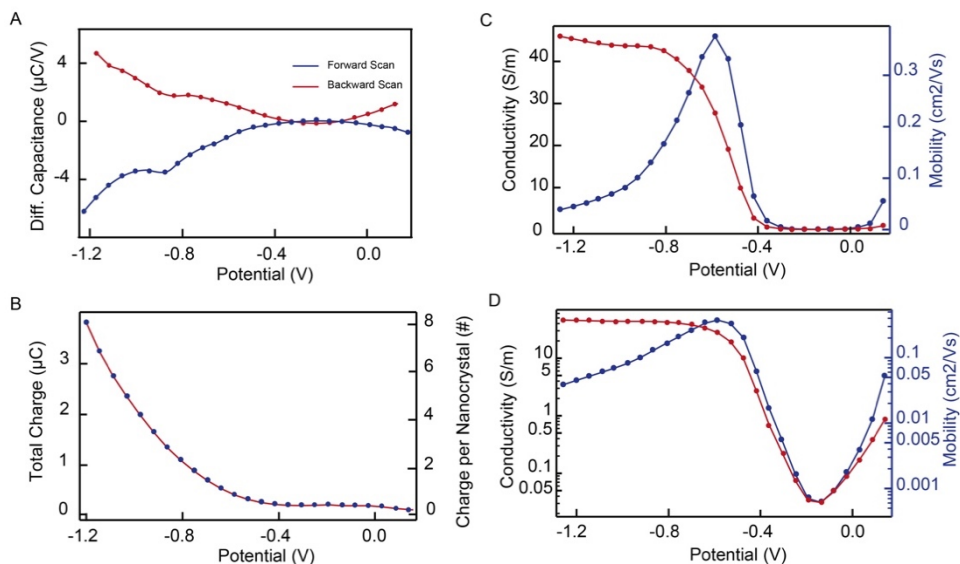


Figure C7. (A) Differential capacitance of a passivated PbSe honeycomb superlattice measured in forward (from 0.2 to -1.2 V) and backward scan. (B) The total injected charge and the charge per NC site as measured in the forward scan. (C) The conductivity (red) and the electron mobility (blue) of the superlattice obtained from the source-drain conductance, the geometry of the source-gap-drain fingers system and the charge density presented as a function of the electrochemical potential. (D) The conductivity (red) and the electron mobility (blue) of the superlattice in logarithmic scale.

7. Terahertz conductivity data.

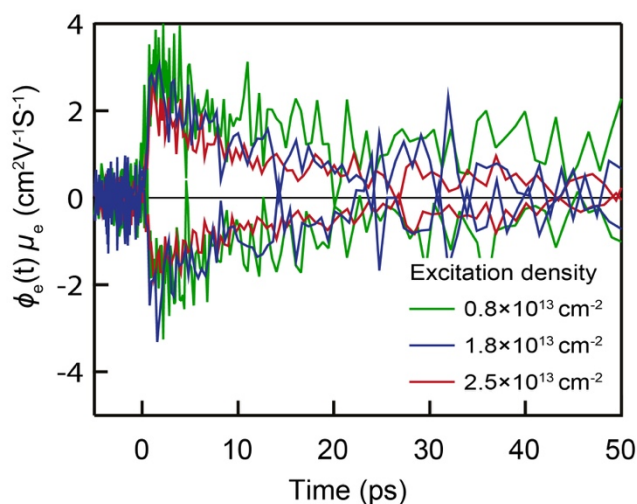


Figure C8. Product of quantum yield and mobility of electrons for excitation densities of $0.8 \times 10^{13} \text{ cm}^{-2}$, $1.8 \times 10^{13} \text{ cm}^{-2}$, and $2.5 \times 10^{13} \text{ cm}^{-2}$ which correspond to 3, 7, and 10 electron-hole pairs per NC, respectively.

8. Normalized real and imaginary part of the THz conductivity at different excitation densities.

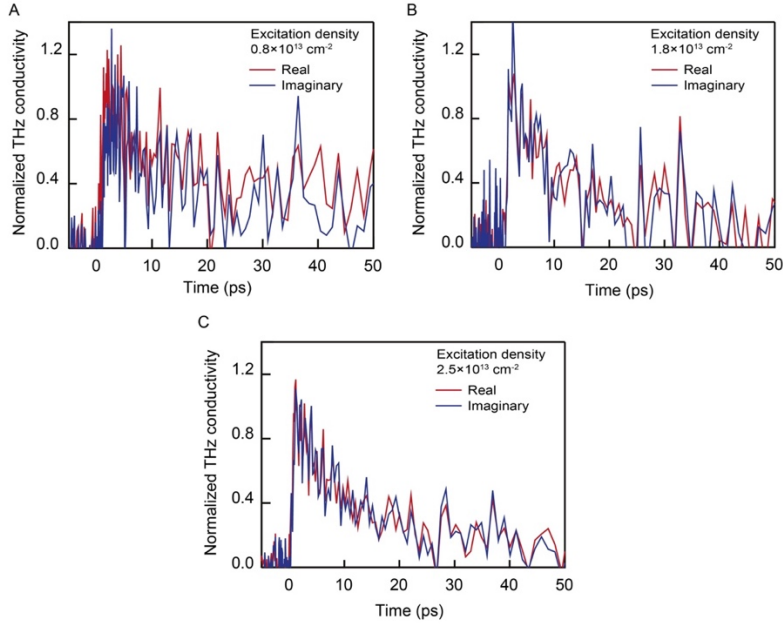


Figure C9. Normalized real and imaginary part of the THz conductivity at excitation densities (a) $0.8 \times 10^{13} \text{ cm}^{-2}$, (b) $1.8 \times 10^{13} \text{ cm}^{-2}$, and (c) $2.5 \times 10^{13} \text{ cm}^{-2}$.

9. Drude-Smith model fits to the frequency dependent electron mobility.

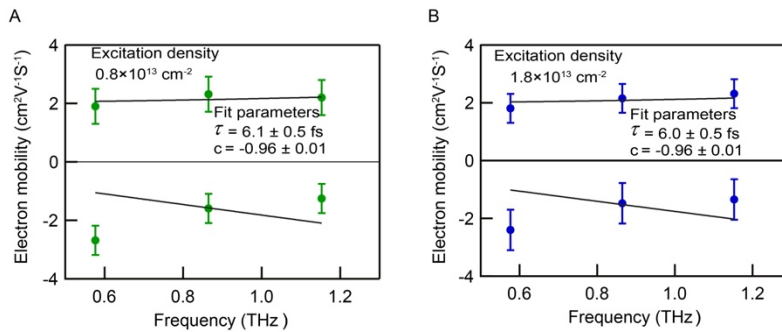


Figure C10. Drude-Smith model fits to the frequency dependent electron mobility for excitation densities of (a) $0.8 \times 10^{13} \text{ cm}^{-2}$, and (b) $1.8 \times 10^{13} \text{ cm}^{-2}$.

10. Comparative THz photoconductivity study on a PbCl_2 treated PbSe honeycomb structure and an untreated structure.

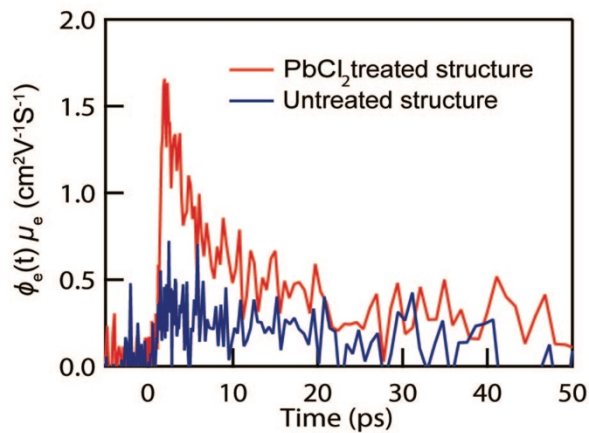


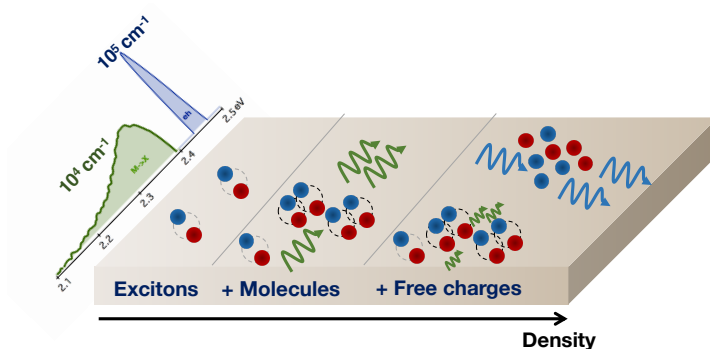
Figure C11. Product of quantum yield of electrons and electron mobility measured on a PbCl_2 treated honeycomb structure at excitation density $4.2 \times 10^{13} \text{ cm}^{-2}$ and an untreated honeycomb structure at excitation density $4.3 \times 10^{13} \text{ cm}^{-2}$.

References

1. Peters, J. L.; Altantzis, T.; Lobato, I.; Jazi, M. A.; van Overbeek, C.; Bals, S.; Vanmaekelbergh, D.; Sinai, S. B., Mono- and Multilayer Silicene-Type Honeycomb Lattices by Oriented Attachment of PbSe Nanocrystals: Synthesis, Structural Characterization, and Analysis of the Disorder. *Chemistry of materials : a publication of the American Chemical Society* **2018**, *30* (14), 4831-4837.
2. Delerue, C.; Vanmaekelbergh, D., Electronic band structure of zinc blende CdSe and rock salt PbSe semiconductors with silicene-type honeycomb geometry. *2D Materials* **2015**, *2* (3), 034008.
3. Tadjine, A.; Delerue, C., Colloidal nanocrystals as LEGO® bricks for building electronic band structure models. *Physical Chemistry Chemical Physics* **2018**, *20* (12), 8177-8184.
4. Allan, G.; Delerue, C., Confinement effects in PbSe quantum wells and nanocrystals. *Physical Review B* **2004**, *70* (24), 245321.
5. Niquet, Y. M.; Delerue, C.; Allan, G.; Lannoo, M., Method for tight-binding parametrization: Application to silicon nanostructures. *Physical Review B* **2000**, *62* (8), 5109-5116.

Chapter 5

A Charge Carrier Cooling Bottleneck Opens up Nonexcitonic Gain Mechanisms in Colloidal CdSe Quantum wells



Based on:

A Charge Carrier Cooling Bottleneck Opens up Non-Excitonic Gain Mechanisms in Colloidal CdSe Quantum Wells.

Renu Tomar, Aditya Kulkarni, Kai Chen, Shalini Singh, Dries Van Thourhout, Justin M Hodgkiss, Laurens D. A. Siebbeles, Zeger Hens, and Pieter Geiregat.

The Journal Physical Chemistry C, 2019, 123(14), 9640–9650.

5.1 Introduction

Two-dimensional (2D) materials are considered as prime candidates for realizing low-cost and tunable optoelectronic devices.^{1, 2} Applications in fields as diverse as light emission, photodetection and quantum optics can make use of the distinct and high-oscillator strength excitonic transitions and/or the tunable, narrow photoluminescence found in such material at room temperature.³⁻⁵ Recent years saw an increase in the number of available inorganic 2D materials such as transition metal dichalcogenide monolayers,³ layered perovskites⁶ and II- VI nanoplatelets.⁷ The strong Coulomb correlations leading to stable and strong excitonic features might be very beneficial for increasing the light-matter interactions required for large and/or low threshold optical gain. Several reports indicated for example low-threshold lasing using 2D materials.^{8, 9} However, since net modal gain only develops at very high carrier densities, the possible role of those exciton(s) (complexes) in the process remains unclear.¹⁰⁻¹² Indeed, within a mass-action model excitons and higher complexes such as excitonic molecules only form when the associated binding energy and pair density is sufficiently large. On the other hand, it is well-known that 2D excitons dissociate more readily to form unbound carriers at high excitation density. This effect is due to the density induced screening of the attractive Coulomb interactions which reduces the exciton binding energy, leading to so-called Mott transitions and overall intricate phase diagrams between insulating excitonic species and unbound charge carriers.^{10, 11, 13} Optical gain in epitaxially grown quantum wells, for example, is mostly mediated by an electron-hole plasma, even at cryogenic temperatures.¹⁴ Given the exceptionally large binding energy of excitons in colloidal 2D materials, in large due to reduced screening,¹⁵ it is not clear to what extent these concepts still hold.^{16, 17} As one of the few quantitative reports on the optical gain mechanism in 2D materials, Chernikov et al. observed a strong band-gap renormalization and transition to an unbound electron-hole plasma in WS₂ at high carrier density associated with the development of gain.¹⁸ This observation is remarkable given the large binding energies (> 300 meV) for the 2D excitons.¹⁹

It is clear that quantitative studies on optical gain are therefore much needed in order to assess the relation between stimulated emission and the complex mixture of carrier types that exists in strongly excitonic 2D materials at high density, such as 2D excitons, excitonic molecules and free charges.

CdSe 2D nanoplatelets, also called colloidal quantum wells, provide an excellent test-bed for this purpose as they can be obtained as scatter-free colloidal dispersions with high luminescence quantum yield and excellent colloidal stability.^{7, 20} Several

reports have demonstrated excellent light amplification properties using these colloidal quantum wells, such as large modal gains up to 500 cm^{-1} and low lasing thresholds down to tens of $\mu\text{J}/\text{cm}^2$, pointing towards a seemingly huge potential of these materials.^{8, 21-25} Apart from core only CdSe platelets, also more complex architectures have been studied such as core/shell and core/crown systems.^{26, 27} The development of optical gain in CdSe (-based platelets was how- ever studied mainly through thin-film measurements, where either amplified spontaneous emission (ASE) or lasing was employed.^{28, 29} Unfortunately, such approaches fail to elucidate the fundamentals of the gain mechanism, i.e. which type of interactions and excitations (free charge carriers, excitons, ...) are required to achieve net optical gain. Nor do they provide any prospect on the full potential of the material as the measured properties are inherently linked to the development of net stimulated emission dictated by the film and/or cavity losses.²⁵ A case in point here is the alleged threshold for stimulated emission, where energy densities (typically in $\mu\text{J}/\text{cm}^2$) are reported instead of generated excitation densities. Although energy densities have a high practical value, the density of carriers, i.e. the number of absorbed photons, is the most relevant parameter for a proper mechanistic understanding of optical gain in this unique class of materials. Nanoplatelets can be deceptive in this respect, as they offer larger intrinsic absorption coefficients at short wavelengths due to a reduced in-plane screening.³⁰

Herein, we report on an extensive quantitative study of optical gain development and the associated high excitation density photo-physics of colloidal 2D CdSe quantum wells. By combining a comprehensive set of femtosecond transient absorption, photoluminescence and terahertz spectroscopy, we were able to identify different optical gain regimes and a remarkable absence of a clear exciton Mott transition. At low electron-hole pair densities, a gain band appears at the low energy side of the heavy-hole exciton absorption that was assigned to stimulated emission by biexcitonic molecules.³¹ Here, we show that this exciton-mediated gain regime persist at pair densities well above the expected Mott density, where a transition of the exciton/molecule gas into an electron-hole plasma is expected. At $\sim 20000\text{ cm}^{-1}$, the saturated material gain in this regime is significantly larger than for comparable zero-dimensional materials, such as state-of-the-art CdSe/CdS or perovskite nanocrystals, and explains the observations of large modal gains in literature.^{25, 32-34} Apart from the exciton-mediated regime, a charge carrier cooling bottleneck manifests itself, which results in the peculiar co-existence of neutral excitonic species with unbound, hot electrons and holes. This combination leads to large, up to 10^5 cm^{-1} , and broadband material gain and luminescence, a second regime. At the same high excitation densities, we inferred a remarkable preservation of the exciton

polarizability, as evidenced by optical pump-terahertz probe experiments, and heavy and light-hole exciton oscillator strength, both of which indicates that a pure Mott-type transition does not occur. Our results show that even though strong excitonic features are not beneficial for the development of truly broadband gain, they do significantly increase the achievable material gain magnitude. Moreover, the extreme stability of the exciton gas in colloidal 2D materials will be beneficial for applications relying on the scattering of excitons at high density, such as exciton-polariton lasers.³⁵

5.2 Materials and methods

Synthesis of 4.5 ML platelets. Synthesis of 4.5 monolayer CdSe nanoplatelets was carried out by degassing cadmium myristate (0.34 g), Se (24 mg) and ODE (25 mL) in a three necked flask in vacuum and backfilling with N₂.^{7, 20} To this solution, 0.08 g of cadmium acetate was added at 205 °C when the solution turned yellow. Next, the solution was heated at 240 °C for 10 minute and 1.6 g of cadmium oleate in ODE was added at end. Samples were washed with a hexane/ethanol mixture. For spectroscopy, the CdSe platelets were dispersed in a transparent solvent (hexane) to achieve optical densities of 0.1 at the first heavy-hole exciton transition (510 nm). The photoluminescence quantum yield was determined using an integrating sphere after CW photo-excitation at 400 nm.

Quantification of absorbed photons per platelet. The average number of absorbed photons (or photo-generated electron-hole pairs) at time zero, here labeled $\langle N \rangle$, generated by a pump pulse at wavelength λ was calculated as

$$\langle N \rangle = J_{ph} \sigma_a . \quad (5.1)$$

Here J_{ph} is the photon fluence in photons/cm², σ_a is the absorption cross section of the platelets and A_λ is the sample absorbance at the pump wavelength. The beam size used for calculating J_{ph} is measured using a Thorlabs CCD Camera Beam profiler. The additional factor corrects for variation of the pump fluence along the pump beam path length. The cross-section is determined starting from the intrinsic absorption coefficient (see Appendix D2).

Ultrafast transient absorption spectroscopy. Samples were pumped using 110 femtosecond pulses (1 kHz) at varying wavelengths, created from the 800 nm fundamental (Spitfire Ace, Spectraphysics) through non-linear frequency mixing in

an OPA (TOPAS, Light Conversion). Broadband probe pulses were generated in a CaF₂ crystal using the 800 nm fundamental. The probe pulses were delayed using a delay stage with maximum delay of 3.3 ns (Newport TAS). Noise levels of 0.1 mOD (RMS) are achieved by averaging out over 5000 shots. The probe spectrum covers the VIS-NIR window from 350 nm up to 700 nm. Using 2 mm path length cuvettes, the samples were stirred during pump-probe measurements to avoid effects of photo-charging and sample degradation. Only at extreme densities ($\langle N \rangle > 150$) was sample degradation observed. No air-free sample handling was required as CdSe platelets are, under our conditions, insensitive to oxidation as is evidenced by a lack of PL peak shift or change in photoluminescence quantum yield when exposing samples to ambient conditions. No air-free sample handling was required as CdSe platelets are, under our conditions, insensitive to oxidation as is evidenced by a lack of PL peak shift or change in photoluminescence quantum yield when exposing samples to ambient conditions.

Ultrafast Photoluminescence Spectroscopy. For (ultrafast) photoluminescence (PL) spectroscopy, samples were measured using a cuvette with a 1 mm optical path length and an optical density of 0.1 at the heavy-hole absorption peak to avoid strong re-absorption. The quantum yield was determined using an integrating sphere with excitation at 400 nm. For the ultrafast experiments, samples were translated along 1 axis to avoid photo-charging. The detection of the broadband PL on femtosecond timescales was made possible by using a newly developed transient grating technique by Chen et al.³⁶ A Ti:Sapphire amplifier system (Spectra-Physics Spitfire Ace) operating at 3 kHz generating 100 fs pulses was split into two parts. One part was frequency doubled using a BBO crystal and focused to a 70 μ m spot on the sample. The photoluminescence is collimated using an off-axis parabolic mirror and refocused on a polished slice of fused silica. The second part of the 800 nm output was split using a 50:50 beam splitter creating two gate beams that are focused on the fused silica with a crossing angle of 5 degrees. The instantaneous grating generated by the interfering gate beams create an instantaneous gate which is used to temporally resolve the decay over a broad wavelength range. The scatter of the pump beam was suppressed using a 430 nm long-pass filter and the pump was set a magic angle relative to the PL collection. Data is averaged over 15000 shots for every time delay.

Terahertz spectroscopy. Samples were photo-excited by optical pump pulses of wavelength 480 nm and the photoconductivity due to mobile charge carriers and the polarizability of excitons was probed by single cycle THz pulses. The real part of the THz conductivity is due to in-phase charge velocity in the probing THz field and leads to a reduction of the amplitude of the THz field.^{37, 38} The imaginary THz

conductivity is due to the out-of-phase velocity of charges and the polarizability of excitons, leading to a phase retardation of the THz field.³⁸⁻⁴² Single cycle terahertz pulses were generated in a ZnTe non-linear crystal by optical rectification of 800 nm optical pulses of duration 60 fs, delivered from a chirped pulse amplified femtosecond laser system (Mira, Coherent), with a frequency of 1.4 kHz. The generated THz pulses were detected in a ZnTe crystal by the electro-optic effect with a chirped optical detection pulse, which encodes and decodes the entire THz pulse in a single laser shot. Optical pulses of wavelength 480 nm were generated in an optical parametric amplifier (TOPAS, Coherent). The THz conductivity due to charge carriers and excitons at time t after the laser pump pulse, that generates charges and excitons, was obtained from the differential THz field given by $\Delta E(t_p, t) = E_{excited}(t_p, t) - E_{unexcited}(t_p, t)$, where $E_{excited}(t_p, t)$ and $E_{unexcited}(t_p, t)$ are the transmitted THz field in the presence and absence of optical pumping, respectively. t_p is the delay between the THz generation and detection pulse. The real THz conductivity was obtained from the ratio $\frac{\Delta E(t_p^{max}, t)}{E_0(t_p^{max})}$, where t_p^{max} is the time at which the amplitude of the THz efield is maximum, according to:⁴³⁻⁴⁵

$$\sigma_R = \frac{2n_{sol}c\epsilon_0}{L} \frac{\Delta E(t_p^{max}, t)}{E(t_p^{max})}, \quad (5.2)$$

with $n_{sol} = 1.42$, the refractive index of n-hexane.⁴⁶ c the speed of light in vacuum, ϵ_0 the permittivity of free space, L the sample thickness. The imaginary THz conductivity was obtained from the differential THz field with t_p^{zero} the time at which the THz efield is zero, according to:^{40, 41, 44}

$$\sigma_I = \frac{2n_{sol}c\epsilon_0}{L} \frac{\Delta E(t_p^{zero}, t)}{E(t_p^{zero})}. \quad (5.3)$$

5.3 Results and discussion

CdSe platelets with a thickness of 1.37 nm, i.e. 4.5 monolayers, were synthesized according to Ihturria *et al.*^{7, 20} and their lateral dimensions were determined using brightfield transmission electron microscopy (TEM). While the measurements were repeated on multiple samples, all the data shown in the manuscript were recorded on

a sample measuring $34 \times 10 \text{ nm}^2$, see Figure 5.1A and Appendix D1. These dimensions are well above the $\sim 2 \text{ nm}$ Bohr diameter of the exciton, see further, leading to overall weak in-plane 2D confinement.

Figure 5.1A shows the intrinsic absorption and spontaneous emission spectrum of a dispersion of CdSe platelets in n-hexane. As is common for direct gap II-VI semiconductor quantum wells, two excitonic features are observed, attributed to the heavy (HH, 510 nm) and light hole (LH, 480 nm) exciton transitions.^{7, 48} The spontaneous photoluminescence (PL) has a high quantum yield of $> 50\%$ (see Methods) and shows no Stokes shift, indicating the absence of strong phonon-coupling,⁴⁹ fine-structure relaxation,⁵⁰ or spurious effects such as charging, exciton localization or trap-emission.⁴⁹ We represent the absorbance spectrum as an intrinsic absorption coefficient $\mu_{i,0}(\text{cm}^{-1})$, a quantity that is independent of the concentration of platelets in the dispersion analyzed.³⁰ $\mu_{i,0}$ can be calculated through theory as $\mu_{i,0}(300) = 5.9 \times 10^5 \text{ cm}^{-1}$, see Appendix D2, as validated experimentally by Achtstein *et al.*³⁰ Besides providing a means of normalizing linear and transient spectra, $\mu_{i,0}$ enables us to calculate the absorption cross section σ of a single platelet from the relation $\sigma(\lambda) = \mu_{i,0}(\lambda) \times V$, with V the platelet volume.⁴⁷ This brings us to a cross section of $8 \times 10^{-14} \text{ cm}^2$ at 400 nm for the platelets used here. Following the well-established methodology of epitaxially grown quantum wells, Figure 5.1B shows a decomposition of the absorbance spectrum into (C) step-like features representing 2D-continuum transitions and (X) narrow resonances representing the excitonic transitions.^{23, 48} This decomposition shows that the sharp exciton features are actually superimposed on a broadened step-profile, typical for the 2D density of states, which is due to free carrier transitions between the first of the 2D heavy-hole states to the first 2D conduction-band states C_{HH} , see also Inset of Figure 5.2B. At higher energy, a similar step associated with the light hole valence band is observed, denoted as C_{LH} . The fit also enables us to estimate the exciton binding energies $E_{b,X}$ as $193 \pm 5 \text{ meV}$ (HH exciton) and $277 \pm 13 \text{ meV}$ (LH exciton). Such figures are in excellent agreement with literature,^{51, 52} where the large values for the exciton binding energies are confidently ascribed to the reduced screening of the Coulomb interaction compared to bulk, given the low permittivity environment consisting of ligands and solvent.^{15, 49} Using the exciton binding energy, we can calculate the Bohr radius of

the 2D HH exciton using $m_r = 0.085$, $a_{B,HH} = \frac{\hbar}{\sqrt{2m_r E_{b,2D}}} = 1.52 \text{ nm}$.⁵³ Given

the area S of the nanoplatelets, we can define $\langle N_f \rangle$, as the number of excitons required to physically occupy all of the nanoplatelets surface area, i.e. the average inter-

exciton distance is the Bohr diameter. For our sample, this amounts to 45 excitations per platelet, a number that sets a scale for $\langle N \rangle$ in this particular system.

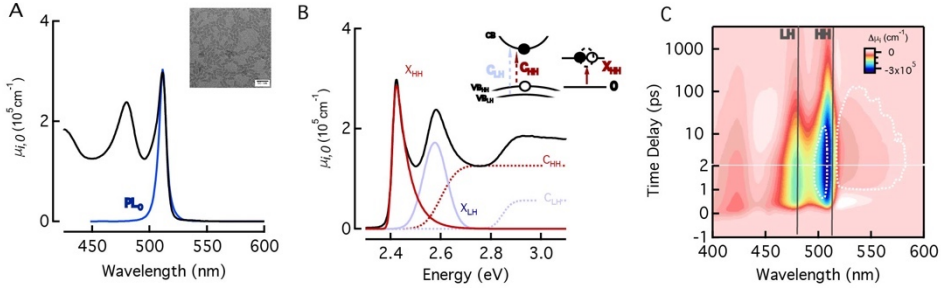


Figure 5.1. 4.5 monolayer (ML) colloidal CdSe quantum wells (A) Photoluminescence (blue) and linear absorption spectrum (black) of the CdSe nanoplatelets dispersed in n-hexane, where the latter is normalized to represent the intrinsic absorption coefficient $\mu_{i,0}$. Inset: Transmission Electron Microscope (TEM) image showing an average lateral area of $34 \times 10 \text{ nm}^2$ and no signs of stacking. (B) Absorption spectrum versus photon energy, decomposed into free carrier (C, dashed) and exciton (X, solid) contributions, both originating from the heavy (HH, red) and light hole (LH, blue) valence bands. Inset depicts the free carrier and exciton transitions. (C) Map of $\Delta\mu_i$, in cm^{-1} , for 400 nm photo-excitation creating $\langle N \rangle = 84$ as function of time (vertical axis) and probe wavelength (horizontal axis). The grey vertical lines indicate the position of the heavy (HH) and light (LH) exciton resonances. The white dashed contour indicates the regions where $|\Delta\mu_i| > \mu_{i,0}$, i.e. where net optical gain occurs.

Gain Spectroscopy. We analyzed the development of optical gain in dispersed CdSe platelets by a combination of femtosecond pump-probe transient absorption (TA), ultrafast photoluminescence (PL) spectroscopy and optical-terahertz probe spectroscopy (OTPT); see Methods section for technical details. All techniques involve the excitation of an ensemble of dispersed platelets using a 110-fs laser pulse at 400 nm, unless mentioned otherwise. In TA, photo-excitation is followed by probing the change in absorbance $\Delta A(\lambda, t) = A(\lambda, t) - A_0(\lambda)$, where A is the absorbance after photo-excitation and A_0 the absorbance in absence of pump pulse as a function of wavelength and pump-probe time delay. Note that the occurrence of optical gain, or net stimulated emission, at a given wavelength is most clearly evidenced by a negative non-linear absorbance $A = \Delta A + A_0 < 0$.

Starting from this non-linear absorbance $A(\lambda, t)$, the time- and wavelength-dependent intrinsic absorption coefficient of the NC under study can be calculated as,

$$\mu_i(\lambda, t) = \frac{A(\lambda, t)}{A_0(300)} \mu_{i,0}(300). \quad (5.4)$$

see also Appendix D2.³⁰ When μ_i turns negative, we have net stimulated emission for which $-\mu_i = g_i$ can be identified as the material gain. This quantity is independent of the measurement conditions and can be translated to any device or thin-film context through a rescaling with the appropriate modal confinement and volume fraction.³²

Figure 5.1C shows the shows a 2D time-wavelength map of $\Delta\mu_i$ recorded on a dispersion of nanoplatelets using excitation at 400 nm. As outlined in the Methods section and Appendix D2, the average excitation number $\langle N \rangle$ such a fluence brings about per platelet can be calculated from the product $J_{ph} \times \sigma_a$ of the photon flux and the absorption cross section, an exercise yielding $\langle N \rangle = 84$ for the data represented in Figure 5.1C. At these pumping levels, pronounced, long lived bleach features arise at the HH and LH exciton positions due to state-filling. Importantly, the absorbance at the pump wavelength remains nearly unaffected, implying no corrections are needed for the absorbed number of photons. At early times, a short-lived photo-induced feature occurs near 530 nm. This photo-induced absorption gets overtaken by a bleach signal at later times and was assigned to exciton-molecule transitions, opposed to the common notion of spectral shifts. Comparing the $\Delta\mu_i$ signal to $\mu_{i,0}$, we can readily identify regions of the 2D map where net optical gain occurs. These are indicated by the white dashed contour line in Figure 5.1C and remarkably show up both at the low and high energy side of the HH resonance.

To evaluate optical gain more precisely, we map out the regions of the spectrum where the material gain $g_i = -\mu_i$ turns positive. Figure 5.2A shows such a false color map for a higher excitation density corresponding again to an average photo-excitation density of $\langle N \rangle = 84$. We observe two distinct regimes of optical gain, separated from each other by the persisting heavy-hole absorption at 510 nm. First, a ≈ 60 nm (250 meV) wide gain band red-shifted from the HH-exciton peak is observed which persists for ca. 100 ps. This gain window coincides perfectly with reports on amplified spontaneous emission and lasing experiments on 4.5 ML CdSe nanoplatelets and recent theoretical work, see also Appendix D3.²³ At these high pump powers, an unexpected second window of optical gain develops at the high energy side of the HH-resonance. It offers significantly larger gain than the low energy band, builds up instantaneously, but is only sustained until ≈ 10 ps after photo-

excitation. Figure 5.2B shows the map of the PL under similar conditions of optical pumping as in Figure 5.2A. The emission spectrum is clearly broadened towards lower and higher photon energy compared to the spontaneous emission of a single exciton. Note that the spectrum decays asymmetrically, showing a shorter ≈ 10 ps lifetime for the high energy luminescence and a longer ≈ 100 ps lifetime for the red-shifted luminescence, overall very comparable to the material gain dynamics shown in Figure 5.2A.

Gain bands. To deepen our understanding of both gain regimes, we sweep the photo-generated density or average number of excitations per platelet $\langle N \rangle$ over two orders of magnitude, from nearly single excitations to close to 112 charge pairs per platelet. Note that the highest flux corresponds to a 2D pair density of $3.4 \times 10^{13} \text{ cm}^{-2}$. Figure 5.2C shows the intrinsic absorbance μ_i at 2.5 ps for these increasing densities. We observe that gain initially builds up on the low energy (long wavelength) side of the HH resonance. This first gain window is sustained throughout the entire density range. The gain in the blue-shifted regime is observed only when the excitation exceeds ca. 40. A number of intriguing observations can already be made at this point: the gain at the high energy side is disruptively larger than the low-energy gain; both the heavy and light hole exciton absorption persists, showing only slight saturation and effectively counteract broadband gain development; and at high density, a reduction of the absorbance plateau at shorter wavelengths (<480 nm) is observed.

Zooming in on the net material gain $g_i = -\mu_i$ in Figure 5.2D, shows that for the low energy gain band, the intrinsic gain coefficient in cm^{-1} reaches up to 18000 cm^{-1} and eventually saturates close to 84 excitations per platelet. Quantitative variable stripe length experiments verify such large gain coefficients are indeed achievable, see Appendix D3, and line up with the report of Guzelturk et al.²⁵

The gain at the blue side shows no signs of saturation and is also disruptively larger with values close to 10^5 cm^{-1} . A more detailed analysis of the gain threshold is shown in Figure 5.2E, see also Appendix D4, where we observe that the low energy gain band has a threshold of 4.1 ± 0.5 and the high energy gain band of 35 ± 2 , see also Appendix D4.

Finally, Figure 5.2F shows a similar fluence dependence as Figures 5.2C-D for the PL after 2.5 ps. Also, here, a transition occurs at ca. $\langle N \rangle = 35$ which is perhaps more clearly observed looking at the wavelengths (energies) for which the luminescence has its half-maximum value, as is shown in the inset of Figure 2F. A

gradual increase at the low energy side clearly contrasts the disruptive jump on the high energy side near $\langle N \rangle = 35$. These results show that not only are nanoplatelets able to amplify incoming probe light in the high energy gain window, they also exhibit spontaneous emission in the same spectral region, with a similar density-dependent onset. This is crucial for their use in lasers since the material's ability to amplify its own spontaneous emission is what sets it apart from optical amplifiers.

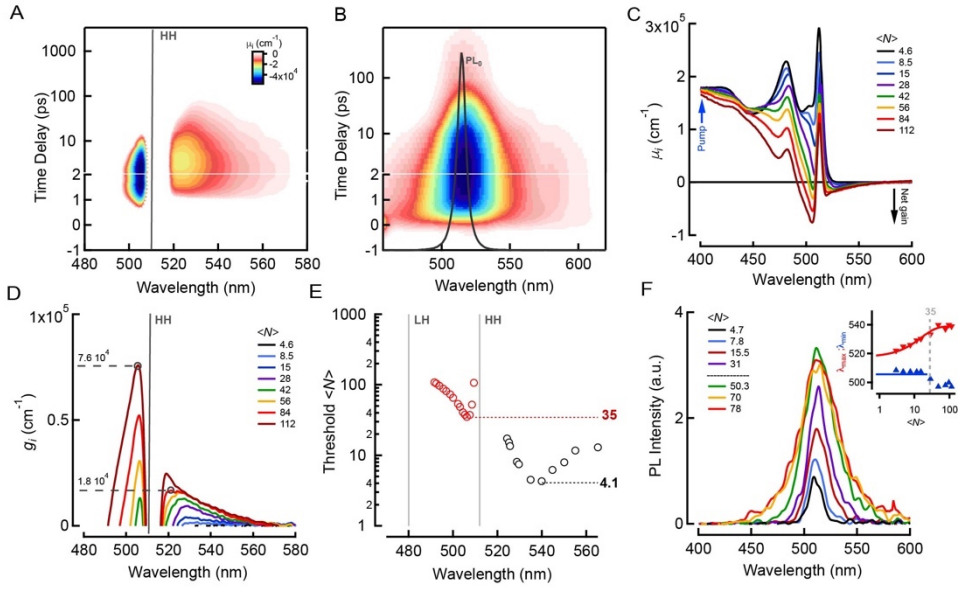


Figure 5.2: Optical gain at high carrier density after excitation with 400 nm. (A) 2D time-wavelength map of the intrinsic absorption coefficient μ_i (cm⁻¹) for $\langle N \rangle = 84$ where we limit the color scale to negative values showing net gain: $g_i = -\mu_i > 0$. The vertical line indicate the position of the heavy-hole exciton resonance. (B) 2D time-wavelength map of the PL taken at the same excitation density as (A). Black trace is the spontaneous emission for $\langle N \rangle \ll 1$. (C) Intrinsic absorption coefficients taken 2.5 ps after photo-excitation with a 400 nm pump pulse for densities ranging from 4.6 to 112 excitations per platelet. (D) Material gain spectra g_i for the same carrier densities as (c). (E) Required $\langle N \rangle$ to achieve transparency, $\mu_i(2.5\text{ps}) = 0$, as function of wavelength. Optical gain is achieved at 4.1 and 35 in the red and blue-shifted gain regimes respectively. (F) PL at 2.5 ps for increasing pair density from 4.7 to 78. The inset shows the FWHM wavelengths of the PL spectra.

As shown elsewhere, we assign the low energy gain band to stimulated emission from excitonic molecules.³¹ Such a biexcitonic molecule is a bound two-exciton state with a binding energy $E_{b,M} \approx 45$ meV for 4.5 ML CdSe platelets, outlasting thermal energy at room temperature and typical optical phonon energies of CdSe.^{48, 49} This

complex can recombine radiatively to a single exciton state, giving rise to stimulated emission and net amplification in a narrow band on the low energy side of the heavy-hole exciton absorption. The quantified material gain coefficients of the excitonic molecule gain mechanism shown here are close to 1 order of magnitude larger than observed for state-of-the-art CdSe/CdS or perovskite quantum dots,^{32, 34} which rationalizes recent reports on extremely small footprint lasers operating under low excitation power.^{22, 23} Appendix D5 shows that across the entire density range, exciton-exciton annihilation is the main culprit for the vanishing carrier density and hence the overall optical gain lifetime of ca. 100 ps, as confirmed by other reports.^{54, 55}

The exciton-mediated red-shifted gain window observed at low density persists through the entire density range and shows a saturation close to 100 excitations, see Figure 5.2D. The latter already indicates that excitonic species can indeed persist up to such high carrier densities. In particular for the biexcitonic molecules, which show a much smaller stabilization energy compared to excitons, this result is remarkable. An initial confirmation is found in the absence of a full collapse of the exciton oscillator strength as is observed via the preservation of the exciton luminescence, gain and absorption features, see Figure 5.2.

The exciton-mediated red-shifted gain window observed at low density persists through the entire density range and shows a saturation close to 100 excitations, see Figure 5.2D. The latter already indicates that excitonic species can indeed persist up to such high carrier densities. In particular for the biexcitonic molecules, which show a much smaller stabilization energy compared to excitons, this result is remarkable. An initial confirmation is found in the absence of a full collapse of the exciton oscillator strength as is observed via the preservation of the exciton luminescence, gain and absorption features, see Figure 5.2. However, before we analyze the limited exciton saturation in more detail, we want to unambiguously confirm the existence of excitons at high density.⁵⁶

Excitonic Stability at High Density. To this end, we employ optical pump-THz probe spectroscopy as, similar to previous studies on 2D InSe nanosheets,⁵⁷ one can use these measurements to characterize the nature of photo-excited species. The real component of the THz conductivity is due to free mobile charges moving with velocity in-phase with the THz field, while the imaginary conductivity is due to the out-of-phase velocity of charges (resulting from scattering) and the polarizability of excitonic species (see Methods).^{38, 39} Figure 5.3A shows the THz conductivity as a function of time after photo-excitation for $\langle N \rangle = 6$ and 53. The real conductivity is

much smaller than the imaginary component for both densities, which is a strong qualitative indication for a significant contribution from excitons. To get more insight into the contribution of excitons we plot the kinetics of the optical bleach at the HH transition due to excitons on top of the imaginary THz conductivity for comparable excitation densities. The decay kinetics of the bleach and imaginary THz conductivity are similar at lower and higher densities, indicating that the imaginary THz conductivity is mainly due to excitons.

The initial real THz conductivity $\Delta\sigma_R$ is given by:^{43, 57}

$$\Delta\sigma_R = \frac{eN_a\phi(n)\sum\mu_R}{L}, \quad (5.5)$$

with $\sum\mu_R$ the sum of the real components of the electron and hole mobility, ϕ the quantum yield of charges, e the elementary charge and N_a the number of absorbed photons per unit area in the sample solution with cuvette length L . As denoted, ϕ depends on the average pair density $n = \frac{\langle N \rangle}{S}$ where S is the average platelet area.

The imaginary THz conductivity $\Delta\sigma_I$ is given by the sum of the contribution of (localized) charges and excitons, according to:^{44, 57}

$$\Delta\sigma_I = \frac{eN_a}{L} \left(\phi(n)\sum\mu_I + (1-\phi(n))\frac{\alpha\omega}{e} \right), \quad (5.6)$$

with μ_I the sum of the imaginary electron and hole mobility, α the polarizability of excitons and ω the radian frequency of the THz electric field. The imaginary THz conductivity in Figure 5.3B increases close to linearly with $\langle N \rangle$ (or n). The sub-linear increase of the contribution of free charges observed in the real conductivity indicates $\phi(n)$ increases strongly sub-linearly. Given equation 5.6 and the observed linear increase with n , this implies a significant contribution of the second term in Equation 2, i.e. of excitons.

The fraction of free charges is dictated by the Saha equilibrium $e + h \rightleftharpoons X$, which assumes a thermal equilibrium between excitons and free charge carriers. In Appendix D6, this equilibrium is worked out formally. Using the Saha model at a temperature of 293 K, and fitting that to the experimental data with $\mu_{I,R}$ and the

exciton polarizability α as adjustable parameters, yields the drawn curves in Figures 5.3B. The real conductivity is reproduced with $\mu_R = 54 \pm 12$ cm²/Vs. For the imaginary conductivity we found $\mu_I = 7 \pm 5$ cm²/Vs and $\alpha = 3.1 \pm 0.2 \times 10^{-36}$ Cm²/V.

We remark that the Saha equation can fit the data reasonably well beyond the broadband gain onset of $\langle N \rangle = 35$, see Figure 5.3B. We should however proceed with caution in this regime for two reasons. The temperature of the system is not well defined beyond this density and most likely above room temperature, as is evidenced by detailed analysis of the PL (see further), and (b) full occupation of the platelet occurs around the same number, $\langle N_f \rangle = 45$, as derived earlier. The first observation complicates the validity of the Saha fitting procedure as thermal equilibrium is not guaranteed, whereas the second observation indicates possibly stronger carrier scattering limiting the mobility and hence possibly saturating the transient real conductivity.

In any case, the THz results unambiguously show that across the entire density range probed in this work, excitons are present with no significant change in the polarizability compared to the isolated, low density regime. This agrees with the observation that the red- shifted gain window, assigned to excitonic species, can persist up to the highest densities used here. For the highest carrier density employed

in this work (112), the average inter-exciton is only, $d_s = 2 \sqrt{\frac{S}{\pi \times \langle N \rangle}} = 1.9$ nm, fairly

close to the Bohr diameter estimated earlier. Though exciton carrier phase diagrams can be very complex, a general understanding is that a so-called Mott-type transition should occur at these separations. Closely tied to the transition of an exciton gas into a conductive phase is the saturation and spectral shifting of the exciton absorption line itself. In concert with this, the exciton line will also undergo spectral shifts for increasing density due to a balance between renormalization of the band gap (redshift) and reduction in exciton binding energy (blueshift).⁵⁸⁻⁶⁰ Figure 5.3C shows the evolution of the normalized oscillator strength of the HH -exciton line, extracted from the integrated HH-peak area (see Appendix D2), and the heavy-hole spectral

shift ΔE_{HH} , for increasing excitation density. A qualitative fit, $\frac{f}{f_0} = \frac{1}{1 + \frac{\langle N \rangle}{\langle N \rangle_s}}$, to

the oscillator strength indicates a characteristic saturation density $\langle N \rangle_s = 12.7$. A full Mott-transition is however not observed as the oscillator strength persists up to $\langle N \rangle = 112 \approx 10 \langle N \rangle_s$, with a lingering strength of ca. $0.25 f_0$. This observation indicates

new types of carriers, or interactions between them, manifest themselves at higher density, a point we will elaborate further in the following section.

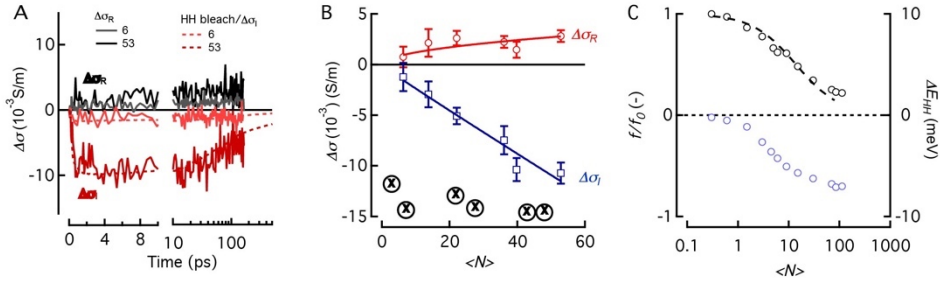


Figure 5.3. THz spectroscopy (A) Real (positive traces) and imaginary (negative traces) components of the THz conductivity as a function of time after photo-excitation with $\langle N \rangle$ equal to 6 and 53. The optical bleach at the heavy hole (HH) exciton transition at comparable densities is shown for comparison with the imaginary THz conductivity. (B) Measured real (red circles) and imaginary (blue squares) THz conductivity averaged between 6 and 10 ps after photo-excitation as a function of $\langle N \rangle$, together with fitted results from the Saha model (solid lines). Inset below shows a schematic depiction of the inter-exciton distance for this density range. (C) Reduction of normalized HH oscillator strength (red circles) and HH spectral shift ΔE (blue triangles), normalized to the HH binding energy, for increasing carrier density.

Finally, the exciton line shows a clear red-shift indicating that band gap renormalization overtakes the blueshift that would originate from a binding energy reduction through increased screening of the exciton.¹⁴ Our quantitative observations on CdSe are in-line with recent observations on other high binding energy 2D materials such as WS₂, where similarly a red-shift and no full saturation of the exciton line was observed until densities of $5 \times 10^{12} \text{ cm}^{-2}$, equivalent to $\langle N \rangle = 16$ for our experiments, yet at slightly higher densities, Chernikov *et al.* showed the exciton line does get fully saturated and a transition to free carrier-mediated gain takes over.^{18, 61}

Gain via Unbound Charge Carriers. Having established the excitonic nature of the universal gain regime at low photon energy, it remains an open question what causes the short-lived broadband gain and luminescence at high photon energy just after strong photo-excitation. To deepen our understanding, we first conceptualize how charge carrier thermalize and excitons are formed in direct gap polar semiconductors. Upon photo-excitation with 400 nm (3.1 eV), free electrons and holes with significant excess energy are created. These ‘hot’ carriers have to cool down by optical phonon emission and finally condense into a heavy-hole exciton, see Figure 5.4A.^{48, 60} This is quite a remarkable process as the stabilization of the exciton alone, i.e. its binding energy, requires the dissipation of close to 200 meV. Given typical phonon energies

of $E_{LO,CdSe} \approx 26$ meV, this implies multiple optical phonons need to be emitted.⁴⁹ Several reports in literature indicated that this coupling to phonons is relatively weak for single excitons and gets even more slowed down with increasing excitation density, hence slowing down exciton formation after non-resonant excitation.^{49, 62, 63} Nonetheless, we observe a sub-picosecond, near resolution-limited, buildup of the band edge exciton population and the associated gain at low exciton densities. To understand how a cooling bottleneck can still manifest with such fast single exciton formation, we should consider the accumulative nature of the phonon emission process, see also Figure 5.4A.^{48, 64} At early times, carriers cool down extremely fast to the band edge by rapid phonon emission, denoted as stage (1) in Figure 5.4A, giving rise to fast buildup of exciton PL and band-edge bleach, stage (2). However, as more carriers cool down the phonon population increases up to a point where the temperature (occupation) of (a subset of) the phonon mode(s), generalized as T_q , exceeds that of the electronic system, generalized as T_e . At this point, net energy transfer to the phonon bath will substantially reduce, giving rise to a cooling bottleneck for the remaining carriers. Overall, this would result in the formation of a hot electron-hole gas which cannot cool down effectively to form excitons. This will eventually lead to spontaneous and also stimulated emission from unbound charge carriers from higher energy free carrier states.

Key elements to validate the proposed model are (a) the (prolonged) occupation of high energy levels corresponding to unbound charges and (b) an increase of the overall carrier temperature, i.e. a modified distribution of charge carriers over those high energy states. The TA and luminescence data in Figure 5.2 already show that we can indeed attain a significant amount of carriers occupying energy levels blue-shifted from the HH line since we achieve spontaneous emission and net amplification of incoming probe light in that spectral window. As the TA data is congested due to the overlap of several spectral features (bleach, induced absorption, shifts, ...), we focus here on the PL data to extract additional information on the unbound charge carrier distribution, i.e. their temperature and absolute number density.

Figure 5.4B shows the high energy tail of the normalized photoluminescence (PL) spectrum 2.5 ps after photo-excitation with 400 nm, for increasing excitation density from $\langle N \rangle = 1.9 - 78$. We clearly observe both an increased emission at higher energy and a change in the slope of the high energy tail. The latter indicates that the distribution of the carriers over the high energy levels is changing, not just the occupation of the levels themselves.

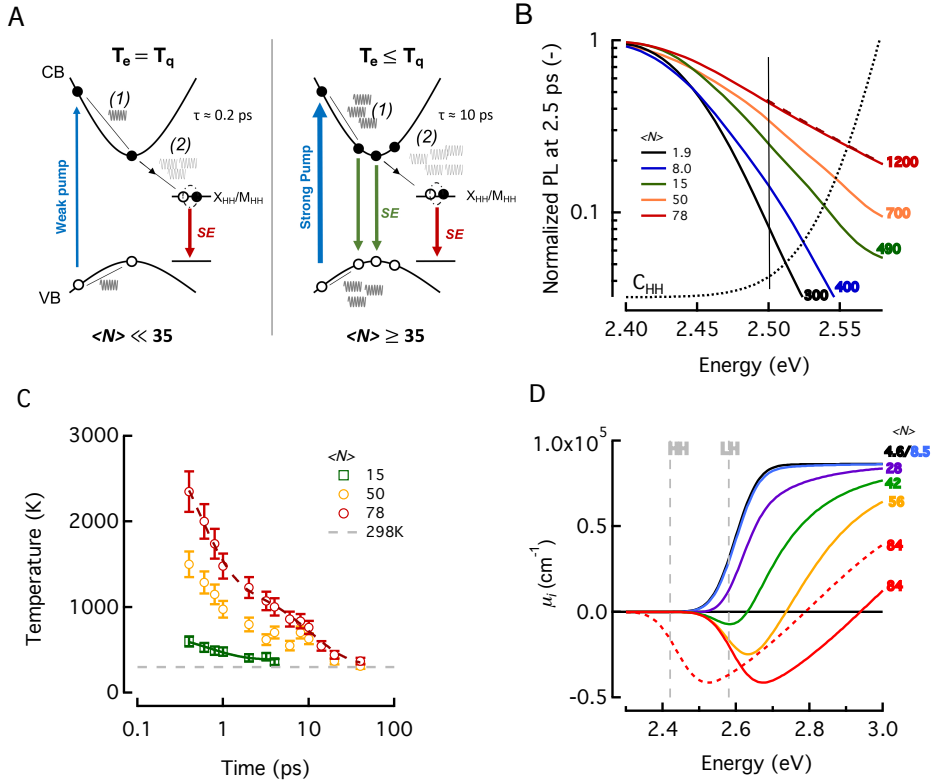


Figure 5.4: (A) Schematic explaining the effect of a phonon emission bottleneck on the various stages (1), (2) of exciton formation in a low (left) and high (right) density regime and the associated stimulated emission (SE) pathways. (B) Normalized photoluminescence (PL) for increasing pump fluence, 2.5 ps after photo-excitation with 400 nm (3.1 eV). The dashed fits indicate a Boltzmann approximation to the decaying high energy tail of the PL, the latter delineated by the vertical solid line. The thus extracted temperatures are labeled on the traces from 300 K (black) to 1200 K (red). Dotted black line is the free charge carrier transition C_{HH} , see also Figure 5.1B. (C) Dynamics of carrier temperature for various excitation densities. Solid lines are restricted fits, see main text. (D) Calculated intrinsic absorption coefficient of the heavy-hole associated free carrier transition for increased carrier density. The dashed red line shows the result at the highest density combined with a band gap renormalization (BGR) of 150 meV.

Fitting the decaying tail with a Boltzmann distribution,⁴⁸ $I(\hbar\omega) = e^{-E-E_f/K_B T_e}$, we are able to extract an effective carrier temperature T_e which starts off at 300 K for low excitation density and reaches up to 1200 K for $\langle N \rangle$ close to 80. A Boltzmann fit is a good approximation if we restrain the fit to high energies (> 2.5 eV; 496 nm) effectively matching the expected energy range of free carrier related transitions,

shown by the dotted black curve in Figure 5.4B. Appendix D7 shows moreover that quasi-Fermi level shifts are limited.⁴⁸ The lower density limit corresponds well to the data of Sippel et al., who found similar carrier temperatures at low densities.⁶²

Figure 5.4B shows the full dynamics of the extracted temperature for three initial excitation densities: 15, 50 and 78. A single component fit of the lowest density trace shows that the temperature decay is initially very fast with a characteristic lifetime of $\tau_l = 355 \pm 35$ fs. Fixing this fast lifetime, we can also do a restricted two-component fit on the high density kinetic trace and find a second component of 10 ± 1.4 ps. The latter matches well with the observed gain lifetime in the high energy region, see Figure 5.2A. This two-stage cooling corresponds well to the notion of initial fast LO phonon emission followed by a bottleneck caused by overheating of the phonon bath.

Having established that there is a population of high energy unbound carriers with elevated temperature, we can now rationalize their role in optical gain development. Looking closer at the TA data of Figure 5.2C, we observe that at high enough density (Figure 5.2C), the high-energy plateau (< 495 nm; 2.50 eV) of the absorbance starts to collapse. Looking back at Figure 5.1B, this plateau is formed by the staircase absorption profile of a 2D electron gas, in particular from the quantized heavy-hole valence band to the conduction band. Filling up these energy levels will indeed lead to a bleach of the plateau C_{HH} and eventually optical gain, as is observed for densities above ca. 35 electron-hole pairs. To gain more insight, we calculated the intrinsic absorption coefficient for varying carrier densities, considering only the heavy hole continuum C_{HH} of Figure 5.1C, see also Appendix D7. In Figure 5.4D, we obtain both the experimentally observed collapse of the absorbance and a clear transition from net absorption to optical gain. A detailed zoom around the gain threshold is shown in Figure D6 and reveals a gain threshold close to 20 excitations. This number is substantially larger than the molecule mediated gain threshold (4.1) but slightly lower than the observed $\langle N \rangle = 35$, see Figure 5.2E. This is to be expected since not all excitations are unbound charge carriers and competing LH/HH absorption will counteract the gain buildup. The correspondence of the experimental high energy gain data with the classical quantum well gain model is excellent as also the gain magnitude, e.g. $5 \times 10^4 \text{ cm}^{-1}$ for $\langle N \rangle = 84$ is retrieved. However, the gain from free carriers is at slightly higher energy than observed experimentally. It is however well established that strongly photo-excited (2D) semiconductors show strong band gap renormalization (BGR).⁵⁹ Estimates based on universal models

indicate shifts of 2 excitonic Rydberg's $\left(Ry_{2D} = \frac{2e^2}{\epsilon_0 a_{B,2D}} \right)$ up to a density of

$\langle N_f \rangle (= 45)$ and reaching even up to a $4 R_{y_{2D}}$ for higher densities. For CdSe, this would amount to shifts of 60 meV at low density and up to 240 meV at higher density. Figure 5.4C shows that such a moderate 150 meV renormalization for the highest density indeed pushes the optical gain window in between the two exciton resonances, exactly where optical gain is observed.

Discussion. The increased formation of free charge carriers at elevated carrier temperatures and densities over excitons explains the observations made in Figure 5.3C on the lack of exciton saturation and blueshift. Indeed, exciton saturation through state-filling will be ineffective since carriers do not thermalize to occupy the band edge levels and additionally, a gas of unbound two-dimensional charge carriers is considered less effective at screening Coulomb interactions than cold excitons.¹⁴ Also the persistent exciton redshift, as was observed in Figure 5.3C, can be rationalized this way since the position of the exciton transition is a balance between bandgap renormalization (BGR) and screening-induced blueshifts. The latter are too weak to overcome the substantial BGR and the overall line redshifts. The remarkable absence of a full Mott-type transition merits further theoretical investigation. Several estimates of this Mott density exist, based on dynamic or static screening arguments.⁵⁹ Static screening would put the Mott transition $na_B^2 = 0.1$, which for our system would amount to a mere $\langle N_f \rangle \approx 14$, clearly a huge underestimation.¹⁴

A possible explanation for the high energy gain window could be the emission/gain from multi-excitons, similar to what is observed in colloidal 0D CdSe-based quantum dots.^{31, 33} It is however important to stress that the photo-physics of excitons in 2D materials is fundamentally different of that found in zero-dimensional systems. The example of biexciton formation is illustrative for this purpose. Whereas in a 0D system, excitons have due to spatial localization no choice than to form the bi-exciton state, either repulsive or attractive, this is not valid for a 2D system with lateral extent (326 nm^2) much larger than the exciton size (7.2 nm^2). Indeed, if the interactions between excitons are repulsive in a 2D system, the excitons simply do not stabilize and retain their single exciton characteristics. As such, repulsive exciton interactions cannot explain the blue-shifted gain window. Another '0D'-argument could be that we are just observing state-filling where optical gain will manifest itself first on the low energy side and then span out to higher transitions, such as P-type transitions found in QDs, upon increased population.³¹ First off, this contradicts our observation that the heavy-hole exciton line persists in absorption, see Figure 5.2C/3C. If state-filling was applicable, it should quench similar to the absorption line in 0D quantum dots saturates (and inverts) when the population reaches (half of)

the band edge degeneracy and then span out to provide gain of excited exciton states.³³ Moreover, fluorescence and gain of non-thermalized excitons holds no ground since only zero momentum ($K=0$) transitions are allowed for 2D excitons.⁴⁸ Finally, the density of states at the band edge is enormous in a 2D system. Even modest estimates of the number of available states NS in the 50 meV window taken up by the HH line, puts the number at ca. 230, see Appendix D8. An additional proof that state-filling plays no role is found by exciting the system at 480 nm. Significantly less energy, ca. 500 meV, needs to be dissipated in this case, leading to much more efficient thermalization. Using the same exciton density, we observe only limited blue-shifted gain under these conditions with a much narrower bandwidth, again evident that exciton state filling cannot explain the blue-shifted gain window.

5.3 Conclusions

We have quantified and modeled the distinctive mechanisms leading to room temperature optical gain in 2D CdSe nanoplatelets, a model system for colloidal 2D materials. At high charge carrier density, a phonon bottleneck slows down hot carrier cooling leading to a unique situation of strong light amplification by unbound charge carriers, up to 10^5 cm^{-1} , and excitonic molecules simultaneously. The remarkable retention of excitonic features until extreme densities indicated an absence of a full Mott-type collapse of the exciton gas, as confirmed by THz spectroscopy. Although it shows from our results that this remarkable property is not directly beneficial for development of very broadband stimulated emission due to lingering exciton absorption, it does indicate gain at high exciton densities is feasible with concomitantly high gain coefficients. Moreover, it could render other applications possible such as high brightness LEDs or more complex devices relying on high density multi-exciton phenomena such as Bose-Einstein condensation.⁶⁵ Indeed, the latter are often hampered by exciton instability at high carrier densities, a problem which is absent in these high exciton binding energy quantum wells.^{35, 66} Clearly, (colloidal) 2D materials hold great promise to realize small footprint, low threshold micro lasers. Hence, it would be of great interest to see how these observations translate to other 2D material systems with different types of carrier-carrier and carrier-phonon interactions such as transition metal di-chalcogenides or layered perovskites.^{3, 6, 11}

References

1. Kovalenko, M. V.; Manna, L.; Cabot, A.; Hens, Z.; Talapin, D. V.; Kagan, C. R.; Klimov, V. I.; Rogach, A. L.; Reiss, P.; Milliron, D. J.; Guyot-Sionnest, P.; Konstantatos, G.; Parak, W. J.; Hyeon, T.; Korgel, B. A.; Murray, C. B.; Heiss, W., Prospects of Nanoscience with Nanocrystals. *ACS Nano* **2015**, 9 (2), 1012-1057.
2. Kagan, C. R.; Lifshitz, E.; Sargent, E. H.; Talapin, D. V., Building devices from colloidal quantum dots. *Science* **2016**, 353.
3. Xia, F.; Wang, H.; Xiao, D.; Dubey, M.; Ramasubramaniam, A., Two-dimensional material nanophotonics. *Nature Photonics* **2014**, 8, 899.
4. Wang, Q. H.; Kalantar-Zadeh, K.; Kis, A.; Coleman, J. N.; Strano, M. S., Electronics and optoelectronics of two-dimensional transition metal dichalcogenides. *Nature Nanotechnology* **2012**, 7, 699.
5. Bie, Y.-Q.; Grosso, G.; Heuck, M.; Furchi, M. M.; Cao, Y.; Zheng, J.; Bunandar, D.; Navarro-Moratalla, E.; Zhou, L.; Efetov, D. K.; Taniguchi, T.; Watanabe, K.; Kong, J.; Englund, D.; Jarillo-Herrero, P., A MoTe₂-based light-emitting diode and photodetector for silicon photonic integrated circuits. *Nature Nanotechnology* **2017**, 12, 1124.
6. Manser, J. S.; Christians, J. A.; Kamat, P. V., Intriguing Optoelectronic Properties of Metal Halide Perovskites. *Chemical Reviews* **2016**, 116 (21), 12956-13008.
7. Ithurria, S.; Tessier, M. D.; Mahler, B.; Lobo, R. P. S. M.; Dubertret, B.; Efros, A. L., Colloidal nanoplatelets with two-dimensional electronic structure. *Nature Materials* **2011**, 10, 936.
8. Ye, Y.; Wong, Z. J.; Lu, X.; Ni, X.; Zhu, H.; Chen, X.; Wang, Y.; Zhang, X., Monolayer excitonic laser. *Nature Photonics* **2015**, 9, 733.
9. Zhao, L.; Shang, Q.; Gao, Y.; Shi, J.; Liu, Z.; Chen, J.; Mi, Y.; Yang, P.; Zhang, Z.; Du, W.; Hong, M.; Liang, Y.; Xie, J.; Hu, X.; Peng, B.; Leng, J.; Liu, X.; Zhao, Y.; Zhang, Y.; Zhang, Q., High-Temperature Continuous-Wave Pumped Lasing from Large-Area Monolayer Semiconductors Grown by Chemical Vapor Deposition. *ACS Nano* **2018**, 12 (9), 9390-9396.
10. Schmitt-Rink, S.; Ell, C.; Haug, H., Many-body effects in the absorption, gain, and luminescence spectra of semiconductor quantum-well structures. *Physical Review B* **1986**, 33 (2), 1183-1189.
11. Rustagi, A.; Kemper, A. F., Theoretical Phase Diagram for the Room-Temperature Electron-Hole Liquid in Photoexcited Quasi-Two-Dimensional Monolayer MoS₂. *Nano Letters* **2018**, 18 (1), 455-459.

12. Schmitt-Rink, S.; Ell, C., Excitons and electron-hole plasma in quasi-two-dimensional systems. *Journal of Luminescence* **1985**, 30 (1), 585-596.
13. Asano, K.; Yoshioka, T., Exciton–Mott Physics in Two-Dimensional Electron–Hole Systems: Phase Diagram and Single-Particle Spectra. *Journal of the Physical Society of Japan* **2014**, 83 (8), 084702.
14. Schmitt-Rink, S.; Chemla, D. S.; Miller, D. A. B., Theory of transient excitonic optical nonlinearities in semiconductor quantum-well structures. *Physical Review B* **1985**, 32 (10), 6601-6609.
15. Kumagai, M.; Takagahara, T., Excitonic and nonlinear-optical properties of dielectric quantum-well structures. *Physical Review B* **1989**, 40 (18), 12359-12381.
16. Kozlov, V.; Kelkar, P.; Vertikov, A.; Nurmikko, A. V.; Chu, C. C.; Han, J.; G. Hua, C.; L. Gunshor, R., *Gain spectroscopy of excitonic molecules and its dynamics in a ZnSe single quantum well*. 1996; Vol. 54, p 13932-13937.
17. Ding, J.; Jeon, H.; Ishihara, T.; Hagerott, M.; Nurmikko, A. V.; Luo, H.; Samarth, N.; Furdyna, J., Excitonic gain and laser emission in ZnSe-based quantum wells. *Physical Review Letters* **1992**, 69 (11), 1707-1710.
18. Chernikov, A.; Ruppert, C.; M. Hill, H.; Rigosi, A.; Heinz, T., *Population inversion and giant bandgap renormalization in atomically thin WS₂ layers*. 2015; Vol. 9.
19. Zhu, B.; Chen, X.; Cui, X., Exciton Binding Energy of Monolayer WS₂. *Scientific Reports* **2015**, 5, 9218.
20. Singh, S.; Tomar, R.; ten Brinck, S.; De Roo, J.; Geiregat, P.; Martins, J. C.; Infante, I.; Hens, Z., Colloidal CdSe Nanoplatelets, A Model for Surface Chemistry/Optoelectronic Property Relations in Semiconductor Nanocrystals. *Journal of the American Chemical Society* **2018**, 140 (41), 13292-13300.
21. Wu, S.; Buckley, S.; Schaibley, J. R.; Feng, L.; Yan, J.; Mandrus, D. G.; Hatami, F.; Yao, W.; Vučković, J.; Majumdar, A.; Xu, X., Monolayer semiconductor nanocavity lasers with ultralow thresholds. *Nature* **2015**, 520, 69.
22. Yang, Z.; Pelton, M.; Fedin, I.; Talapin, D. V.; Waks, E., A room temperature continuous-wave nanolaser using colloidal quantum wells. *Nature Communications* **2017**, 8 (1), 143.
23. Grim, J. Q.; Christodoulou, S.; Di Stasio, F.; Krahne, R.; Cingolani, R.; Manna, L.; Moreels, I., Continuous-wave biexciton lasing at room temperature using solution-processed quantum wells. *Nature Nanotechnology* **2014**, 9, 891.
24. Pelton, M., Carrier Dynamics, Optical Gain, and Lasing with Colloidal Quantum Wells. *The Journal of Physical Chemistry C* **2018**, 122 (20), 10659-10674.
25. Guzelturk, B.; Pelton, M.; Olutas, M.; Demir, H. V., Giant Modal Gain Coefficients in Colloidal II–VI Nanoplatelets. *Nano Letters* **2019**, 19 (1), 277-282.

26. Dede, D.; Taghipour, N.; Quliyeva, U.; Sak, M.; Kelestemur, Y.; Gungor, K.; Demir, H. V., Highly Stable Multicrown Heterostructures of Type-II Nanoplatelets for Ultralow Threshold Optical Gain. *Chemistry of Materials* **2019**, *31* (5), 1818-1826.
27. She, C.; Fedin, I.; Dolzhnikov, D. S.; Demortière, A.; Schaller, R. D.; Pelton, M.; Talapin, D. V., Low-Threshold Stimulated Emission Using Colloidal Quantum Wells. *Nano Letters* **2014**, *14* (5), 2772-2777.
28. Li, Q.; Xu, Z.; McBride, J. R.; Lian, T., Low Threshold Multiexciton Optical Gain in Colloidal CdSe/CdTe Core/Crown Type-II Nanoplatelet Heterostructures. *ACS Nano* **2017**, *11* (3), 2545-2553.
29. Olutas, M.; Guzelurk, B.; Kelestemur, Y.; Yeltik, A.; Delikanli, S.; Demir, H. V., Lateral Size-Dependent Spontaneous and Stimulated Emission Properties in Colloidal CdSe Nanoplatelets. *ACS Nano* **2015**, *9* (5), 5041-5050.
30. Achtstein, A. W.; Antanovich, A.; Prudnikau, A.; Scott, R.; Woggon, U.; Artemyev, M., Linear Absorption in CdSe Nanoplates: Thickness and Lateral Size Dependency of the Intrinsic Absorption. *The Journal of Physical Chemistry C* **2015**, *119* (34), 20156-20161.
31. Li, Q.; Lian, T., A model for optical gain in colloidal nanoplatelets. *Chemical Science* **2018**, *9* (3), 728-734.
32. Xie, W.; Zhu, Y.; Bisschop, S.; Aubert, T.; Hens, Z.; Thourhout, D. v.; Geiregat, P., Colloidal Quantum Dots Enabling Coherent Light Sources for Integrated Silicon-Nitride Photonics. *IEEE Journal of Selected Topics in Quantum Electronics* **2017**, *23* (5), 1-13.
33. Bisschop, S.; Geiregat, P.; Aubert, T.; Hens, Z., The Impact of Core/Shell Sizes on the Optical Gain Characteristics of CdSe/CdS Quantum Dots. *ACS Nano* **2018**, *12* (9), 9011-9021.
34. Geiregat, P.; Maes, J.; Chen, K.; Drijvers, E.; De Roo, J.; Hodgkiss, J. M.; Hens, Z., Using Bulk-like Nanocrystals To Probe Intrinsic Optical Gain Characteristics of Inorganic Lead Halide Perovskites. *ACS Nano* **2018**, *12* (10), 10178-10188.
35. Flatten, L. C.; Christodoulou, S.; Patel, R. K.; Buccheri, A.; Coles, D. M.; Reid, B. P. L.; Taylor, R. A.; Moreels, I.; Smith, J. M., Strong Exciton–Photon Coupling with Colloidal Nanoplatelets in an Open Microcavity. *Nano Letters* **2016**, *16* (11), 7137-7141.
36. Chen, K.; Gallaher, J. K.; Barker, A. J.; Hodgkiss, J. M., Transient Grating Photoluminescence Spectroscopy: An Ultrafast Method of Gating Broadband Spectra. *The Journal of Physical Chemistry Letters* **2014**, *5* (10), 1732-1737.
37. Hangleiter, A.; Jin, Z.; Gerhard, M.; Kalincev, D.; Langer, T.; Bremers, H.; Rossow, U.; Koch, M.; Bonn, M.; Turchinovich, D., Efficient formation of excitons

in a dense electron-hole plasma at room temperature. *Physical Review B* **2015**, *92* (24), 241305.

38. Ulbricht, R.; Hendry, E.; Shan, J.; Heinz, T. F.; Bonn, M., Carrier dynamics in semiconductors studied with time-resolved terahertz spectroscopy. *Reviews of Modern Physics* **2011**, *83* (2), 543-586.

39. Lloyd-Hughes, J.; Jeon, T.-I., A Review of the Terahertz Conductivity of Bulk and Nano-Materials. *Journal of Infrared, Millimeter, and Terahertz Waves* **2012**, *33* (9), 871-925.

40. Dakovski, G. L.; Lan, S.; Xia, C.; Shan, J., Terahertz Electric Polarizability of Excitons in PbSe and CdSe Quantum Dots. *The Journal of Physical Chemistry C* **2007**, *111* (16), 5904-5908.

41. Wang, F.; Shan, J.; Islam, M. A.; Herman, I. P.; Bonn, M.; Heinz, T. F., Exciton polarizability in semiconductor nanocrystals. *Nature Materials* **2006**, *5*, 861.

42. Hendry, E.; Koeberg, M.; Schins, J. M.; Nienhuys, H. K.; Sundström, V.; Siebbeles, L. D. A.; Bonn, M., Interchain effects in the ultrafast photophysics of a semiconducting polymer: THz time-domain spectroscopy of thin films and isolated chains in solution. *Physical Review B* **2005**, *71* (12), 125201.

43. Evers, W. H.; Schins, J. M.; Aerts, M.; Kulkarni, A.; Capiod, P.; Berthe, M.; Grandidier, B.; Delerue, C.; van der Zant, H. S. J.; van Overbeek, C.; Peters, J. L.; Vanmaekelbergh, D.; Siebbeles, L. D. A., High charge mobility in two-dimensional percolative networks of PbSe quantum dots connected by atomic bonds. *Nature Communications* **2015**, *6*, 8195.

44. Cunningham, P. D., Accessing Terahertz Complex Conductivity Dynamics in the Time-Domain. *IEEE Transactions on Terahertz Science and Technology* **2013**, *3* (4), 494-498.

45. Murphy, J. E.; Beard, M. C.; Nozik, A. J., Time-Resolved Photoconductivity of PbSe Nanocrystal Arrays. *The Journal of Physical Chemistry B* **2006**, *110* (50), 25455-25461.

46. Kunneman, L. T.; Schins, J. M.; Pedetti, S.; Heuclin, H.; Grozema, F. C.; Houtepen, A. J.; Dubertret, B.; Siebbeles, L. D. A., Nature and Decay Pathways of Photoexcited States in CdSe and CdSe/CdS Nanoplatelets. *Nano Letters* **2014**, *14* (12), 7039-7045.

47. Hens, Z.; Moreels, I., Light absorption by colloidal semiconductor quantum dots. *Journal of Materials Chemistry* **2012**, *22* (21), 10406-10415.

48. Ivan, P. J., Valenta, *Luminescence Spectroscopy of Semiconductors*. Oxford University Press.

49. Achtstein, A. W.; Schliwa, A.; Prudnikau, A.; Hardzei, M.; Artemyev, M. V.; Thomsen, C.; Woggon, U., Electronic Structure and Exciton-Phonon Interaction

in Two-Dimensional Colloidal CdSe Nanosheets. *Nano Letters* **2012**, *12* (6), 3151-3157.

50. Norris, D. J.; Efros, A. L.; Rosen, M.; Bawendi, M. G., Size dependence of exciton fine structure in CdSe quantum dots. *Physical Review B* **1996**, *53* (24), 16347-16354.

51. Naeem, A.; Masia, F.; Christodoulou, S.; Moreels, I.; Borri, P.; Langbein, W., Giant exciton oscillator strength and radiatively limited dephasing in two-dimensional platelets. *Physical Review B* **2015**, *91* (12), 121302.

52. Scott, R.; Achtstein, A. W.; Prudnikau, A. V.; Antanovich, A.; Siebbeles, L. D. A.; Artemyev, M.; Woggon, U., Time-Resolved Stark Spectroscopy in CdSe Nanoplatelets: Exciton Binding Energy, Polarizability, and Field-Dependent Radiative Rates. *Nano Letters* **2016**, *16* (10), 6576-6583.

53. Sadao, A., *Properties of Group-IV, III-V and II-VI Semiconductors*. WILEY-VCH Verlag.

54. Kunneman, L. T.; Tessier, M. D.; Heuclin, H.; Dubertret, B.; Aulin, Y. V.; Grozema, F. C.; Schins, J. M.; Siebbeles, L. D. A., Bimolecular Auger Recombination of Electron-Hole Pairs in Two-Dimensional CdSe and CdSe/CdZnS Core/Shell Nanoplatelets. *The Journal of Physical Chemistry Letters* **2013**, *4* (21), 3574-3578.

55. Li, Q.; Lian, T., Area- and Thickness-Dependent Biexciton Auger Recombination in Colloidal CdSe Nanoplatelets: Breaking the “Universal Volume Scaling Law”. *Nano Letters* **2017**, *17* (5), 3152-3158.

56. Koch, S. W.; Kira, M.; Khitrova, G.; Gibbs, H. M., Semiconductor excitons in new light. *Nature Materials* **2006**, *5*, 523.

57. Lauth, J.; Kulkarni, A.; Spoor, F. C. M.; Renaud, N.; Grozema, F. C.; Houtepen, A. J.; Schins, J. M.; Kinge, S.; Siebbeles, L. D. A., Photogeneration and Mobility of Charge Carriers in Atomically Thin Colloidal InSe Nanosheets Probed by Ultrafast Terahertz Spectroscopy. *The Journal of Physical Chemistry Letters* **2016**, *7* (20), 4191-4196.

58. Das Sarma, S.; Jalabert, R.; Yang, S. R. E., Band-gap renormalization in semiconductor quantum wells. *Physical Review B* **1990**, *41* (12), 8288-8294.

59. Masumoto, Y.; Fluegel, B.; Meissner, K.; Koch, S. W.; Binder, R.; Paul, A.; Peyghambarian, N., Band-gap renormalization and optical gain formation in highly excited CdSe. *Journal of Crystal Growth* **1992**, *117* (1), 732-737.

60. Piermarocchi, C.; Tassone, F.; Savona, V.; Quattropani, A.; Schwendimann, P., Exciton formation rates in $\text{GaAs}/\text{Al}_x\text{Ga}_{1-x}\text{As}$ quantum wells. *Physical Review B* **1997**, *55* (3), 1333-1336.

61. Sie, E. J.; Steinhoff, A.; Gies, C.; Lui, C. H.; Ma, Q.; Rösner, M.; Schönhoff, G.; Jahnke, F.; Wehling, T. O.; Lee, Y. H.; Kong, J.; Jarillo-Herrero, P.; Gedik, N., Observation of Exciton Redshift–Blueshift Crossover in Monolayer WS₂. *Nano Letters* **2017**, *17* (7), 4210-4216.
62. Yoffa, E. J., Screening of hot-carrier relaxation in highly photoexcited semiconductors. *Physical Review B* **1981**, *23* (4), 1909-1919.
63. Semkat, D.; Richter, F.; Kremp, D.; Manzke, G.; Kraeft, W. D.; Henneberger, K., Ionization equilibrium in an excited semiconductor: Mott transition versus Bose-Einstein condensation. *Physical Review B* **2009**, *80* (15), 155201.
64. Sippel, P.; Albrecht, W.; van der Bok, J. C.; Van Dijk-Moes, R. J. A.; Hannappel, T.; Eichberger, R.; Vanmaekelbergh, D., Femtosecond Cooling of Hot Electrons in CdSe Quantum-Well Platelets. *Nano Letters* **2015**, *15* (4), 2409-2416.
65. Deng, H.; Weihs, G.; Santori, C.; Bloch, J.; Yamamoto, Y., Condensation of Semiconductor Microcavity Exciton Polaritons. *Science* **2002**, *298* (5591), 199.
66. Fraser, M. D.; Höfling, S.; Yamamoto, Y., Physics and applications of exciton–polariton lasers. *Nature Materials* **2016**, *15*, 1049.

Appendix D

1. TEM analysis. As is shown in Figure D1, brightfield transmission electron microscopy (TEM) was used to determine the lateral area of the platelets (see Figure D1). No signs of stacking were observed as is clear from the TEM image in Figure 5.1A of the main paper.¹ An average length of 34 ± 1.2 nm and width of 9.6 ± 0.6 nm is obtained, resulting in an average area of 326.4 nm². The thickness is fixed at 4.5 monolayers or 1.37 nm since the platelets are Cd-terminated.²

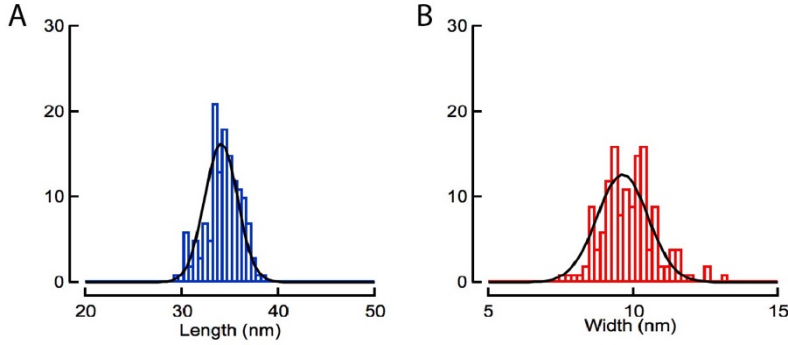


Figure D1. Analysis of brightfield transmission electron microscopy images of the platelets used in this work.

2. Linear optical properties of platelets

Absorption cross section. The intrinsic absorption coefficient $\mu_{i,0}$ can be calculated theoretically using Lorentz local field theory in connection with an effective medium Maxwell-Garnett approach. We follow the approach as laid out by Achtstein et al. who also verified this model using elemental analysis.³ Platelets are assumed to be oblate ellipsoids to calculate the linear absorption cross-section $\sigma(\lambda)$ having random orientations in the solvent medium with refractive index $n_m^2 = \epsilon_m$. As such, we obtain:

$$\mu_{i,0} = \frac{2\pi}{3n_m(\lambda)\lambda} \times (|F_x(\lambda)|^2 + |F_y(\lambda)|^2 + |F_z(\lambda)|^2) \times \epsilon_{s,I}(\lambda), \quad (\text{D.1})$$

where $\epsilon_{s,I}$ is the imaginary part of the permittivity $\epsilon_{s,I}$ is the imaginary part of the permittivity ϵ_s of bulk CdSe at λ and local field factors are given by:

$$F_i(\lambda) = \frac{1}{1 + L_i \left(\frac{\epsilon_s(\lambda)}{\epsilon_m(\lambda)} - 1 \right)}. \quad (\text{D.2})$$

The depolarization factors L_i can be written as:

$$L_i = \int_0^\infty \frac{abc}{2(s+c^2)^{3/2}(s+a^2)^{1/2}(s+b^2)^{1/2}} ds \quad (\text{D.3})$$

The numbers (a, b, c) are the half lengths in 3 dimensions. Initially, the absorption cross-section is calculated at 4.1eV (300 nm) as we can use bulk dielectric constants and we can cross-check our results with the experimental data in literature.³ Using tabulated values⁴ for the dielectric function of CdSe ($\epsilon_s = 7.4 + 8.2i$) and the refractive index of hexane, $n_s=1.405$, and taking the dimensions of the platelets into account (a=17 nm, b = 4.8 nm, c= 0.68 nm), we can calculate the different factors.

The depolarization factors are calculated as:

$$L_z = \int_0^\infty \frac{a^3 r R}{2(s+r^2 a^2)^{3/2}(s+a^2)^{1/2}(s+R^2 a^2)^{1/2}} ds = 0.8648, \quad (\text{D.4})$$

$$L_y = \int_0^\infty \frac{a^3 r R}{2(s+a^2)^{3/2}(s+R^2 a^2)^{1/2}(s+r^2 a^2)^{1/2}} ds = 0.0181, \quad (\text{D.5})$$

$$L_x = \int_0^\infty \frac{a^3 r R}{2(s+R^2 a^2)^{3/2}(s+r^2 a^2)^{1/2}(s+a^2)^{1/2}} ds = 0.1171, \quad (\text{D.6})$$

where $r = c/a$, and $R = b/a$. The local field factors are obtained as: (F_x : F_y : F_z) = (0.71: 0.95: 0.20). This leads to an average local field factor $F = \frac{1}{3} \times (F_x^2 + F_y^2 + F_z^2)$ of 0.69. This lines up with the local field factor of a cubic CdSe 0D quantum dot at 510 nm (2.4 eV), $F = 0.7$. Combining the above, we find:

$$\mu_{i,0} = 5.9 \times 10^5 \text{ cm}^{-1}. \quad (\text{D.7})$$

One can translate this μ_i to different wavelengths by means of the linear absorption spectrum A_o : $\mu_{i,0}(\lambda) = \mu_{i,0}(300) \times \frac{A_o(\lambda)}{A_o(300)}$. Now we can also translate this into an absorption cross section using the previously mentioned relation $\sigma(\lambda) = \mu_i(\lambda) \times V$:

$$\begin{aligned}\sigma_{300} &= 2.7 \times 10^{-13} \text{ cm}^2. \\ \sigma_{400} &= 7.9 \times 10^{-14} \text{ cm}^2.\end{aligned}\tag{D.8}$$

Quantum well absorption spectrum. The absorption spectrum of a quantum-well can be decomposed in excitonic (p) and free carrier transitions (C). In particular considering weak exciton localization, we can write for a given photon energy E :^{5, 6}

$$A(E) = p_x(E) + C(E), \tag{D.9}$$

with p_x the absorption line shape of a quantum well exciton with asymmetric broadening η due to localization:

$$p_x = \frac{1}{2\eta} \left(\text{erf} \left(\frac{E - E_0}{\gamma} - \frac{\gamma}{2\eta} \right) + 1 \right) \exp \left(\frac{\gamma^2}{4\eta^2} - \frac{E - E_0}{\eta} \right). \tag{D.10}$$

$C(E)$ the absorption profile associated with single-particle transitions:

$$C(E) = \frac{A_c}{2} \left[\text{erf} \left(\frac{(E - E_0) - E_{b,x}}{\gamma c} \right) \right]. \tag{D.11}$$

Here, E_0 and $E_{b,x}$ are the absolute exciton energy and exciton binding energy, respectively, and ‘erf’ is the error function. The total absorption α therefore becomes, including both light (LH) and heavy-hole (HH) contributions:

$$\alpha(E) = A_{HH} p_{HH}(E) + A_{LH} p_{LH}(E), \tag{D.12}$$

with A_{HH} and A_{LH} weight of the heavy and light bands, respectively. Table D1 summarizes the fit parameters and Figure D2 shows the relevant parameters of

the heavy-hole contribution, in particular the exciton binding energy of 193 meV and the exciton lineshape.

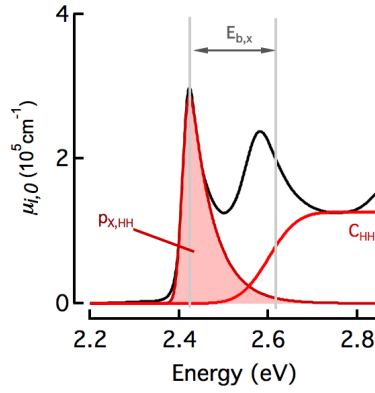


Figure D2: Decomposition of the linear absorption spectrum of our quantum wells using single-particle transitions (C) and exciton contributions (p), here shown only for the heavy-hole contribution. See main text, Figure 5.1A for the full decomposition.

	HH	LH
$E_{b,x}$ (meV)	193 ± 5	277 ± 0.65
E_0 (meV)	2408 ± 0.05	2568 ± 0.018
γ (meV)	15.94 ± 0.117	65.5 ± 0.001
A_C (meV)	5722 ± 24	2598 ± 40
γ_C (meV)	66.6 ± 2	43.0 ± 1.2
η (meV)	51.3 ± 0.4	9.1 ± 0.001
A	21394 ± 77.3	20976 ± 336

Table D1. Fit parameters

Oscillator strength. Knowing the intrinsic absorption spectrum of the heavy-hole exciton transition, the oscillator strength of the band gap can be calculated by integrating $p_{x,HH}$ as is shown in Figure D2. Indeed, this integral is directly connected to the oscillator strength via:⁷

$$f_{abs} = \frac{2\epsilon_0 n_s c m_e}{e\pi\hbar} \frac{V_{pl}}{|f_{LH}|^2} \mu_{i,gap} . \quad (D.13)$$

Table D2. Effective mass parameters, in units of m_0 , taken from Adachi:⁸

m_e	0.12
m_{HH}	0.3

where

$$\mu_{i,gap} = \int_0^{+\infty} p_{x,HH}(E) dE . \quad (D.14)$$

As such, we can use the area under the HH-absorption peak as a metric for the oscillator strength scaling, a feat which is used in Figure 5.3C of the main paper to estimate the reduction of the exciton oscillator strength.

Reduced exciton mass. The reduced mass is calculated from the isotropic electron mass and the in-plane [001] heavy-hole mass, see table D2. It is calculated, in units of m_0 , as:⁸

$$\frac{1}{m_r} = \frac{1}{m_e} + \frac{1}{m_{HH}} = 0.085 . \quad (D.15)$$

3. Amplified spontaneous emission. To cross-check the low energy optical gain window and whether the large values for the intrinsic gain coefficient are feasible, we analyzed the development of optical gain in close-packed thin films using a variation on the variable stripe length (VSL) method.⁹ Here, we use single mode silicon-nitride (SiNx) waveguides (on silica) with variable lengths to avoid in-plane diffraction, which often complicates the analysis of VSL results.⁹ A stack of 100 nm SiNx/106 nm platelets/100 nm SiNx is used and illuminated using a cylindrical lens

from the top. The spontaneous emission gets amplified along the waveguide and is collected via butt-coupling using a lensed fiber and sent to a spectrometer for analysis. A clear advantage of this approach is the well-defined amplifier length and the use of well-defined optical modes propagating along the amplifier axis. Using excitation at 480 nm, a clear ASE peak is observed at 532 nm, as is shown in Figure D3. Unfortunately, excitation at 400 nm lead to sample degradation in thin films. At an energy density of $150 \mu\text{ J/cm}^2$, a modal gain of $585 \pm 5 \text{ cm}^{-1}$ is extracted as is shown in Figure D3 (bottom right). We used a fit to a 1D amplifier model including an end facet reflection R of 5 percent:¹⁰

$$I = I_0 \left(\frac{e^{gL} - 1}{g} + \frac{R}{g} e^{2gL} (1 - e^{-gL}) \right). \quad (\text{D.16})$$

Based on a refractive index of 1.7 for the nanoplatelet layer and known parameters for the nitride waveguide, we can calculate the mode confinement¹¹ as $\Gamma = 24\%$ which, combined with a volume fraction f in thin film of 42%, leads to an estimated intrinsic gain of $g_i = \frac{585}{0.24 \times 0.42} = 5500 \text{ cm}^{-1}$. The latter value matches very well with the measured material gain under similar fluence. Indeed, a fluence of $150 \mu\text{J/cm}^2$ corresponds to $\langle N \rangle \approx 33$ for which the peak material gain would amount to 7150 cm^{-1} at 532 nm as is shown in Figure D3. Note that the modal gain measured here is already twice as large as the maximum values reported for CdSe-based QDs¹², and in line with recent reports.¹³

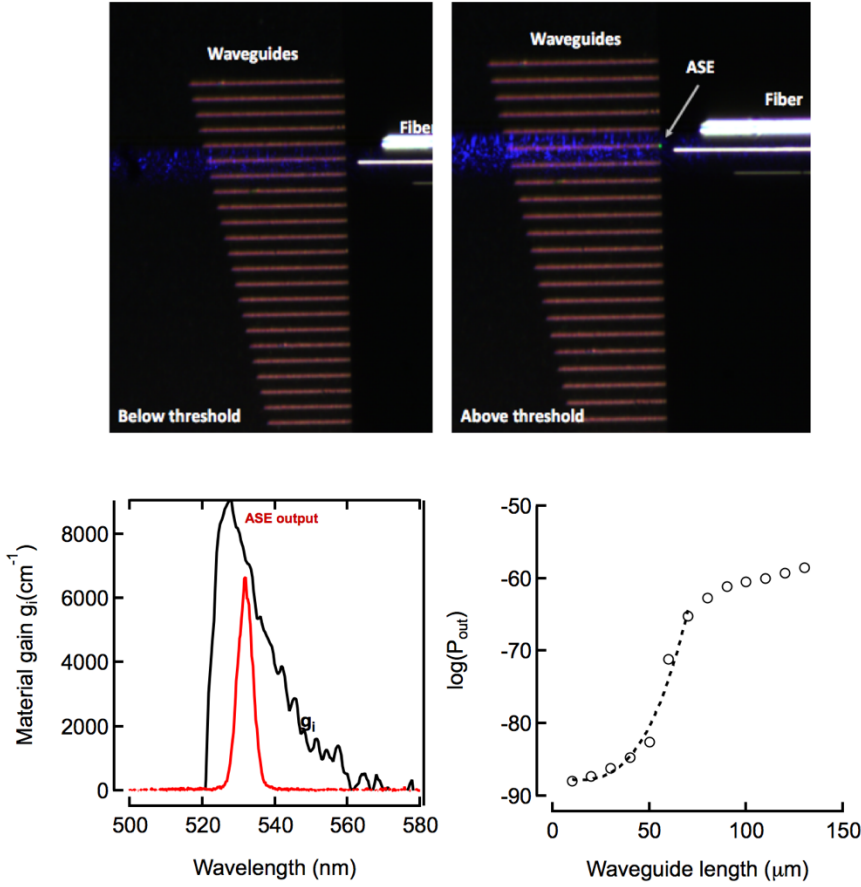


Figure D3. Variable stripe length experiment (VSL) (top) Picture of the VSL setup showing single mode silicon nitride waveguides with varying length being illuminated from the top. The amplified spontaneous emission (ASE) shows up as a bright green spot at the output facet. (bottom, left) ASE spectrum plotted together with the material gain spectrum under similar pump fluence. (bottom, right) VSL data where the output intensity of the waveguide with length L is plotted for varying L under constant flux of $150 \mu\text{J}/\text{cm}^2$. The dashed line indicates the fit according to the text.

4. Gain Threshold Determination. To accurately determine the gain threshold, we first define it properly as the required average number of absorbed photons $\langle N \rangle$ to reach $A(\lambda, t) = \Delta A(\lambda, t) + A_0(\lambda) = 0$ (transparency) at a given wavelength at a given time delay t . In practice, this only works when samples are scatter-free resulting in a proper A_0 . This is the case for our CdSe nanoplatelets as is evidenced by a zero extinction below the HH resonance, i.e. beyond 520 nm.¹ The gain threshold is then extracted by plotting the value of A at a given wavelength for increasing fluence. The

results are shown in Figure D4 leading to a gain threshold of 4.1 for the red- shifted gain band and 35 for the blue-shifted gain.

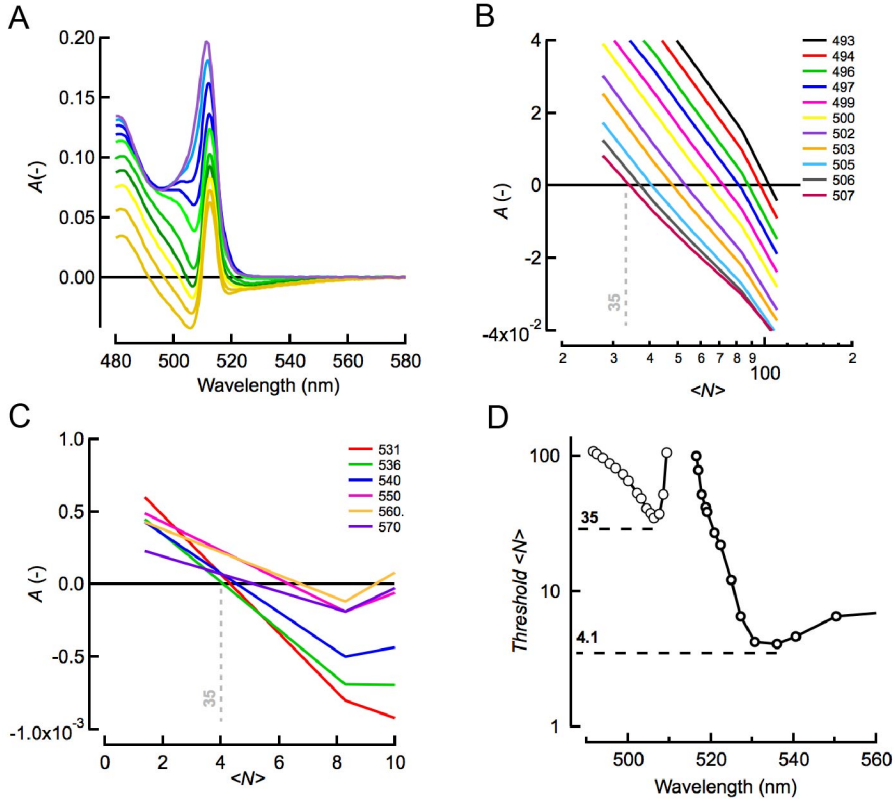


Figure D4. Determination of the gain threshold (A) Non-linear absorption spectra $A = \Delta A + A_0$ for increasing $\langle N \rangle$, (B, C) A at different wavelengths versus N . The zero-crossing is identified as the point of transparency, *i.e.* the gain threshold, which is then plotted in (D) for the different wavelengths.

5. Recombination Kinetics. From the THz and PL analysis, see further, we know that the dominant species in our platelets are excitons, in particular those contributing to luminescence at the PL peak and lower energy side of the PL peak. As such, we propose a model involving first and second order decay of excitons using their density $n = \langle N \rangle / S$ with S the surface area:

$$\frac{dn}{dt} = -k_2 n^2 - k_1 n, \quad (\text{D.17})$$

which has the following analytical solution:

$$n(t) = \frac{n_0 e^{-k_1 t}}{1 + \frac{k_2 n_0}{k_1} \times (1 - e^{-k_1 t})} . \quad (\text{D.18})$$

Several reports indicated that this description is valid, yet reported different values for the bimolecular recombination rate.¹⁴⁻¹⁶ We should note that the linear term with rate k_1 combines both exciton radiative recombination as well as linear trapping. Figure D5C shows the PL decay analysis based on equation D18. A global fit to traces at several pump fluences reveals $k_1 = 4.5 \text{ ns}^{-1}$ and $k_2 = 0.001 \text{ cm}^2 \text{ ns}^{-1}$. Rescaling the bimolecular decay to the area of the platelet, we can compare the rate of 0.3 ns^{-1} with the report of Kunneman et al. who reported 0.1 ns^{-1} .¹⁶ The single exciton decay rate is in between those found at room temperature by Kunneman¹⁶ and on single nanoplatelets at cryogenic temperatures by Tessier et al.¹⁴ who reported $5\text{--}6 \text{ ns}^{-1}$ for similarly sized platelets. Given the temperature independence of this lifetime and the quantum yield of ca. 50 %, we assign this lifetime to non-radiative processes in a sub-set of nanoplatelets.

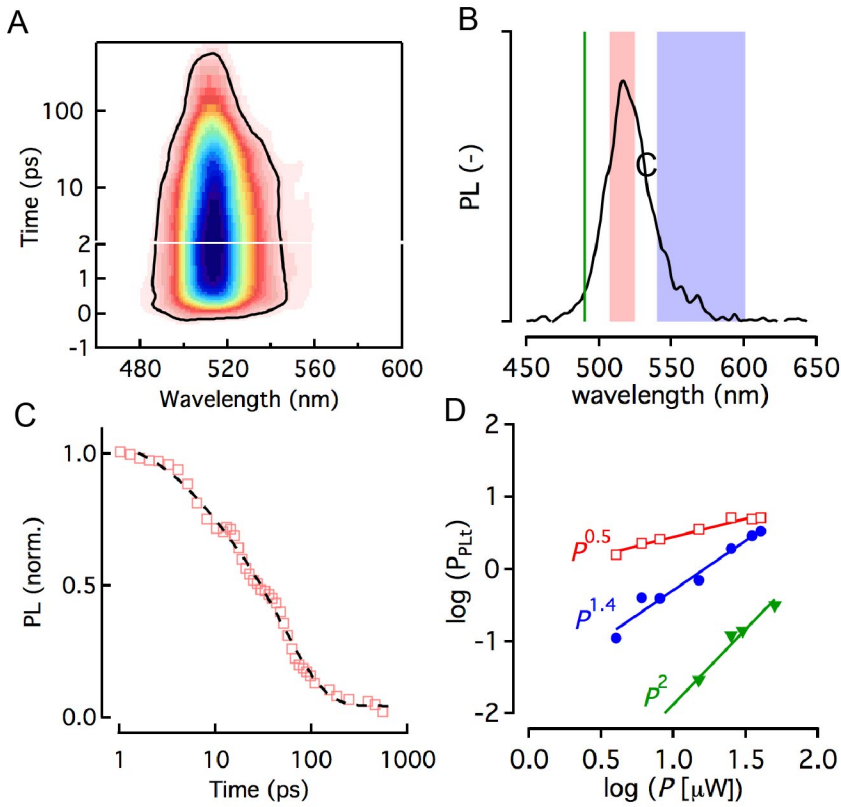


Figure D5. (A) 2D false colour map of the PL intensity after photo-excitation creating $\langle N \rangle = 12$ (B) PL spectrum at 3 ps with various regions indicated: (green) high energy free carrier PL (red) exciton emission and (blue) molecule-exciton transitions. (C) Mono- and bimolecular fit example to decay of PL. (D) Scaling of PL integrated in the green, red and blue bands of (B).

6. Saha modeling of the THz Data. We can relate the surface density of charges and excitons in a platelet by the two-dimensional Saha equilibrium constant K :¹⁸⁻²⁰

$$K = \frac{n_q^2}{n_x} = \frac{m_r k_B T}{2\pi\hbar^2} e^{-\frac{E_{b,x}}{K_B T}}, \quad (\text{D.19})$$

with n_q and n_x the free charge carrier and exciton areal density and $n = \frac{\langle N \rangle}{S} = n_q + n_x$, respectively, k_B the Boltzmann constant, $T = 294$ K the temperature, \hbar the reduced Planck constant, $E_{b,x} = 193$ meV the estimated

exciton binding energy and $m_r = 0.086 m_0$ the in-plane reduced effective mass of electrons and holes for bulk CdSe, see table D2 and D3.²¹ Using $n_q = \phi(n)n$ and $n_x = (1 - \phi(n))n$ yields:

$$\phi(n) = \frac{-K}{2n} \times \left(1 - \sqrt{1 + \frac{4n}{K}} \right). \quad (\text{D.20})$$

parameter	value
m_e	0.12
m_h	0.3
m_r	0.086
$E_{b,x}$	193 meV
T	294 K
L_z	1.37 nm
S	340 nm ²

7. Quantum Well Gain.

Optical gain in quantum wells is well described in literature.¹¹ In short, if we consider only one set of quantized levels (HH1 to CB1), see Figure 5.1A, we can calculate the absorption spectrum of a quantum well as:

$$\alpha(\omega) = \alpha_0(\hbar\omega) \times \left[f_H \left(-E_{v1} - \left(\hbar\omega - E_{c1}^{h1} \right) \frac{m_r}{m_h} \right) - f_c \left(-E_{c1} - \left(\hbar\omega - E_{c1}^{e1} \right) \frac{m_r}{m_h} \right) \right], \quad (\text{D.21})$$

with $m_e = 0.12$, $m_h = 0.3$ and $m_r = 0.086$. and $E_{e/h,1}$ is the energy of the first quantized level of the hole (h) and electron (e) relative to the valence band edge and E_{h1}^{e1} is the transition energy between both, i.e. the 2D band gap without excitonic effects. The functions f_{CH} are the Fermi-Dirac occupation factors for the conduction (C) and valence band (H) levels and depend on the quasi-Fermi level positions. We note that α_0 is the C_{HH} form defined from the fit to the linear absorption spectrum in Figure 5.1C of the main text, see also section D1.

The quasi-Fermi levels are dictated by the photo-generated carrier density, where for an undoped system under optical excitation $n = p$.

$$n = \int dE \rho_e^{2D}(E) f_c(E) , \quad (\text{D.22})$$

where ρ_e^{2D} is the density of states and $f_c(E) = \frac{1}{1 + e^{\frac{E_{c1} + E_t - F_c}{kT}}}$. This leads to the form:

$$n = \frac{m_e k_B T}{\pi \hbar^2} \ln \left(1 + e^{\frac{F_c - E_{c1}}{k_B T}} \right) = n_0 \ln \left(1 + e^{\frac{F_c - E_{c1}}{k_B T}} \right) \quad (\text{D.23})$$

And similarly for the holes. The prefactor n_0 is often denoted as the band edge intrinsic density and amounts to:

$$\begin{aligned} n_0 &= \frac{m_e k_B T}{\pi \hbar^2} = 1.4 \times 10^{12} \text{ cm}^{-2}, \\ p_0 &= \frac{m_h k_B T}{\pi \hbar^2} = 3.6 \times 10^{12} \text{ cm}^{-2} \end{aligned} \quad (\text{D.24})$$

at $T = 300$ K. Using these expressions, we can calculate the shift in quasi-Fermi level of both electrons and holes and hence the gain/absorption spectrum. Figure D6C shows the values for the quasi-Fermi level differences ΔE_{fi} for both electrons ($i=e$) and holes ($i=h$). Figure D6A shows the result of these calculations at 300 K for increasing carrier densities comparable to the experimental values, see also Figure 5.2C of the main text. We observe optical gain for densities exceeding ca. 20 electron-hole pairs per platelet. Figure D6D shows the same calculation yet using the correct carrier temperatures extracted from PL analysis and zoomed in on the region of the gain threshold (density). Optical gain can be observed at densities close to $\langle N \rangle = 20$ though would only be resolvable experimentally from 26 onwards given the experimental noise for of ca. 50 cm^{-1} and competition with the lingering HH and LH absorption at 2.42 and 2.56 eV, respectively.

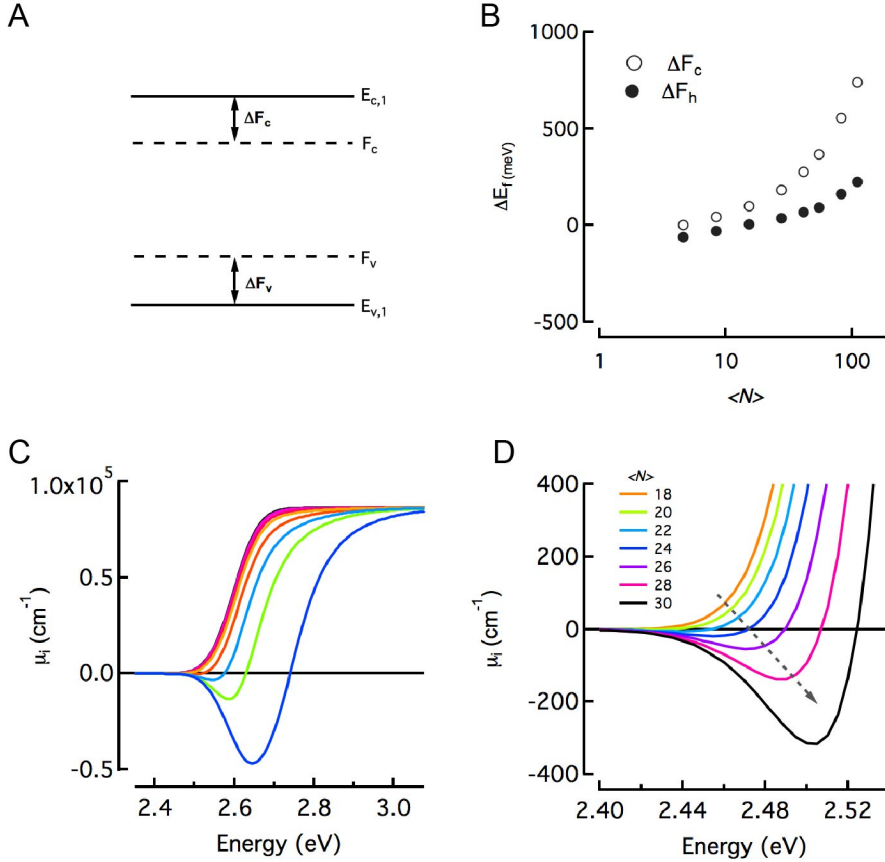


Figure D6. Free carrier mediated optical gain (A) Energy levels of free carrier transitions in a QW with quasi-Fermi levels $F_{c,v}$. (B) Calculated shifts of the quasi-Fermi levels for electrons and holes. (C) Free carrier gain from the HH-CB1 transition for increasing carrier density at 300 K. (D) Similar to (C), but zoomed in on the gain threshold density and using the correct carrier temperatures extracted from PL.

8. Support for the discussion section.

Density of states. The number of available states in a 2D semiconductor can be based

on the density of states: $g_{X,2D,eV} = \frac{m_x}{\pi \hbar^2}$, which using $m_{x,HH} = 0.42m_0$, amounts to

4569 eV^{-1} . In a 50 meV window, the exciton linewidth, already up to 228 states available for the excitons to occupy.

2. Pump wavelength variation. If we change the excess energy of the electron-hole pairs generated by the pump, we can affect the hot carrier thermalization. Figure D7 shows that when switching from 400 nm to 480 nm under the same excitation density $\langle N \rangle = 112$, hence lowering the excess energy by 500 meV, we observe a lower magnitude in the blue-shifted gain window and a substantially narrower gain window. This does not match the notion of state filling since at the same exciton density, state-filling should be independent on the carrier temperature.

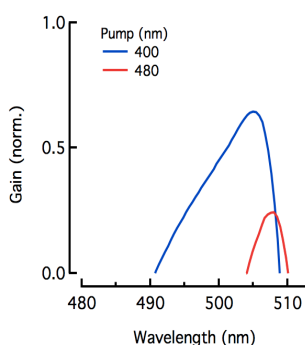


Figure D7. Normalized (at HH bleach) gain spectrum for pumping at 400 nm (blue) and 480 nm (red) creating the same exciton number $\langle N \rangle = 45$, showing a smaller blue-shifted gain spectrum with a narrower width.

References

1. Singh, S.; Tomar, R.; ten Brinck, S.; De Roo, J.; Geiregat, P.; Martins, J. C.; Infante, I.; Hens, Z., Colloidal CdSe Nanoplatelets, A Model for Surface Chemistry/Optoelectronic Property Relations in Semiconductor Nanocrystals. *Journal of the American Chemical Society* **2018**, *140* (41), 13292-13300.
2. Ithurria, S.; Tessier, M. D.; Mahler, B.; Lobo, R. P. S. M.; Dubertret, B.; Efros, A. L., Colloidal nanoplatelets with two-dimensional electronic structure. *Nature Materials* **2011**, *10*, 936.
3. Achtstein, A. W.; Antanovich, A.; Prudnikau, A.; Scott, R.; Woggon, U.; Artemyev, M., Linear Absorption in CdSe Nanoplates: Thickness and Lateral Size Dependency of the Intrinsic Absorption. *The Journal of Physical Chemistry C* **2015**, *119* (34), 20156-20161.
4. Adachi, S., *Optical constants of crystalline and amorphous semiconductors : numerical data and graphical information*. Kluwer Academic Publishers: Boston ;, 1999.
5. Grim, J. Q.; Christodoulou, S.; Di Stasio, F.; Krahne, R.; Cingolani, R.; Manna, L.; Moreels, I., Continuous-wave biexciton lasing at room temperature using solution-processed quantum wells. *Nature Nanotechnology* **2014**, *9*, 891.
6. F. Schnabel, R.; Zimmermann, R.; Bimberg, D.; Nickel, H.; Lösch, R.; Schlapp, W., *Influence of exciton localization on recombination line shapes: In_{x}Ga_{1-x}As/GaAs quantum wells as a model*. 1992; Vol. 46.
7. Hens, Z.; Moreels, I., Light absorption by colloidal semiconductor quantum dots. *Journal of Materials Chemistry* **2012**, *22* (21), 10406-10415.
8. Sadao, A., *Properties of Group-IV, III-V and II-VI Semiconductors*. WILEY-VCH Verlag.
9. Xie, W.; Zhu, Y.; Bisschop, S.; Aubert, T.; Hens, Z.; Thourhout, D. v.; Geiregat, P., Colloidal Quantum Dots Enabling Coherent Light Sources for Integrated Silicon-Nitride Photonics. *IEEE Journal of Selected Topics in Quantum Electronics* **2017**, *23* (5), 1-13.
10. Zhu, Y.; Xie, W.; Bisschop, S.; Aubert, T.; Brainis, E.; Geiregat, P.; Hens, Z.; Van Thourhout, D., On-Chip Single-Mode Distributed Feedback Colloidal Quantum Dot Laser under Nanosecond Pumping. *ACS Photonics* **2017**, *4* (10), 2446-2452.
11. S, C., *Physics of Photonics Devices*. 2 ed.; John Wiley & Sons Ltd.
12. Bisschop, S.; Geiregat, P.; Aubert, T.; Hens, Z., The Impact of Core/Shell Sizes on the Optical Gain Characteristics of CdSe/CdS Quantum Dots. *ACS Nano* **2018**, *12* (9), 9011-9021.

13. Guzelturk, B.; Pelton, M.; Olutas, M.; Demir, H. V., Giant Modal Gain Coefficients in Colloidal II–VI Nanoplatelets. *Nano Letters* **2019**, *19* (1), 277-282.
14. Tessier, M. D.; Javaux, C.; Maksimovic, I.; Lorient, V.; Dubertret, B., Spectroscopy of Single CdSe Nanoplatelets. *ACS Nano* **2012**, *6* (8), 6751-6758.
15. Pelton, M., Carrier Dynamics, Optical Gain, and Lasing with Colloidal Quantum Wells. *The Journal of Physical Chemistry C* **2018**, *122* (20), 10659-10674.
16. Kunneman, L. T.; Tessier, M. D.; Heuclin, H.; Dubertret, B.; Aulin, Y. V.; Grozema, F. C.; Schins, J. M.; Siebbeles, L. D. A., Bimolecular Auger Recombination of Electron–Hole Pairs in Two-Dimensional CdSe and CdSe/CdZnS Core/Shell Nanoplatelets. *The Journal of Physical Chemistry Letters* **2013**, *4* (21), 3574-3578.
17. Ivan, P. J., Valenta, *Luminescence Spectroscopy of Semiconductors*. Oxford University Press.
18. Kaindl, R. A.; Hägele, D.; Carnahan, M. A.; Chemla, D. S., Transient terahertz spectroscopy of excitons and unbound carriers in quasi-two-dimensional electron-hole gases. *Physical Review B* **2009**, *79* (4), 045320.
19. Hangleiter, A.; Jin, Z.; Gerhard, M.; Kalincev, D.; Langer, T.; Bremers, H.; Rossow, U.; Koch, M.; Bonn, M.; Turchinovich, D., Efficient formation of excitons in a dense electron-hole plasma at room temperature. *Physical Review B* **2015**, *92* (24), 241305.
20. Noriyasu, M.; Fujiwara, K., *Excitonic electroluminescence at room temperature in an (In,Ga)As multiple-quantum-well diode*. 2010; Vol. 97, p 031103-031103.
21. Naeem, A.; Masia, F.; Christodoulou, S.; Moreels, I.; Borri, P.; Langbein, W., Giant exciton oscillator strength and radiatively limited dephasing in two-dimensional platelets. *Physical Review B* **2015**, *91* (12), 121302.

Summary

The aim of this thesis is to study the nature of photoexcitations and carrier multiplication in low-dimensional semiconductors using ultrafast spectroscopy techniques. Ongoing from a macroscopic scale to a nanoscale, the electronic and optical properties of a material become size dependent, and differ significantly from their bulk counterpart due to quantum confinement, and the surrounding dielectric environment. Electrons and holes in nano-semiconductors can attract each other to form neutral bound electron-hole pairs known as excitons. Stable robust excitons are useful to achieve optical gain and lasing. The Coulomb interaction between electrons and holes in nano-semiconductors is enhanced due to quantum confinement, which can lead to the creation of multiple electron-hole pairs per single absorbed photon *via* a process called carrier multiplication (CM). CM is beneficial to achieve a power conversion efficiency in a solar cell beyond the Shockley-Queisser limit.

Until now, CM in thin films and solar cells of semiconductor nanocrystals (NCs) has been found at photon energies well above the minimum required energy of twice the band gap. The high threshold of CM strongly limits the benefits for solar cell applications. In chapter 2, we show that CM is more efficient in a percolative network of directly connected PbSe NCs. The CM threshold is at twice the band gap and increases in a steplike fashion with photon energy. A lower CM efficiency is found for a solid of weaker coupled NCs. This demonstrates that the coupling between NCs strongly affects the CM efficiency. According to device simulations, the measured CM efficiency would significantly enhance the power conversion efficiency of a solar cell.

In chapter 3, we determine to what extent photoexcitation of PbSe nanorods leads to free charges or excitons, and we determine the charge carrier mobility and the exciton polarizability. We combine transient optical absorption (TA) spectroscopy with terahertz (THz) photoconductivity measurements for different photoexcitation densities to distinguish free charges from excitons. From analysis of the TA and THz photoconductivity data it is inferred that photoexcitation leads predominantly to formation of excitons. For higher photoexcitation density the photoconductivity is strongly affected by mutual interactions between charges leading to a lower charge mobility. The high quantum yield of excitons makes PbSe nanorods of interest for applications in near infra-red LEDs or lasers. For use in solar cells, hetero-junctions must be realized, so that excitons can dissociate into free charges.

PbSe honeycomb superlattices have been prepared by facet-specific oriented attachment to combine the electronic properties of graphene with semiconducting properties. Theoretical calculations on PbSe honeycomb structures have shown the presence of Dirac cones at the K point of the Brillouin Zone and hence massless Dirac carriers are expected near the K point. In chapter 4, we report the band occupation and electron transport in PbSe honeycomb superstructures at room temperature studied by two different methods. First, we incorporated single-layers of PbSe honeycomb structures into transistor-type devices. With electrochemical gating we could populate the lowest conduction band with electrons in a controlled way. Second, electrons and holes were generated by optical pumping, and the resulted charge carriers were probed by THz spectroscopy. The experimental data show a similar mobility in both the transistor type measurement and THz photoconductivity measurement. The fits to the complex THz photoconductivity data revealed pronounced charge backscattering by imperfections in the superstructure. The study of Dirac physics in honeycomb semiconductors will require improved superlattices.

In chapter 5, we focus on light amplification and the complex photo-physics at high excitation density in CdSe nanoplatelets by using transient optical absorption spectroscopy, time-resolved photoluminescence measurement, and THz photoconductivity experiments. At low density, optical gain originates from excitonic molecules. At increasing pair density, we observe a persistence of this excitonic gain regime and the unexpected co-existence of blue-shifted and significantly enhanced optical gain. Terahertz photoconductivity measurements show the coexistence of excitons with free charges indicating the absence of a full Mott transition.

Samenvatting

Het doel van deze dissertatie is om met gebruik van ultrasnelle spectroscopietechnieken de aard van foto-excitaties en dragermultiplicatie in laag-dimensionale halfgeleiders te bestuderen. Wanneer de macroscopische afmetingen van deze halfgeleiders worden verkleind naar de nanoschaal, worden de elektronische en optische eigenschappen van het materiaal afhankelijk van grootte en verschillen zij aanmerkelijk van hun bulkequivalent als gevolg van quantum confinement en de diëlektrische omgeving waarin zij zich bevinden. Elektronen en gaten in nano-halfgeleiders kunnen elkaar aantrekken om een neutraal geladen elektron-gatpaar te vormen, hetgeen een exciton wordt genoemd. Stabiele, robuuste excitonen zijn nuttig voor het behalen van optical gain en lasing. De Coulomb-interactie tussen elektronen en gaten in nano-halfgeleiders wordt verbeterd door middel van quantum confinement. Dit kan leiden tot carrier multiplication (CM), waarbij een enkel geabsorbeerd foton kan leiden tot de vorming van meerdere elektron-gatparen. CM is bevorderlijk voor het behalen van efficiënte energieconversie in een zonnecel boven de Shockley-Queisser-limiet.

Tot op heden is CM geobserveerd in dunne lagen en zonnecellen van halfgeleider-nanokristallen (NC's) bij fotonenergieën van ruim boven de minimumvereiste energie van tweemaal de bandkloof. De hoge drempel van CM beperkt de voordelen van de toepassing in zonnecellen aanzienlijk. In hoofdstuk 2 tonen wij aan dat CM efficiënter is in een percolatief netwerk van direct verbonden NC's van PbSe. De CM-drempel bedraagt tweemaal de bandkloof en neemt stapsgewijs toe met de fotonenergie. Wanneer de NC's minder sterk gekoppeld zijn, wordt een lagere CM-efficiëntie waargenomen. Dit toont aan dat de koppeling van NC's een aanzienlijke invloed heeft op de CM-efficiëntie. Volgens simulaties zou de gemeten CM-efficiëntie de energieopbrengst van zonnecellen aanzienlijk verhogen.

In hoofdstuk 3 bepalen wij de mate waarin foto-excitatie van PbSe nanostaafjes tot vrije ladingen óf excitonen leidt. Daarnaast meten wij de mobiliteit van de ladingsdragers en de polariseerbaarheid van excitonen. Om de vrije ladingen van excitonen te onderscheiden, combineren we optische absorptiespectroscopie in aangeslagen toestand (transient absorption, TA) met terahertz (THz) fotogeleidingsmetingen bij verschillende foto-excitatiedichtheden. Uit de analyse van deze data wordt afgeleid dat foto-excitatie overwegend leidt tot vorming van excitonen. Bij een hogere foto-excitatiedichtheid wordt de fotogeleiding sterk beïnvloed door wederzijdse interactie tussen de ladingen, wat tot een lagere ladingsmobiliteit leidt. Door de hoge kwantumopbrengst van excitonen zijn PbSe

nanostaafjes interessant voor toepassingen in nabij-infrarode LEDs of lasers. Voor gebruik in zonnecellen moeten heterojuncties gerealiseerd worden, zodat excitons tot vrije ladingen kunnen dissociëren.

Om de elektronische en halfgeleidende eigenschappen van grafeen te combineren, zijn honingraatvormige superroosters van PbSe geprepareerd door middel van facet-specifiek georiënteerde bevestiging. Theoretische berekeningen op deze structuren hebben de aanwezigheid van Dirac-kegels op het *K*-punt van de Brillouin-zone aangetoond en daarom worden nabij het *K*-punt gewichtloze Dirac-dragers verwacht. In hoofdstuk 4 doen wij verslag van de bandbezetting en het elektronentransport in honingraatvormige superstructuren van PbSe bij kamertemperatuur, zoals bestudeerd middels twee verschillende methodes. Eerst hebben wij de enkele PbSe honingraatstructuurlagen verwerkt in transistor-type cellen. Door middel van elektrochemische gating konden wij op gecontroleerde wijze de laagste geleidingsband met elektronen bevolken. Vervolgens hebben wij elektronen en gaten gegenereerd door middel van optische excitatie en de ontstane ladingen onderzocht middels THz-spectroscopie. De experimentele data vertonen een vergelijkbare mobiliteit in zowel de transistor-type als de THz-fotogeleidingsmetingen. De fits van de complexe THz-fotogeleidingsdata lieten een uitgesproken verstrooiing van lading zien door imperfecties in de superstructuur. Voor toekomstig onderzoek van Dirac-fysica in halfgeleiders met honingraatstructuren zijn betere superroosters nodig.

In hoofdstuk 5 richten wij ons op lichtversterking en complexe fotofysica bij een hoge excitatiedichtheid in CdSe nanoplaatjes door middel van absorptiespectroscopie in aangeslagen toestand, tijdsafhankelijke fotoluminescentiemetingen en THz-fotogeleidingsexperimenten. Bij lage excitatiedichtheden leiden excitonische moleculen tot optical gain. Bij het verhogen van de parendichtheid, kunnen wij zowel een voortzetting van dit excitonische gain-regime waarnemen, als de onverwachte co-existentie van een blauwvershoven en aanmerkelijk vergrote optical gain. THz-fotogeleidingsmetingen tonen de co-existentie van excitonen en vrije ladingen aan, wat duidt op de afwezigheid van een volledige Mott-transitie.

Acknowledgements

This thesis is a result of contributions from many people who collaborated and supported this work over the past five years. I would like to express my gratitude to those who made this work possible.

At first, I would like to thank prof. dr. Laurens Siebbeles for providing the opportunity to work as a Ph.D. student in your group, and supervising this work. I am thankful to you for helping in interpreting the data and for the time you spent on revising our manuscripts.

Juleon, thanks for teaching me terahertz spectroscopy and explaining the set up in detail, and encouraging me to write scripts for analyzing the data. You are innovative and you like to solve problems in a unique way. Working with you I learnt various topics.

Wiel, I would not have completed this thesis without the samples you provided. Especially chapters 2 and 3 of this thesis are based on the study on the samples that you provided. Thanks for preparing the samples. Building the terahertz set up in the new building together with you and Jos was a great learning experience.

Jos, thanks for helping me with issues related to the laser and helping me with the beam alignment in the terahertz lab. Ruben, thanks for your guidance on various topics and introducing me to the group when I arrived. Michiel Aerts, thanks for clearing my doubts during my first year of research, and Lucas for the TA code.

Maryam, Daniel, Arjan, Pieter, Renu, Stanko, and Christophe, Michele, and Eva thanks for collaborating with us, based on which chapters 4 and 5 are written.

Cecilia and Els thanks for organizing my stay and residence permit. A special thanks to the OM group for being helpful and friendly: Indy, Jence, Ferdinand, Tom, Ryan, Arjan, Silke, Michele, Sourav, Gianluca, Frank, Deepika, Jannika, Alexander, Wybe, Martien, Wil, John, Jaco, Nick, Ward, Eline, Nico, Sudeep, Valentina, Solrun, Dengyang, Maria, kevin, Magnus, Cansel, Sudeep.

I am thankful to my friends: Prashant, Swasti, Rishabh, Raviraja, Hamit, Birbal, Muzaffar, Phani, Harshita, Rajeev, Sumit, Vijay, Damla, Sushma, Vaishnavi, Himanshu, Tarun, Amol, Shammi, Madhu and Rochan for making my stay in Delft memorable, and enjoyable.

I am thankful to prof. M. Krishnamurthy, and Ram Gopal for providing me hands on experience with femtosecond lasers and optical imaging, and providing a research experience at the Tata Institute of Fundamental Research, Hyderabad.

I am grateful to my parents for encouraging me to take up research. I am thankful for your support in helping me to follow my dreams.

I would like to thank the committee members for spending their valuable time on reading and evaluating my thesis.

I am thankful to the Foundation for Fundamental Research on Matter (FOM), which is part of The Netherlands Organization for Scientific Research (NWO), for providing the funding required for this research in the programme “Designing Dirac Carriers in Semiconductor Honeycomb Superlattices”.

List of publications

Photogeneration Quantum Yield and Character of Free Charges and Excitons in PbSe Nanorods.

Aditya Kulkarni, Wiel H. Evers, Thomas P. van Waas, and Laurens D. A. Siebbeles. In preparation.

Room-Temperature Electron Transport in PbSe Honeycomb Superstructures Studied in a Transistor Configuration and by Terahertz Spectroscopy.

Maryam Alimoradi Jazi, Aditya Kulkarni, Sophia Buhbut Sinai, Joep L. Peters, Eva Geschiere, Michele Failla, Christophe Delerue, Arjan J. Houtepen, Laurens D. A. Siebbeles, and Daniel Vanmaekelbergh.

The Journal Physical Chemistry C, in press.

A Charge Carrier Cooling Bottleneck Opens up Non-Excitonic Gain Mechanisms in Colloidal CdSe Quantum Wells.

Renu Tomar, Aditya Kulkarni, Kai Chen, Shalini Singh, Dries Van Thourhout, Justin M Hodgkiss, Laurens D. A. Siebbeles, Zeger Hens, and Pieter Geiregat.

The Journal Physical Chemistry C, 2019, 123(14), 9640–9650.

Ultrafast Charge Cooling and Carrier Multiplication in Semiconductor Nanocrystals and Superlattices.

Aditya Kulkarni, and Laurens D. A. Siebbeles.

Proc. SPIE 10673, Advances in Ultrafast Condensed Phase Physics 2018, 1067306

Efficient Steplike Carrier Multiplication in Percolative Networks of Epitaxially Connected PbSe Nanocrystals.

Aditya Kulkarni, Wiel H. Evers, Stanko Tomić, Matthew C. Beard, Daniel Vanmaekelbergh and Laurens D. A. Siebbeles.

ACS Nano 2017, 12(1), 378-384.

All-Printed Thin-Film Transistors From Networks of Liquid-Exfoliated Nanosheets.

Adam G Kelly, Toby Hallam, Claudia Backes, Andrew Harvey, Amir Sajad Esmaeily, Ian Godwin, João Coelho, Valeria Nicolosi, Jannika Lauth, Aditya Kulkarni, Sachin Kinge, Laurens DA Siebbeles, Georg S Duesberg, Jonathan N Coleman.

Science 2017, 356(6333), 69-73.

A Source to Deliver Mesoscopic Particles for Laser Plasma Studies.

R. Gopal, R. Kumar, M. Anand, A. Kulkarni, D. P. Singh, S. R. Krishnan, V. Sharma, and M. Krishnamurthy.

Review of Scientific Instruments 2017, 88, 023301.

Photogeneration and Mobility of Charge Carriers in Atomically Thin Colloidal InSe Nanosheets Probed by Ultrafast Terahertz Spectroscopy.

Jannika Lauth, Aditya Kulkarni, Frank C. M. Spoor, Nicolas Renaud, Ferdinand C. Grozema, Arjan J. Houtepen, Juleon M. Schins, Sachin Kinge, and Laurens D. A. Siebbeles.

The Journal of Physical Chemistry Letters 2016, 7 (20), 4191–4196.

High Charge Mobility in Two-Dimensional Percolative Networks of PbSe Quantum Dots Connected by Atomic Bonds.

Wiel H. Evers, Juleon M. Schins, Michiel Aerts, Aditya Kulkarni, Pierre Capiod, Maxime Berthe, Bruno Grandidier, Christophe Delerue, Herre S.J. van der Zant, Carlo van Overbeek, Joep L. Peters, Daniel Vanmaekelbergh & Laurens D.A. Siebbeles.

Nature communications 2015, 6, 8195.

Curriculum Vitae

Aditya Kulkarni was born on the 6th February 1989 in Davanagere, India. He studied physics at Sri Sathya Sai Institute of Higher Learning, Bangalore, from 2008 to 2011, and completed BSc in physics in 2011. He continued his study in physics, and specialized in photonics, and obtained his MSc in physics in 2013 from Sri Sathya Sai Institute of Higher Learning, Puttaparthi, India.

In July 2013, he joined Tata Institute of Fundamental Research, Hyderabad, to work as a Junior Research Fellow, and was involved in the project to develop mesoscopic particle generator to perform laser-matter interaction experiments without using substrates.

From 2014 to 2019, he performed research at the Optoelectronic Materials section at the Delft University of Technology under supervision of prof. dr. Laurens Siebbeles. The aim of the project was to study “The nature of photoexcitations and carrier multiplication in low-dimensional semiconductors”. This project was funded by the Foundation for Fundamental Research on Matter (FOM), which is part of The Netherlands Organization for Scientific Research (NWO), in the programme “Designing Dirac Carriers in Semiconductor Honeycomb Superlattices”.

